

1 **Temperature micro-mapping in oscillatory zoned chlorite: Application to**
2 **study of a green-schist facies fault zone in the Pyrenean Axial Zone (Spain)**

3

4 Vincent Trincal^{1*}, Pierre Lanari², Martine Buatier¹, Brice Lacroix³, Delphine Charpentier¹,
5 Pierre Labaume⁴ and Manuel Muñoz⁵

6

7

8 ¹ UMR Chrono-Environnement, Université de Franche-Comté, 16 Route de Gray, Besançon,
9 France.

10 ² Institute of Geological Sciences, University of Bern, Baltzstrasse 1+3, CH-3012 Bern,
11 Switzerland.

12 ³ Department of Earth and Environmental Sciences, University of Michigan, Ann Arbor,
13 Michigan, USA.

14 ⁴ Géosciences Montpellier, UMR 5243, Université de Montpellier-CNRS, 34095 Montpellier,
15 France.

16 ⁵ Institut des Sciences de la Terre, CNRS, Université Grenoble 1, Grenoble, France.

17

18

19 * **Corresponding author:** Vincent Trincal (email address: vincenttrincal@gmail.com)

20

21

22 *Revision 1 to American Mineralogist*

23

24

25 **Keywords:**

26 Oscillatory zoning, Chlorite, XFe³⁺, Geothermometer, μ -XANES, X-ray mapping,
27 XMAPTOOLS

28

Abstract

29

30

31

32

33

34

35

36

37

38

39

40

41

42

43

44

45

46

47

48

49

50

51

52

Oscillatory compositional zoning in minerals has been observed in hydrothermal, magmatic and metamorphic environments and is commonly attributed to chemical or physical cyclical changes during crystal growth. Chemical zoning is a common feature of solid solutions, which has been rarely reported in phyllosilicates. In this study, oscillatory zoning in chlorite is described in samples from the Pic-de-Port-Vieux thrust, a minor thrust fault associated to the major Gavarnie thrust fault zone (Central Pyrenees, Spain). The Pic-de-Port-Vieux thrust sheet comprises a 1-20 meter thick layer of Triassic red pelite and sandstone thrust over mylonitized Cretaceous dolomitic limestone. The thrust fault zone deformation comprises secondary faults and cleavage affecting the Triassic pelite and sandstone. An important feature responsible to this deformation is a set of veins filled by quartz and chlorite. Chlorite is present in crack-seal extension veins and in shear veins, both structures opened under the same stress conditions. In some shear veins, chlorite occurs as pseudo-uniaxial plates arranged in rosette-shaped aggregates. These aggregates appear to have developed as a result of radial growth of the chlorite platelets. Oscillatory zoning has been imaged by backscattered scanning electron microscopy and by X-ray quantitative micro-mapping. These oscillations correspond to chemical zoning with alternating iron-rich and magnesium-rich bands. The chlorite composition ranges from a Fe-rich pole to a Mg-rich pole. $Fe^{3+}/\Sigma Fe$ values were measured in chlorite using μ -XANES spot analyses and vary from 0.23 to 0.44. The highest values are in the Fe-rich area. Temperature maps, built from standardized microprobe X-ray images and redox state using the program XMAPTOOLS, indicate oscillatory variations from about 310 to $400\pm 50^\circ C$ during chlorite crystallization. These temperature variations are correlated with a $Fe^{3+}/\Sigma Fe$ variation by $Al^{3+}Fe^{3+}_{-1}$ and di-trioctahedral substitutions highlighted by Mg and Fe_{Tot} contents (Fe-Mg zoning). Chemical variations could be then explained by alternation of cooling times and cyclical pulses of a fluid hotter

53 than the host rock. It is however not excluded that kinetic effects influence the incorporation
54 of Mg or Fe during chlorite crystallization.

55

56

Introduction

57 In sedimentary basins petrophysical characterization of a fault zone and reconstruction
58 of the pressure-temperature evolution during faulting activity are of major interest for both
59 fundamental research and oil industry. Indeed, faults can serve as drains or barriers for crustal
60 fluid flow, including hydrocarbons. They may also record fluid-rock interactions in
61 syntectonic veins (e.g., Lacroix et al. 2014). The fault cores are often mineralized with,
62 among other, clay rich zones (e.g., Buatier et al. 2012; Lacroix et al. 2012; Leclère et al. 2012;
63 Cantarero et al. 2014; Trincal et al. 2014a). The role of authigenic clay growth in clay-bearing
64 fault zones is increasingly recognized as a key to understand the mechanics of brittle faulting
65 and thrusting processes (e.g. Wintsch et al. 1995). This provides new insights into the ongoing
66 debate about the frictional strength of brittle faults (e.g., Chester et al. 1993; Bos and Spiers
67 2001; Holdsworth 2004; Haines and Van Der Pluijm 2012; Leclère et al. 2014). In rare cases,
68 oscillatory zoned minerals can be observed. These minerals witness fluid-rock interaction
69 processes such as mineralogical reactions and mass transfer assisted by fluids (e.g. Beaufort et
70 al., 2005). Their study allows a better understanding of processes such as pressure-solution,
71 fluid-rock interaction and recrystallization occurring during thrust faulting.

72 With the development of electron imaging techniques, chemical zoning patterns in
73 metamorphic, magmatic and hydrothermal minerals have been increasingly investigated (e.g.,
74 Jamtveit et al. 1993; de Andrade et al. 2006; Friel and Lyman 2006; Vidal et al. 2006; Dziggel
75 et al. 2009; Robyr et al. 2009, 2014; Pearce and Wheeler 2010; Blanco-Quintero et al. 2011;
76 Dare et al. 2011; Lanari et al. 2012, 2013, 2014b; Manzotti and Ballèvre 2013; Martin et al.
77 2013; Zhai et al. 2014). Depending on the geological environments and the minerals involved,

78 chemical zoning reflects time series of equilibrium conditions experienced by the rock.
79 Several parameters such as pressure (P), temperature (T), oxygen fugacity (f_{O_2}), water activity
80 (a_{H_2O}), redox conditions (XFe^{3+}) and bulk-rock (solid) or fluid chemical compositions can be
81 involved. For example, the study of zoned minerals is critical to reconstruct detailed P-T paths
82 of individual samples. In low-grade metamorphic rocks, the diffusion processes are slow
83 enough to preserve successive stages of growth and continuous P-T conditions may be
84 derived by analyzing preserved local equilibria (Lanari et al. 2013 and references therein).
85 According to Kohn (2003) all minerals could show zoning for a particular element or isotope
86 at a given scale, and it is simply a matter of time or analytical precision increase before that
87 zonation is described. Chemical zoning patterns such as concentric zoning may result from
88 successive stages of crystallization. From a macroscopic point of view, the variations in
89 chemical composition from core to rim of minerals result of the variations in the relative
90 proportions in a solid solution between two or more end-member minerals. The final rim may
91 show a reversal trend due to late consumption or resorption during retrograde reactions
92 (Schumacher et al. 1999; Kohn and Spear 2000) and/or weathering, generating pellicular
93 patterns (Delvigne 1998).

94 Sector or hourglass zoning (Dowty 1976; Kwak 1981) and oscillatory zoning (see
95 Shore and Fowler 1996 for a review) are more complex patterns. Minerals showing
96 oscillatory zoning patterns exhibit repetitious concentric compositional zones, i.e. quasi-cyclic
97 alternation in the chemical compositions. Oscillatory mineral zoning has been reported from
98 open-system environments (e.g., Jamtveit 1991; Jamtveit and Andersen 1992; Jamtveit et al.
99 1993; Holten et al. 2000) in magmatic, metamorphic and hydrothermal rocks. Occurrences
100 have been found in at least 75 rock-forming and accessory minerals comprising most major
101 chemical groups: silicates (hydrous and anhydrous), sulfides, oxides, halides, carbonates,
102 phosphates and sulfates (Shore and Fowler 1996). The study of magmatic minerals showing

103 oscillatory zoning allows to deepen the understanding of magma evolution during the
104 crystallization of the rock (Putirka and Tepley 2008 and references therein). The best
105 candidate is plagioclase because its composition is sensitive to T, P, and H₂O content of the
106 melt (Shcherbakov et al. 2011). Recent studies interpreted the oscillatory zoning patterns in
107 plagioclase as convection of crystals across distinct zones of the magmatic chamber before
108 eruption (Nicotra and Viccaro 2012), or by frequent replenishments of the magma chamber
109 causing thermal and chemical interactions between melts and the growing crystals
110 (Shcherbakov et al. 2011). Oscillatory zoning patterns in garnet have been extensively studied
111 in order to track the metamorphic P-T-t path (e.g., Jamtveit and Andersen 1992; Garcia-Gasco
112 et al. 2002; Gaidies et al. 2008) or the hydrothermal fluid conditions evolution of skarn
113 deposits (Gaspar et al. 2008). In faults located in low-grade metamorphic environment,
114 minerals showing oscillatory zoning are common (Shore and Fowler 1996). This zoning is
115 due to the effect of large-scale processes (external dynamics) and/or to pattern formation
116 caused by self-organization of the local growth processes (internal dynamic) (Meth and
117 Carlson 2005; Shore and Fowler 1996; Carlson 2005; Gaspar et al. 2008; Zhai et al. 2014).

118 The previous studies on minerals showing oscillatory zoning allow a better
119 understanding of their crystallization mechanisms in magmatic and metamorphic rocks, but
120 are still insufficient to interpret those in phyllosilicates in hydrothermal environments. In most
121 cases, external changes of the fluid compositions are invoked to explain oscillatory zoning
122 patterns (e.g., Holten et al. 1997). In fluid-rich systems, complex zonings are commonly
123 interpreted to reflect changes in fluid composition or varied degrees of fluid buffering (e.g.,
124 Yardley et al. 1991; Beaufort et al. 2005; Jourdan et al. 2009). However, recent experimental
125 studies showed that rapid fluid-flow reactions and ultra-local kinetic effects could lead to
126 fluids with locally extreme non-equilibrium compositions (Borg et al. 2014).

151 The Pyrenean belt is a double-vergence orogenic wedge formed during the collision of
152 the Iberian and European plates between the Late Cretaceous and the early Miocene (e.g.,
153 Muñoz 1992; Roure et al. 1989; Teixell 1998). The south-vergent thrust system comprises
154 imbricated basement thrusts which form the anticlinal stack of the Axial Zone and pass
155 southwards to detachment levels within the sedimentary cover thrust units of the South-
156 Pyrenean Zone (Fig. 1a). The studied area is located in the Pyrenean Axial Zone, in the
157 eastern slope of the Pic-de-Port-Vieux (Fig. 1b). The major structure in this area is the
158 Gavarnie thrust (GT), involving a minimum southward displacement of 11.5 km (Grant 1989)
159 of Upper Paleozoic strata on Hercynian to Lower Paleozoic basement covered with Permo-
160 Triassic and Upper Cretaceous strata (Fig. 1c). The Gavarnie thrust activity is dated from the
161 Priabonian to Rupelian by stratigraphy in the South-Pyrenean foreland basin (Teixell 1996)
162 and to the Priabonian (36.5 ± 1.4 Ma) by ^{40}Ar - ^{39}Ar isotopic dating on authigenic illite from
163 the thrust fault zone (Rahl et al. 2011). The latter authors also report a Maastrichtian (circa 70
164 Ma) age but the Jaca basin stratigraphic organization make it difficult to relate this age to an
165 early thrusting activity (i.e. the future Gavarnie thrust sheet area was tilting northward down
166 to basinal depths at that time, e.g., Teixell 1996). In the Pic-de-Port-Vieux culmination, a
167 secondary thrust occurs in the footwall of the Gavarnie thrust: the Pic-de-Port-Vieux (PPV)
168 thrust (Fig. 2). With a minimum southward displacement of 0.85 km (Grant 1990), the PPV
169 thrusting deformed, and is thus younger than, the Gavarnie thrust and emplaced Triassic
170 pelites/sandstones above Upper Cretaceous dolomitic limestone (Figs. 2 and 3a).

171 Structures and microstructures related to the PPV thrust emplacement have been
172 extensively studied by Grant (1990, 1992). In the hanging-wall of the major thrust surface, a
173 damage zone about 10 m-thick comprises four generations of extensional normal faults (Fig.
174 3c; see Grant 1992 for details). The last generation corresponds to low-angle synthetic normal
175 faults (Fig. 3c) related to the reactivation of the PPV thrust by spreading/gliding inducing

176 shear and extension strain (Grant 1992). During this tectonic episode, previously formed (pre-
177 thrusting and syn-thrusting) high-angle faults were reactivated as conjugated normal faults.
178 The formation of these normal faults records syn-kinematic fluid-rock interactions in chlorite
179 \pm quartz \pm calcite extension veins and shear veins (Fig. 3b, Grant, 1992). Forty samples were
180 collected, for most of them, in faults and veins in the hanging-wall of the PPV thrust. The
181 stars in Figure 3c indicate the positions of zoned chlorite crystals, systematically localized in
182 the largest synthetic faults (labeled A and B in Fig. 3c).

183

184 **Methodological procedures**

185

186

1. Analytical techniques

187 Detailed investigation of textures, microstructures and related variations of chemistry
188 in chlorite was conducted using optical microscopy and scanning electron microscope (SEM)
189 coupled with energy dispersive spectrometer (EDS) analyses. Quantitative chemical analyses
190 were performed by electron probe micro-analysis (EPMA).

191 SEM observations were performed with a JEOL JSM5600 scanning electron
192 microscope coupled with a FONDIS energy dispersive analyzer (EDS) at the Renatech
193 network Femto laboratory (University of Franche-Comté). More detailed observations were
194 made with a JEOL JSM 6400F at the Institut Carnot de Bourgogne (University of
195 Bourgogne).

196 Quantitative chemical analyses of zoned chlorite minerals were performed using two
197 JEOL 8200 EPMA at ISTE (University of Lausanne) and at the Institute of Geological
198 Sciences (University of Bern). X-ray compositional maps were measured using wavelength
199 dispersive spectrometers (WDS) and analytical conditions of 15 keV accelerating voltage, 100
200 nA specimen current, 300-450 ms dwell time and 1 μ m spot size. Punctual analyses were
201 acquired at the Institute of Geological Sciences (University of Bern), using common

202 standards: albite (Si), phlogopite (K), ilmenite (Fe, Ti), orthoclase (Ca, Al), spinel (Mg),
203 tephroite (Mn) and enstatite (Cr) with 15 keV accelerating voltage, 10 nA specimen current
204 and 40 s dwell time.

205 Chemical analyses of unzoned chlorite crystals were performed using a CAMECA
206 model SX100 electron microprobe equipped with five WDS at the University of Montpellier.
207 The microprobe was operated at 20 keV accelerating voltage, with a specimen current of 10
208 nA and a beam diameter of 3 μm . The standards used were albite (Na), Al_2O_3 (Al), Fe_2O_3
209 (Fe), forsterite (Mg), orthoclase (K), TiO_2 (Ti) and wollastonite (Si, Ca) (for the choice of the
210 standards see Merlet and Bodinier 1990).

211 In order to determine the speciation of iron in chlorite crystals, Fe K-edge XANES (X-
212 ray Absorption Near Edge Structure) and XRF (X-ray Fluorescence) data were collected at
213 the BM23 beam-line of the European Synchrotron Radiation Facility (ESRF; Grenoble,
214 France) using the micro-focused experimental setup. The storage ring was operating in the 16-
215 bunch mode with an average current of 75 mA. X-rays were generated using a bending
216 magnet, and monochromatized with a double crystal fixed exit Si(111) monochromator.
217 Micro-focusing KB mirrors were used to focus the beam down to 4 by 4 μm FWHM (Full
218 Width Half Maximum). Data were collected in fluorescence mode using a Vortex silicon-
219 drifted diode located at 85° of the incident X-ray beam. The samples were positioned
220 perpendicular to the X-ray beam to minimize self-absorption (Pfalzer et al. 1999). μ -XRF
221 maps were first recorded at 9 keV, with 10 μm spatial resolution and a dwell time of 0.5 s.
222 Then, μ -XANES spectra were collected at the Fe K-edge for different locations of the XRF
223 maps. Data normalization and pre-peak fits were performed with the XASMAP package,
224 originally dedicated to the dispersive micro-XANES mapping applications (Muñoz et al.
225 2006, 2008). The Fe K-edges were fitted between 7108 and 7118 eV using three pseudo-Voigt
226 functions, following the procedure of Muñoz et al. (2013). In order to derive the speciation of

227 iron, pre-edge calibration was based on the following powdered standards: staurolite
228 ($^{[IV]}Fe^{2+}$), siderite ($^{[VI]}Fe^{2+}$), andradite ($^{[VI]}Fe^{3+}$) and sanidine ($^{[IV]}Fe^{3+}$), according to Wilke et
229 al. (2001). Chlorite crystals were oriented in the magic angle geometry to prevent polarization
230 effects in the XANES and pre-edge regions (i.e. crystal orientation relative to the polarized X-
231 ray beam), in agreement with Muñoz et al. (2013).

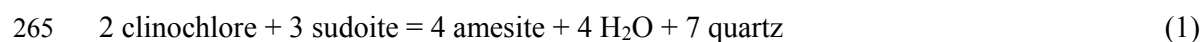
232

233 **2. Data processing and thermometry calculation**

234 X-ray images data were processed using the program XMAPTOOLS 1.6.5 (Lanari et al.
235 2014b). The allocation of each pixel to one mineral phase (e.g., chlorite or quartz) was done
236 using all the elements analyzed by EPMA. Chlorite X-ray raw intensity of Si, Al, Ti, Fe, Mg,
237 Mn, Ca, Na, Cr and K were converted into oxide wt-% compositions SiO_2 , Al_2O_3 , TiO_2 , FeO ,
238 MgO , MnO , CaO , Na_2O , Cr_2O_3 and K_2O using internal standards, i.e. transects of point
239 analyses measured on the same area (de Andrade et al. 2006). Indeed, the reduction of
240 acquisition time at 200 ms per pixel allows significant time saving in the map creation, but
241 requires standardization with well localized spot analyses using a standard EPMA setup. The
242 ‘automatic median’ approach available in XMAPTOOLS was used (Lanari et al. 2014b). The
243 quality of the standardization was tested by comparing the composition of the internal
244 standard and the composition of the corresponding pixel in the X-ray maps. Chlorite structural
245 formulas were then calculated for each pixel using the function available in XMAPTOOLS.
246 This function allows calculating a structural formula on a 14 oxygen-basis by distributing
247 elements on two tetrahedral (T1, T2) and three octahedral sites (M1, M2M3, M4) and
248 assuming equipartition between Fe^{2+} and Mg^{2+} (constant $X_{Mg} = Mg^{2+}/(Mg^{2+}+Fe^{2+})$ on M1,
249 M2M3 and M4). The knowledge of the iron oxidation state ($X_{Fe^{3+}} = Fe^{3+}/(Fe^{3+}+Fe^{2+})$) of
250 chlorite is required to calculate the correct structural formula of chlorite without the
251 hypothesis of $\sum Fe = Fe^{2+}$. It has been shown that incorporation of Fe^{3+} instead of Fe^{2+} may

252 generate important changes of the calculated X_{Mg} and the amount of vacancy (\square) in M1 (Vidal
253 et al. 2005; Lacroix et al. 2012; Lanari et al. 2014a). End-member proportions of amesite,
254 clinochlore, daphnite and sudoite were estimated from the abundance of Al, Mg, Fe^{2+} and \square in
255 the M1 site respectively.

256 Maps of formation temperature can be calculated from the oxide wt-% maps using the
257 different empirical and semi-empirical calibrations available in XMAPTOOLS (Lanari et al.
258 2014b). In this study, we used a calibration which allows the chlorite temperature calculation
259 knowing XFe^{3+} . Among the two recent calibrations using XFe^{3+} adapted to low grade
260 metamorphism context (Inoue et al., 2009 and Lanari et al., 2014a), we used the calibration
261 Chl(1) from Lanari et al. (2014a) that was better constrained, in particular with an adjustment
262 of the standard state thermodynamic properties of sudoite. The calibration of Inoue et al.
263 (2009) gives similar results. The Lanari et al. (2014a) calibration is based on the following
264 chlorite + quartz + water equilibrium:



266 Ideal activities of amesite, clinochlore and sudoite are calculated using a site mixing model
267 for chlorite end-members and $a_{H_2O} = 1$ (Lanari et al. 2014a), which allows the determination
268 of $\ln(K)$ using the following equation:

$$269 \quad \ln(K) = \ln(a_{\text{ames}}^4 / a_{\text{clin}}^2 a_{\text{sud}}^3) \quad (2)$$

270 Chlorite temperatures are then calculated using:

$$271 \quad T_{\text{chlorite}} (\text{°C}) = 172341 / (-R\ln(K) + 315.149) - 273.15 \quad (3)$$

272 An average temperature was calculated from quadrat samples of 20*20 μm (corresponding to
273 400 pixels) using a Monte Carlo technique (1,000 permutations for each pixel corresponding
274 to 400,000 calculations) to simulate the uncertainty of 5% on the XFe^{3+} determined by μ -
275 XANES measurements. The center of the quadrat location was superimposed to the XANES-

276 related point. According to the number of data and the small heterogeneities of the sample, a 1
277 sigma standard deviation appears significant and was calculated for each quadrat.

278

279

Results

280

1 Host rock

281 The Pic-de-Port-Vieux thrust fault zone comprises pelites in the hanging-wall and
282 dolomitic limestone in the footwall (Fig. 4a). Pelite is constituted by phyllosilicates (mainly
283 illite-muscovite, but also chlorite), quartz, and dispersed grains of hematite, apatite, and rutile
284 (Fig. 4b); rare calcite is detected. Near the major thrust surface and along synthetic faults, the
285 red pelite turns to a greenish color. The green pelite is characterized by the absence of
286 hematite (Fig. 4c). Illite-muscovite is still abundant. Matrix quartz displays an elongated
287 morphology with long axis parallel to schistosity. Chlorite crystallized commonly along
288 extension veinlets and shear veinlets (Fig. 4c). In the footwall, the dolomitic limestone is
289 composed of euhedral dolomite crystals in a microcrystalline calcite matrix with rare iron
290 oxides (Figs. 4d). Approaching the thrust surface, dolomitic limestone is progressively
291 mylonitized (Fig. 4a). Dolomite is progressively dissolved (Figs. 4e and 4g) and secondary
292 calcite precipitated in dolomitic ghosts and cracks (Fig. 4f). Within the mylonite, dolomite
293 occurs only as anhedral remains in calcite.

294

295

2. Chlorite description

296 Two types of chlorite minerals crystallized in the Pic-de-Port-Vieux veins related to
297 synthetic fault activity. Figures 5a and 5b shows a syntaxial extension vein filled by quartz +
298 chlorite ± calcite. In these veins, chlorite crystals are preferentially developed along the vein-
299 host rock interface and quartz crystals occur as elongated crystal with axis perpendicular to
300 the vein boundaries. These textural observations suggest that chlorite nucleated first in contact

301 to the host-pelite and grew toward the center of the vein with a growth direction parallel to the
302 schistosity planes. When a vein crosses pelite and silt alternating layers, chlorite is
303 preferentially present along the pelitic layers (Figs. 5a, 5b). In these extension veins, quartz
304 shows parallel inclusion bands (dust or secondary minerals inclusions parallel to the vein
305 wall) and serrated grain boundaries (called “radiator structure” within Bons et al. 2012)
306 indicating a crack-seal mechanisms of vein formation (Ramsay, 1980). The second type of
307 vein corresponds to shear vein filled by quartz, chlorite and locally calcite (Figs. 5c and 5d).
308 The quartz exhibits blocky crystals without any preferential orientation. Moreover, chlorite
309 occurs sometime in these shear veins as pseudo-uniaxial plates arranged in rosette-shaped
310 aggregates. These structures suggest that chlorite is followed by quartz during precipitation of
311 these minerals in open fractures. These two vein types are cogenetic and in accordance with
312 the orientation of the principal axes of the local field stress (Fig. 5e).

313 SEM images show that rosette chlorite from shear veins displays oscillatory zoning
314 pattern (Fig. 6a) while chlorite from extension veins is homogenous. The rosette-like
315 morphology of chlorite can be seen on Figures 6b and 6c. Both images show that the rosettes
316 correspond to the aggregation of individual platelet crystals composed of stacks of layers 20-
317 50 μm thick and 100-200 μm long. This morphology suggests that chlorite grew in an open
318 space and that quartz crystallization postdates chlorite growth as discussed above. However,
319 the contacts between quartz and chlorite grains are devoid of any corrosion texture (Figs. 6a,
320 6c).

321 Within a single vein, all chlorite aggregates exhibit similar zoning patterns with the
322 same number of contrasted layers. However, the thickness of the layers can vary from one
323 rosette to another (Fig. 6a). At higher magnifications, the zonation appears complex with
324 heterogeneous contrasts at the micrometric scale (Fig. 6d). The contrast distribution appears
325 as stair steps in section, seeming to follow the growth development of the chlorite crystals

326 (layer by layer or by spiral growth) but with preferential growth directions perpendicular to c^*
327 (F face is (001)) (Fig. 6e).

328

329

3. Chlorite chemistry

330 Two X-ray images were performed on aggregates of oscillatory zoned chlorite from a
331 shear vein using EPMA (maps A and B, Fig. 7). Five zones are distinguishable in the two
332 aggregates. Zone 1 is located in the core of the aggregate and zone 5 in the external rim (Figs.
333 7b). Backscattering oscillatory contrasts are caused by FeO and MgO content variation (Figs.
334 7c; 7d). FeO and MgO contents display strong opposite behaviors with absolute variations up
335 to 7 wt-%. FeO ranges from 16 to 23 wt-% and MgO from 21 to 13 wt-%. SiO₂ and Al₂O₃
336 contents show smaller variations (less than 2 wt-%). SiO₂ ranges from 25 to 27 wt-% and
337 Al₂O₃ from 22 to 24 wt-% (Figs. 7e and 7f). There is a slight increase of Al₂O₃ from zone 1
338 (core) to zone 4, whereas the external rim (zone 5), like zone 1, displays lower Al₂O₃. SiO₂
339 content is almost constant in all zones, except in zone 2 where it is about 2 wt-% higher. X-
340 ray image from chlorite extension veins was not performed due to the chemical homogeneity
341 of these minerals.

342 Based on both μ -XRF and EPMA chemical maps, μ -XANES measurements were
343 performed in five spots along a radius of zoned chlorite mineral that was previously analyzed
344 (Fig. 8a). Normalized spectra are displayed in Figure 8b. Spectral signatures are typical of
345 clinocllore (e.g., Muñoz et al. 2013). Their similar shape suggests that similar crystal
346 orientations are considered for these measurements. However the Xan1 spectrum shows a
347 slightly different shape suggesting a small change in orientation, mostly because it is located
348 in the center of the concentric crystal. According to the work of Muñoz et al. (2013), this
349 shape might lead to a slight over-estimation of the XFe^{3+} (i.e. $Fe^{3+}/\sum Fe$) from the pre-edge

350 data reduction. But according to the same authors, this over-estimation should not exceed
351 0.07, which is in the same range of the typical accuracy of the method (± 0.05).
352 Figure 8c shows the baseline-subtracted pre-edge peaks (white circles), together with their
353 best fits (solid lines) and pseudo-voigt peaks used for deconvolution (dotted lines). Results in
354 terms of integrated area and centroid energy positions are displayed in the variogram of
355 Figure 8d. The accuracy of the centroid value is ± 0.05 eV (Muñoz et al., 2013). This
356 variogram also shows reference values obtained for the standard compounds (white circles)
357 used for the calibration of the data (see Wilke et al. 2001 for details). Results obtained for the
358 different locations along the radius of the crystal all plot in between the two octahedral Fe^{2+} –
359 Fe^{3+} end-members, in agreement with the structure of clinocllore crystals (i.e. Fe located in
360 octahedral sites). The conversion into XFe^{3+} show periodic variations ranging from 23 to 44%
361 ($\pm 5\%$). In addition to the integrated area and the centroid position values, Table 1 shows the
362 XFe^{3+} values obtained from XANES normalization.

363 Assuming that each zone has homogeneous iron state oxidation, μ -XANES
364 measurements (Table 1) coupling with quantitative oxide wt-% composition maps (Fig. 7)
365 were used to calculate structural formulas for each pixel of chlorite (from a shear vein) using
366 *Chl-StructForm.m* function of XMAPTOOLS (Lanari et al. 2014b). XFe^{3+} values from chlorite
367 Map A are assumed to be the same as for Map B. In each zone from chlorite maps A and B,
368 representative structural formulas were given in Table 2 and plotted in Figure 9. The average
369 composition in map A are:

370 $[\text{Si}_{2.54}\text{Al}_{1.46}\text{O}_{10}](\text{Al}_{1.30}\text{Fe}^{2+}_{1.12}\text{Fe}^{3+}_{0.81}\text{Mg}_{2.44}\square_{0.32})(\text{OH})_8$ in zone 1,

371 $[\text{Si}_{2.61}\text{Al}_{1.39}\text{O}_{10}](\text{Al}_{1.33}\text{Fe}^{2+}_{1.14}\text{Fe}^{3+}_{0.42}\text{Mg}_{2.92}\square_{0.18})(\text{OH})_8$ in zone 2,

372 $[\text{Si}_{2.58}\text{Al}_{1.42}\text{O}_{10}](\text{Al}_{1.35}\text{Fe}^{2+}_{1.15}\text{Fe}^{3+}_{0.59}\text{Mg}_{2.62}\square_{0.26})(\text{OH})_8$ in zone 3,

373 $[\text{Si}_{2.60}\text{Al}_{1.40}\text{O}_{10}](\text{Al}_{1.43}\text{Fe}^{2+}_{1.12}\text{Fe}^{3+}_{0.33}\text{Mg}_{2.92}\square_{0.18})(\text{OH})_8$ in zone 4,

374 $[\text{Si}_{2.56}\text{Al}_{1.44}\text{O}_{10}](\text{Al}_{1.34}\text{Fe}^{2+}_{1.08}\text{Fe}^{3+}_{0.85}\text{Mg}_{2.34}\square_{0.37})(\text{OH})_8$ in zone 5.

375 Two groups can be distinguished from these results. The first group includes structural
376 formulas from zones 1, 3 and 5; they correspond to Fe-rich chlorite (Fig. 9a). Their
377 compositions are closed to the unzoned chlorite (homogenous, without chemical variation)
378 from synkinematic extension veins and correspond to 40% of clinocllore+daphnite, 40% of
379 amesite and 20% of sudoite (Fig. 9b). The second group is enriched in Mg and corresponds to
380 the analyses of the zones 2 and 4 (Fig. 9a). Their compositions are out of the field of unzoned
381 chlorite and correspond to 20-30% of clinocllore+daphnite, 40% of amesite and 30-40% of
382 sudoite (Fig. 9b). The differences between the two chlorite groups are the Mg- Σ Fe
383 substitution in octahedron (Fig. 9a) and also a di-trioctahedral substitution (Fig. 9b). No
384 Tschermak substitution has to be invoked to explain the chemical variations.

385 Chlorite structural formulas are calculated from each pixel of the analyzed area, allow
386 building of Fe²⁺, Fe³⁺ maps (Figs. 10a and 10b). In zones 1 and 5, Fe²⁺ content is equal to 1
387 a.p.f.u. while it reaches 1.1 to 1.2 in zones 2, 3 and 4. Fe³⁺ is equal to 0.8 a.p.f.u. in zones 1
388 and 5; 0.7 a.p.f.u. in zone 3 and 0.6 a.p.f.u. in zones 2 and 4. Fe²⁺ content shows small
389 variations probably due to edge effect (the XFe³⁺ between two successive zones probably
390 gradually changing), it may be considered constant throughout the crystallization. In contrast,
391 Fe³⁺ content displays strong variations. These results highlight an iron redox change during
392 crystal growth, with a cyclic alternation between more ferrous and more ferric chlorite layers.

393 In order to test whether the FM substitution is at the origin of the zonation between Fe-
394 rich and Mg-rich layers, an $X_{Mg} = Mg^{2+} / (Mg^{2+} + Fe^{2+})$ map has been produced (Fig. 10c). In
395 agreement with structural formulas (Table 2), X_{Mg} map (Fig. 10c) does show significant
396 variation. X_{Mg} is constant around 0.72 ± 0.03 .

397

398

4. Temperature map

399 Temperature map (Fig. 10d) is derived using the Eq. (3), which is the thermometer
400 Chl(1) from Lanari et al. (2014a) in XMAPTOOLS using the XFe^{3+} measurements for each
401 zone (Table 1). In both maps A and B, average temperatures with associated uncertainty were
402 estimated and are reported in Table 2. For both aggregates, temperatures were estimated at
403 $307^{\circ}C \pm 19^{\circ}C$ to $347^{\circ}C \pm 27^{\circ}C$ in zone 1, followed by $370^{\circ}C \pm 36^{\circ}C$ to $396^{\circ}C \pm 29^{\circ}C$ in
404 zone 2, $338^{\circ}C \pm 24^{\circ}C$ to $354^{\circ}C \pm 23^{\circ}C$ in zone 3, $402^{\circ}C \pm 49^{\circ}C$ to $405^{\circ}C \pm 41^{\circ}C$ in zone 4
405 and $316^{\circ}C \pm 20^{\circ}C$ to $320^{\circ}C \pm 22^{\circ}C$ in zone 5. Chlorite crystals A and B display the same
406 temperature evolution: they show a series of warming and cooling cycles during
407 crystallization. The temperature oscillation (up to $100^{\circ}C$ range) is correlated to the chemical
408 zonation: Mg-rich layers correspond to hot areas while Fe-rich layers correspond to cold ones.

409

410

Discussion

411 Chlorite chemical zoning described above is characterized by Fe-Mg chemical
412 variations and increase in Fe^{3+} in the Fe-rich layers. These chemical changes may reflect
413 changes of local equilibrium conditions experienced during PPV thrust activity. Several
414 parameters such as pressure (P), temperature (T), oxygen fugacity (f_{O_2}), water activity (a_{H_2O}),
415 redox conditions (XFe^{3+}) and bulk system composition (including bulk-rock and fluid
416 compositions) could be invoked to explain the zoning. In the section below, we discuss the
417 effect of those parameters on the chlorite compositions in order to discriminate which can
418 have played a critical role during the growth of these aggregates.

419

1. Significance of chemical and temperature oscillations registered by PPV thrust

420

chlorite aggregates

421

422 Chlorite chemistry can be a very good indicator of temperature of crystallization (e.g.,
423 Cathelineau and Nieva 1985; Cathelineau 1988; de Caritat et al. 1993; Vidal et al. 2001, 2005,

424 2006; Inoue et al. 2009; Bourdelle et al. 2013; Lanari et al. 2014a). In this study, the
425 calibration *Chl(1)* of Lanari et al. (2014a) is used to calculate the formation temperature of
426 chlorite for a known XFe^{3+} content (obtained by μ -XANES). Temperature oscillations
427 between $\sim 310^{\circ}C$ and $\sim 400^{\circ}C$ are found in correlation to chemical variations for the two
428 studied chlorite aggregates. The core of the chlorite aggregates (zone 1) and the last rim (zone
429 5) with low Mg and high Fe^{3+} chemical composition recorded the lowest temperatures
430 ($\sim 310^{\circ}C$). These two zones correspond to the first and last stages of crystallization,
431 respectively. Between these two zones (i.e., zones 2, 3 and 4) the crystallization temperature
432 oscillates between 350 - $400^{\circ}C$ with the highest temperatures corresponding to the layers with
433 the highest Mg and lowest Fe^{3+} contents, respectively.

434 The 1σ standard deviation on the average temperature of each growing zone is
435 reported in Table 2 and Figure 11. Such large errors could indicate that all the zones
436 crystallized around $350 \pm 50^{\circ}C$ if this standard deviation is considered to be representative of
437 the analytical uncertainty. However, temperature differences are significant between the
438 different zones as supported by the temperature map in Fig. 10d. The large 1σ deviations
439 calculated in this study are caused by the ultra-local chemical variability occurring within
440 each zone. As the standard deviation on the temperature is calculated from a local area (see §
441 methods), outliers such as grain boundaries or heterogeneities may cause a large dispersion.
442 The temperature map in Fig. 10d supports that at the scale of each growth zone, the
443 temperature variation is smaller than around $\pm 25^{\circ}C$. Thus, temperature differences
444 highlighted in this study between the different growth zones 1-5, 3 and 2-4 are significant.
445 Although the averages temperatures give values from $310 \pm 50^{\circ}C$ to $400 \pm 50^{\circ}C$, it is more
446 accurate to consider a difference of at least $50^{\circ}C$ between the two populations because of the
447 absolute uncertainty of thermodynamic models and mineral compositions.

448 The lowest temperatures ($310 \pm 50^\circ\text{C}$) recorded during the first and the fifth stages of
449 chlorite growth are similar to those calculated for unzoned chlorite located in extension and
450 shear veins from the same area (Fig. 9a). These temperatures are consistent with temperature
451 estimation of $250\text{-}300^\circ\text{C}$ based on fluid inclusion microthermometry on quartz from extension
452 vein in the PPV thrust (Grant et al. 1990; Banks et al., 1991; McCaig et al., 2000). They are
453 also consistent with stable isotopic data on quartz and chlorite from the same area which
454 indicate a temperature of $320^\circ\text{C} \pm 30^\circ\text{C}$ (Lacroix and Vennemann, 2015) and with carbonate
455 footwall temperature obtained with Raman spectroscopy of carbonaceous material (work in
456 progress). In contrast, chlorite layers with higher Mg content are probably formed at higher
457 temperature: $400 \pm 50^\circ\text{C}$. The thermometry results suggest that the minimum ΔT between two
458 successive layers is about $20\text{-}30^\circ\text{C}$ while the likely ΔT in all the chlorite is about $50\text{-}80^\circ\text{C}$.
459 Such temperature variation is discussed in detail in the following section.

460

461 **2. External and internal factors for chemical zonation**

462 Recent studies based on experimental fluid mineral reactions demonstrate that zoning
463 of mineral compositions does not always reflect the evolution of fluid composition (Borg et
464 al. 2014). These authors showed that during rapid fluid-rock reactions, ultra-local fluid
465 composition variation can form complex mineral zoning patterns, even when the overall
466 system is highly fluid-buffered. Wang and Merino (1992) proposed a dynamic model,
467 autonomously able to produce oscillatory zoning of trace elements in calcite without changes
468 in bulk water chemistry. In this model, the growth-induced H^+ buildup at the growth surface
469 of calcite making the surface more positive, thus repelling inhibited cations (such as Mn^{2+})
470 and accelerating the growth rate. The increase in growth rate in turn further accelerates H^+
471 accumulation (positive feedback) until the Ca^{2+} concentration becomes depressed next to the
472 surface and slows down the crystallization. Then, H^+ diffusion in fluid makes the surface less

473 positive (or even negative) and allows restarting calcite crystallization with incorporation of
474 inhibiting cations. Another growth cycle is triggered. Previous studies in the PPV thrust
475 reveal a circulation of oilfield brines, highly concentrated in ions (Banks et al. 1991). As the
476 growth of chlorite aggregate is probably very rapid, ultra-local fluid disequilibrium cannot be
477 excluded to explain a part of the observed zonation. However, the chemical oscillation display
478 similar patterns at the vein scale suggesting large crystallization volumes (e.g. Fig. 6a). The
479 scale of zoning is very large and shows significant chemical contrasts. This suggests that
480 oscillatory zoning patterns are not due to local kinetic effects in the PPV thrust faults but to an
481 external parameter such as the variation of the oxygen fugacity.

482 Beaufort et al. (2005) described zoned chlorite spherules of hydrothermal origin in
483 sandstones near the uranium deposits of the East Alligator Rivers field in Australia. They
484 interpreted the chemical oscillatory zoning in Fe and Mg as the result of periodic changes in
485 physico-chemical condition of the hydrothermal solution during the crystallization process.
486 These authors have performed microprobe measurements to know the chlorite chemistry; they
487 showed significant variations in Mg but were not able to estimate the $X_{Fe^{3+}}$ which would
488 have allowed a comparison with our data. In the present study, microprobe mapping of
489 chlorite chemistry (atom per formula unit, Fig. 10b) shows significant variations in Fe^{3+} (from
490 0.6 to 0.75 a.p.f.u.) during the crystallization. Highest $Fe^{3+}/\sum Fe$ values correspond to lowest
491 temperatures of chlorite formation. Several authors (Vidal et al. 2006; Tarantola et al. 2009;
492 Grosch et al. 2012; Lanari et al. 2012; Cantarero et al. 2014) found similar correlation
493 between $(Fe^{3+}/\sum Fe)_{chlorite}$ and temperature. In all these studies $(Fe^{3+}/\sum Fe)_{chlorite}$ was indirectly
494 estimated using the Vidal et al. (2005, 2006) approach. In a review paper, Lanari et al.
495 (2014a) found similar trend using both measured $(Fe^{3+}/\sum Fe)_{chlorite}$ and estimated $(Fe^{3+}/\sum Fe)_{chlorite}$
496 using the approach of Vidal et al. (2005, 2006). In a $Fe^{3+}/\sum Fe$ versus temperatures
497 diagram (Fig. 11), Lanari et al. (2014a) identified two main trends using chlorite data reported

498 in the literature and calculation from Vidal et al. (2005, 2006). Both trends correspond to
499 chlorite formed under different redox condition, i.e. various samples where chlorite
500 crystallized under less oxidized or more oxidized conditions (see continuous and dashed
501 curves in Fig. 11 respectively). According to these authors, for a given fO_2 , chlorite formation
502 temperature may control the amount of Fe^{3+} input in the structure. In other words, the amount
503 of Fe^{3+} cannot be considered alone without a formation temperature as a proxy for the redox
504 conditions. Estimated T and measured $Fe^{3+}/\Sigma Fe$ from chlorite of PPV thrust have been
505 reported in this diagram, they are located just above the more oxidized trend (Fig. 11). This
506 result implies that the $Fe^{3+}/\Sigma Fe$ variations of chlorite during its crystallization are mainly
507 caused by temperature variations. The redox conditions (fO_2) are the same during the chlorite
508 crystallization history. Indeed, if the fO_2 in the fluid would have change during chlorite
509 growth, the point analyses would be more scattered on both redox trends (e.g., arrows in Fig.
510 11).

511

512 **3. Origin of oscillatory zoned chlorite aggregates in the PPV thrust veins**

513

513 Previous data and model:

514 Chemistry, source, behavior and P-T conditions of fluids have been previously
515 investigated from fluid inclusions performed in PPV thrust quartz veins (Grant et al. 1990;
516 Banks et al. 1991; McCaig et al. 1995). Synthesized in McCaig et al. (2000), these analyses
517 reveal at least two distinct fluids. Both of them are hypersaline brines (Banks et al. 1991) with
518 a high Br/Cl ratio indicating seawater evaporation with halite precipitation origin (Banks et al.
519 1994). These brines could have been derived from the upper Triassic evaporites and stored in
520 the lower Triassic redbeds (McCaig et al. 2000). Part of this formation water could have been
521 stored in another rock, such as the Devonian phyllites or the Silurian graphitic slates, inducing
522 a change in the isotopic signature of the fluid (Banks et al. 1991). However, the latter

523 interaction has not been certified because no sample carried from local rocks has sufficiently
524 elevated ratio of all the Pb isotopes to explain the fluid inclusions data (McCaig et al. 2000).
525 According to (Grant 1989), chemical zonation in chlorite could be due to a mixing of two
526 distinct fluids. Reducing fluid interactions with Triassic pelites would permit the release of
527 Fe^{3+} by hematite dissolution along the PPV thrust and synthetic faults (Fig. 3c) (Rumble
528 1976; Beaufort et al. 1992, 2005). Furthermore, the fluid interaction with limestone allows the
529 release of Mg by dolomite dissolution (e.g., Figs. 4f, 4g).

530 Fluid inclusion microthermometry indicates temperatures never exceeding 300°C
531 during quartz vein formation (Grant et al. 1990; Banks et al. 1991) and fluid pressure
532 comprised between 1.5 and 2 kbar (Grant 1990), corresponding to a burial depth of 5-7.5 km.
533 Furthermore, measured homogenization temperatures (T_m) define two fluid populations that
534 have been interpreted as a variation of the pressure of 600 bar due to fault valve mechanism
535 (Grant et al. 1990; Banks et al. 1991, McCaig et al. 2000). Indeed, fault-valve process may
536 cause abrupt fluid pressure fluctuations during the thrust activity (Sibson 1990) and have been
537 highlighted by crack-seal structures, open-space filling textures of the quartz + chlorite ±
538 calcite veins and distribution of inclusions in quartz.

539

540 *New data and model:*

541 According to the present study, oscillatory zoned chlorite from the PPV thrust records
542 cyclic changes in temperature without any change of the fluid redox condition or kinetic
543 disequilibrium. The composition map reported in Figure 10c indicates that X_{Mg}
544 ($\text{Mg}^{2+}/(\text{Fe}^{2+}+\text{Mg}^{2+})$) in chlorite does not vary significantly within analytical uncertainties (X_{Mg}
545 = 0.70 ± 0.3) during the aggregate growth. These results suggest that the X_{Mg} of the system
546 does not change during the crystallization of chlorite (Lanari et al. 2014a and references
547 therein), i.e. the chemical composition of the mineralizing fluid remains constant. Indeed,

548 chlorite is very sensitive to bulk composition changes and its X_{Mg} would be modified in case
549 of alternation of two fluids chemistries during crystallization.

550 Thus, each vein containing oscillatory chlorite recorded distinct fluid flow history
551 implying a variation of the number and intensity of pulses, but also a variation in the kinetics
552 of cooling and crystallization. On the other hand, fluid inclusions from PPV thrust quartz
553 veins reveal temperatures from 250 to 300°C, never higher than 325°C (Grant et al. 1990;
554 Banks et al. 1991, McCaig et al. 2000). Several hypotheses can be raised on these differences:
555 (i) Quartz and zoned chlorite may not be strictly cogenetic. Indeed, in shear veins where
556 zoned chlorites formed, chlorite rosettes are always located against the walls of the veins
557 while quartz is in the center of the veins and fills the open spaces between the chlorite
558 rosettes, suggesting that quartz precipitation postdated chlorite formation. In these conditions,
559 quartz fluid inclusions do not represent the chlorite formation conditions. (ii) The two fluid
560 populations recorded by the fluid inclusion study could be related to temperature variation
561 instead of pressure variation, as evocated in Grant et al., (1990). (iii) Fluid inclusion and
562 chlorite sampling was not performed in similar veins. Chlorite sampled in crack-seal
563 extension veins and small shear veins gives similar to those obtained by fluid inclusions. In a
564 crack-seal vein, the opening of the crack (before the seal) is very small (of the order of 50
565 microns or less), the opening mechanism is relatively slow and thus it is impossible to keep a
566 thermal imbalance at this scale. Therefore, crack-seals would likely form during interseismic
567 periods (build-up of stress in the seismic valve model). In contrast the large shear veins that
568 are characterized by blocky texture would form during more dynamic rupture likely being the
569 break seismic (as suggested by Boullier and Robert, 1992). Thus, crack-seal veins open
570 progressively and slowly (opening speed almost equal to the speed of healing, if we integrate
571 all the small increments "cracks" and "seal"). By contrast, large shear veins can be opened by

572 large jolts as suggested by the blocky quartz texture (Figs. 5c, 5d) allowing chlorite
573 crystallization in thermal disequilibrium with host rock.

574

575 *How to get hot fluid inputs?*

576 The results discussed above suggest that oscillatory zoned chlorite recorded the
577 temperature variation of one fluid, sometime hot (more than 350°C) probably episodic and
578 minor; sometime colder reflecting a cooling down to lithostatic equilibrium around 300°C.
579 The question is how to explain this fast input of hotter fluid? No igneous activity has been
580 reported in this area at this time, so the uniqueness way to introduce a much hotter fluid into
581 the vein would be to move fluid up from deeper fault portions. For a geothermal gradient
582 close to 30°C/km as estimated in the Jaca basin (Lacroix et al. 2011), at least 2 km of vertical
583 movement, representing 4 km of fluid transport along the Gavarnie thrust considering a dip
584 about 30°, must be invoked. Such fluid transport scale implicates that the fluid had to ascend
585 through a narrow channelway (1) with no loss of heat in contact to the surrounding rocks,
586 implicating quasi-instantaneous emplacement (a 1cm thick vein will lose most of its excess
587 heat by conduction in few minutes (e.g., Carslaw et al., 1959)); (2) with channelway heating
588 and in this case the whole chlorite rosette and surrounding rocks for at least several meters
589 will have experienced the peak temperatures estimated. Several investigations can be explored
590 to try to resolve this paradox. It is possible that the geothermal gradient changed at greater
591 depth, reducing the fluid migration distance. Fault-valve process increases the fracture
592 permeability for fluid draining and related shear vein formation. Such process permits a high
593 temperature fluid discharge in open veins followed by a cooling event in contact to host rock
594 (pelite). This mechanism has been observed by several authors. For example Cantarero et al.
595 (2014) describe high geothermal gradients (50°C/km minimum) along fractures. Temperature
596 measurements in a fault after an earthquake indicate a slight positive anomaly that can be

597 interpreted by viscous heating (e.g., Brodsky et al., 2009). Strain heating results from the
598 conversion of mechanical energy into heat during progressive deformation and, for some
599 models indicate that temperature rises of a few hundred degrees can be expected in major
600 thrust sheets (Brun and Cobbold 1980; Souche et al., 2013). There is not strain heating
601 evidence in the Pic-de-Port-Vieux thrust, so the ΔT ($>20\text{-}30^\circ\text{C}$) recorded by the chlorite
602 rosettes is most likely related to an increase in the permeability of the fault rock for hot fluids
603 flowing from deeper areas. Fluid flows associated to earthquakes reveal variations of flow
604 rate and fluid sources (e.g., Toutain et al. 1997, 2006; Manga et Wang 2007). For example,
605 Mogi et al. (1988) show hot spring temperature variations related to earthquakes occurrences.
606 These temperature variations can be explained by a model of earthquake-enhanced
607 permeability due to the dislodging of obstacles from clogged fluid channels, such as pre-
608 existing fractures. Unclogged fractures act to breach hydrologic barriers (such as aquitards)
609 and connect otherwise isolated aquifers or other fluid sources, causing fluid source switching
610 and/or mixing (Wang et Manga 2010). It is thus possible that the ΔT measured in zoned
611 chlorite from the PPV thrust reflects the discharge of a deeper and hotter aquifer by stronger
612 fluid flow during large earthquakes.

613

614

Implications

615 (1) This study shows how important is the measure of XFe^{3+} in low-grade
616 metamorphism chlorite to study their chemistry, because the proportion of Fe^{3+} can locally
617 reach up to 45% of the total amount of iron. To measure $\text{Fe}^{3+}/\Sigma\text{Fe}$ ratio XANES and
618 Mössbauer techniques may be used, but microanalyses can only be performed using μ -
619 XANES spectroscopy.

620 (2) With the development of chlorite thermometry, several models have recently
621 emerged including XFe^{3+} estimation (e.g., Vidal et al. 2005, 2006) or requiring the knowledge

622 of the XFe^{3+} (Inoue et al. 2009; Lanari et al. 2014a). These two semi-empirical geo-
623 thermometers were calibrated with the idea that iron in chlorite must be expressed as $Fe_{tot} =$
624 $Fe^{2+} + Fe^{3+}$. As demonstrated by Figure 11 there is no general relation between Fe^{3+} and T
625 except for given redox conditions (in this case, XFe^{3+} increases with decreasing T). The
626 results of this study confirm the existence of a highly oxidized trend that was before only
627 predicted by modeling and prove that XFe^{3+} in chlorite can reach 45%. This result
628 demonstrates that chlorite may be used to investigate the redox conditions in low-grade
629 metamorphic rocks and hydrothermal environments. Fe^{3+} end-members must be defined and
630 should be used in the framework of thermodynamic modeling. This is an important domain
631 for further research in chlorite geo-thermometry and the results reported in this study provide
632 first importance data to adjust such models.

633 (3) The quantitative micro-mapping technique used in this study is fundamental to
634 highlight variations of chemistry in 2D at the thin section scale. This method allows to
635 measure the chemical heterogeneity of minerals and to calculate maps of formation
636 temperature which are critical to see the relations between T and the geometry of the crystals.
637 Here we demonstrate that this method may be coupled with single-spot μ -XANES analyses to
638 generate maps of structural formulas (Fig. 10) with variable XFe^{3+} . This offers new
639 opportunities to apply the same strategy using other high-precision instruments such as La-
640 ICP-MS or SIMS.

641 (4) This paper demonstrates that the temperature of the fluid within a vein is an
642 important parameter that controls the composition of the growing minerals. The zoned
643 chlorite crystals record changes that are caused by hot fluids pulses intercalated with cooling
644 periods. The process of fault-valve behavior is an important process to explain the
645 crystallization of this chlorite in the PPV thrust veins. The detailed study of phyllosilicates
646 can help to better understand fluid flows in a fault and to investigate the relations of such

647 flows with the seismic activity of the thrust. The future results obtained using the strategy
648 detailed in this study may have large implications in geosciences.

649

650

Acknowledgements

651 This work was supported by the French RENATECH network and its FEMTO-ST
652 technological facility. Micro-XANES measurements were supported by In-House research
653 program of the BM23 beam-line of the ESRF. We particularly thank O. Mathon for his
654 crucial help during data acquisition. We address our thanks to E. Courgeon, guardian of
655 Barroude refuge for his pictures and his hospitality and to O. Fabbri for English proofreading.
656 Authors warmly thank A.M. Boullier for discussions on the genetic model. We also thank the
657 editor D. Dyar and detailed reviews by O. Tarantola and A. McCaig which allowed improving
658 this manuscript, especially the discussion section.

659

660

References

661 Banks, D., Davies, G., Yardley, B.W., McCaig, A., and Grant, N. (1991) The chemistry of brines
662 from an Alpine thrust system in the Central Pyrenees: An application of fluid inclusion
663 analysis to the study of fluid behaviour in orogenesis. *Geochimica et Cosmochimica Acta*, 55,
664 1021–1030.

665 Beaufort, D., Patrier, P., Laverret, E., Bruneton, P., and Mondy, J. (2005) Clay Alteration
666 Associated with Proterozoic Unconformity-Type Uranium Deposits in the East Alligator
667 Rivers Uranium Field, Northern Territory, Australia. *Economic Geology*, 100, 515–536.

668 Blanco-Quintero, I.F., García-Casco, A., and Gerya, T.V. (2011) Tectonic blocks in serpentinite
669 mélange (eastern Cuba) reveal large-scale convective flow of the subduction channel.
670 *Geology*, 39, 79–82.

- 67Borg, S., Liu, W., Pearce, M., Cleverley, J., and MacRae, C. (2014) Complex mineral zoning
672 patterns caused by ultra-local equilibrium at reaction interfaces. *Geology*, G35287.1.
- 67Bos, B., and Spiers, C.J. (2001) Experimental investigation into the microstructural and
674 mechanical evolution of phyllosilicate-bearing fault rock under conditions favouring pressure
675 solution. *Journal of Structural Geology*, 23, 1187–1202.
- 67Boullier, A.-M., and Robert, F. (1992) Palaeoseismic events recorded in Archaean gold-quartz vein
677 networks, Val d'Or, Abitibi, Quebec, Canada. *Journal of Structural Geology*, 14, 161–179.
- 67Bourdelle, F., Parra, T., Beyssac, O., Chopin, C., and Vidal, O. (2013) Clay minerals as geo-
679 thermometer: A comparative study based on high spatial resolution analyses of illite and
680 chlorite in Gulf Coast sandstones (Texas, U.S.A.). *American Mineralogist*, 98, 914–926.
- 68Brodsky, E.E., Rowe, C.D., Meneghini, F., and Moore, J.C. (2009) A geological fingerprint of
682 low-viscosity fault fluids mobilized during an earthquake. *Journal of Geophysical Research:*
683 *Solid Earth* (1978–2012), 114.
- 68Brun, J.P., and Cobbold, P.R. (1980) Strain heating and thermal softening in continental shear
685 zones: a review. *Journal of Structural Geology*, 2, 149–158.
- 68Buatier, M.D., Lacroix, B., Labaume, P., Moutarlier, V., Charpentier, D., Sizun, J.P., and Travé, A.
687 (2012) Microtextural investigation (SEM and TEM study) of phyllosilicates in a major thrust
688 fault zone (Monte Perdido, southern Pyrenees): impact on fault reactivation. *Swiss Journal of*
689 *Geosciences*, 105, 313–324.
- 69Cantarero, I., Lanari, P., Vidal, O., Alías, G., Travé, A., and Baqués, V. (2014) Long-term fluid
691 circulation in extensional faults in the central Catalan Coastal Ranges: P–T constraints from
692 neoformed chlorite and K-white mica. *International Journal of Earth Sciences*, 103, 165–188.
- 69Carslaw, H.S., Jaeger, J.C., and others (1959) *Conduction of heat in solids* Vol. 2. Clarendon Press
694 Oxford.

- 696 Cathelineau, M. (1988) Cation site occupancy in chlorites and illites as a function of temperature.
696 Clay Minerals, 23, 471–485.
- 697 Cathelineau, M., and Nieva, D. (1985) A chlorite solid solution geothermometer the Los Azufres
698 (Mexico) geothermal system. Contributions to Mineralogy and Petrology, 91, 235–244.
- 699 Chester, F.M., Evans, J.P., and Biegel, R.L. (1993) Internal structure and weakening mechanisms
700 of the San Andreas Fault. Journal of Geophysical Research: Solid Earth, 98, 771–786.
- 701 Dare, S.A.S., Barnes, S.-J., Prichard, H.M., and Fisher, P.C. (2011) Chalcophile and platinum-
702 group element (PGE) concentrations in the sulfide minerals from the McCreedy East deposit,
703 Sudbury, Canada, and the origin of PGE in pyrite. Mineralium Deposita, 46, 381–407.
- 704 De Andrade, V., Vidal, O., Lewin, E., O'Brien, P., and Agard, P. (2006) Quantification of electron
705 microprobe compositional maps of rock thin sections: an optimized method and examples
706 RID C-2856-2009. Journal of Metamorphic Geology, 24, 655–668.
- 707 De Caritat, P., Hutcheon, I., and Walshe, J.L. (1993) Chlorite geothermometry; a review. Clays
708 and Clay Minerals, 41, 219–239.
- 709 De Grave, E., Vandenbruwaene, J., and Bockstael, M.V. (1987) ^{57}Fe Mössbauer spectroscopic
710 analysis of chlorite. Physics and Chemistry of Minerals, 15, 173–180.
- 711 Delvigne, J.E. (1998) Atlas of Micromorphology of Mineral Alteration and Weathering, 520 p.
712 Mineralogical Association of Canada.
- 713 Dowty, E. (1976) Crystal structure and crystal growth; II, Sector zoning in minerals. American
714 Mineralogist, 61, 460–469.
- 715 Dziggel, A., Wulff, K., Kolb, J., Meyer, F.M., and Lahaye, Y. (2009) Significance of oscillatory
716 and bell-shaped growth zoning in hydrothermal garnet: Evidence from the Navachab gold
717 deposit, Namibia. Chemical Geology, 262, 262–276.
- 718 Briel, J.J., and Lyman, C.E. (2006) Tutorial Review: X-ray Mapping in Electron-Beam
719 Instruments. Microscopy and Microanalysis, 12, 2–25.

- 720 Gaidies, F., Capitani, C. de, Abart, R., and Schuster, R. (2008) Prograde garnet growth along
721 complex P–T–t paths: results from numerical experiments on polyphase garnet from the Wölz
722 Complex (Austroalpine basement). *Contributions to Mineralogy and Petrology*, 155, 673–
723 688.
- 724 García-Casco, A., Torres-Roldán, R.L., Millán, G., Monié, P., and Schneider, J. (2002) Oscillatory
725 zoning in eclogitic garnet and amphibole, Northern Serpentinite Melange, Cuba: a record of
726 tectonic instability during subduction? *Journal of Metamorphic Geology*, 20, 581–598.
- 727 Gaspar, M., Knaack, C., Meinert, L.D., and Moretti, R. (2008) REE in skarn systems: A LA-ICP-
728 MS study of garnets from the Crown Jewel gold deposit. *Geochimica et Cosmochimica Acta*,
729 72, 185–205.
- 730 Grant, N.T. (1989) Deformation and fluid processes in thrust sheets from the central Pyrenees.
731 PhD. Thesis, University of Leeds.
- 732 ——— (1990) Episodic discrete and distributed deformation: consequences and controls in a
733 thrust culmination from the central Pyrenees. *Journal of Structural Geology*, 12, 835–850.
- 734 ——— (1992) Post-emplacement extension within a thrust sheet from the central Pyrenees.
735 *Journal of the Geological Society*, 149, 775–792.
- 736 Grant, N.T., Banks, D.A., McCaig, A.M., and Yardley, B.W.D. (1990) Chemistry, Source, and
737 Behavior of Fluids Involved in Alpine Thrusting of the Central Pyrenees. *Journal of*
738 *Geophysical Research*, 95, 9123–9131.
- 739 Grosch, E.G., Vidal, O., Abu-Alam, T., and McLoughlin, N. (2012) P-T Constraints on the
740 Metamorphic Evolution of the Paleoproterozoic Kromberg Type-Section, Barberton Greenstone
741 Belt, South Africa. *Journal of Petrology*, 53, 513–545.
- 742 Hayes, J.B. (1970) Polytypism of Chlorite in Sedimentary Rocks. *Clays and Clay Minerals*, 18,
743 285–306.

- 744 Millier, S., and Velde, B. (1991) Octahedral occupancy and chemical composition of diagenetic
745 (low-temperature) chlorites. *Clay Minerals*, 26, 149–168.
- 746 Holdsworth, R.E. (2004) Weak Faults--Rotten Cores. *Science*, 303, 181–182.
- 747 Holten, T., Jamtveit, B., Meakin, P., Cortini, M., Blundy, J., and Austrheim, H. (1997) Statistical
748 characteristics and origin of oscillatory zoning in crystals. *American Mineralogist*, 82, 596–
749 606.
- 750 Holten, T., Jamtveit, B., and Meakin, P. (2000) Noise and oscillatory zoning of minerals.
751 *Geochimica et Cosmochimica Acta*, 64, 1893–1904.
- 752 Houe, A., Meunier, A., Patrier-Mas, P., Rigault, C., Beaufort, D., and Vieillard, P. (2009)
753 Application of chemical geothermometry to low-temperature trioctahedral chlorites. *Clays
754 and Clay Minerals*, 57, 371–382.
- 755 Jamtveit, B. (1991) Oscillatory zonation patterns in hydrothermal grossular-andradite garnet;
756 nonlinear dynamics in regions of immiscibility. *American Mineralogist*, 76, 1319–1327.
- 757 Jamtveit, B., and Andersen, T.B. (1992) Morphological instabilities during rapid growth of
758 metamorphic garnets. *Physics and Chemistry of Minerals*, 19, 176–184.
- 759 Jamtveit, B., Wogelius, R.A., and Fraser, D.G. (1993) Zonation patterns of skarn garnets: Records
760 of hydrothermal system evolution. *Geology*, 21, 113–116.
- 761 Jolivet, M., Labaume, P., Monié, P., Brunel, M., Arnaud, N., and Campani, M. (2007)
762 Thermochemistry constraints for the propagation sequence of the south Pyrenean basement
763 thrust system (France-Spain). *Tectonics*, 26, 17 PP.
- 764 Jourdan, A.-L., Vennemann, T.W., Mullis, J., Ramseyer, K., and Spiers, C.J. (2009) Evidence of
765 growth and sector zoning in hydrothermal quartz from Alpine veins. *European Journal of
766 Mineralogy*, 21, 219–231.
- 767 Kohn, M.J. (2003) Geochemical zoning in metamorphic minerals. *The Crust*, 3, 229–261.

- 76 Kohn, M.J., and Spear, F. (2000) Retrograde net transfer reaction insurance for pressure-
769 temperature estimates. *Geology*, 28, 1127–1130.
- 77 Kwak, T.A.P. (1981) Sector-zoned annite 85 phlogopite 15 micas from the Mt. Lindsay Sn-W-F(-
771 Be) deposit, Tasmania, Australia. *The Canadian Mineralogist*, 19, 643–650.
- 78 Lacroix, B., and Vennemann, T. (2015) Empirical calibration of the oxygen isotope fractionation
773 between quartz and Fe–Mg-chlorite. *Geochimica et Cosmochimica Acta*, 149, 21–31.
- 79 Lacroix, B., Charpentier, D., Buatier, M., Vennemann, T., Labaume, P., Adatte, T., Trave, A., and
775 Dubois, M. (2012) Formation of chlorite during thrust fault reactivation. Record of fluid
776 origin and P-T conditions in the Monte Perdido thrust fault (southern Pyrenees).
777 *Contributions to Mineralogy and Petrology*, 163, 1083–1102.
- 80 Lacroix, B., Travé, A., Buatier, M., Labaume, P., Vennemann, T., and Dubois, M. (2014)
779 Syntectonic fluid-flow along thrust faults: Example of the South-Pyrenean fold-and-thrust
780 belt. *Marine and Petroleum Geology*, 49, 84–98.
- 81 Lanari, P., Guillot, S., Schwartz, S., Vidal, O., Tricart, P., Riel, N., and Beyssac, O. (2012)
782 Diachronous evolution of the alpine continental subduction wedge: Evidence from P–T
783 estimates in the Briançonnais Zone houillère (France – Western Alps). *Journal of*
784 *Geodynamics*, 56–57, 39–54.
- 85 Lanari, P., Riel, N., Guillot, S., Vidal, O., Schwartz, S., Pêcher, A., and Hattori, K.H. (2013)
786 Deciphering high-pressure metamorphism in collisional context using microprobe mapping
787 methods: Application to the Stak eclogitic massif (northwest Himalaya). *Geology*, 41, 111–
788 114.
- 89 Lanari, P., Wagner, T., and Vidal, O. (2014a) A thermodynamic model for di-trioctahedral chlorite
790 from experimental and natural data in the system MgO–FeO–Al₂O₃–SiO₂–H₂O: applications
791 to P–T sections and geothermometry. *Contributions to Mineralogy and Petrology*, 167, 1–19.

- 79 Lanari, P., Vidal, O., De Andrade, V., Dubacq, B., Lewin, E., Grosch, E.G., and Schwartz, S.
793 (2014b) XMAPTOOLS: A MATLAB©-based program for electron microprobe X-ray image
794 processing and geothermobarometry. *Computers & Geosciences*, 62, 227–240.
- 795
796
797
798
- 799
800
801
802
- 803
804
805
806
- 807
808
809
- 810
811
812
- 813
814
815
- 816
817
818
819
820
821
822
823
824
825
826
827
828
829
830
831
832
833
834
835
836
837
838
839
840
841
842
843
844
845
846
847
848
849
850
851
852
853
854
855
856
857
858
859
860
861
862
863
864
865
866
867
868
869
870
871
872
873
874
875
876
877
878
879
880
881
882
883
884
885
886
887
888
889
890
891
892
893
894
895
896
897
898
899
900
901
902
903
904
905
906
907
908
909
910
911
912
913
914
915
916
917
918
919
920
921
922
923
924
925
926
927
928
929
930
931
932
933
934
935
936
937
938
939
940
941
942
943
944
945
946
947
948
949
950
951
952
953
954
955
956
957
958
959
960
961
962
963
964
965
966
967
968
969
970
971
972
973
974
975
976
977
978
979
980
981
982
983
984
985
986
987
988
989
990
991
992
993
994
995
996
997
998
999
1000
- 1001
1002
1003
1004
1005
1006
1007
1008
1009
1010
1011
1012
1013
1014
1015
1016
1017
1018
1019
1020
1021
1022
1023
1024
1025
1026
1027
1028
1029
1030
1031
1032
1033
1034
1035
1036
1037
1038
1039
1040
1041
1042
1043
1044
1045
1046
1047
1048
1049
1050
1051
1052
1053
1054
1055
1056
1057
1058
1059
1060
1061
1062
1063
1064
1065
1066
1067
1068
1069
1070
1071
1072
1073
1074
1075
1076
1077
1078
1079
1080
1081
1082
1083
1084
1085
1086
1087
1088
1089
1090
1091
1092
1093
1094
1095
1096
1097
1098
1099
1100
- 1101
1102
1103
1104
1105
1106
1107
1108
1109
1110
1111
1112
1113
1114
1115
1116
1117
1118
1119
1120
1121
1122
1123
1124
1125
1126
1127
1128
1129
1130
1131
1132
1133
1134
1135
1136
1137
1138
1139
1140
1141
1142
1143
1144
1145
1146
1147
1148
1149
1150
1151
1152
1153
1154
1155
1156
1157
1158
1159
1160
1161
1162
1163
1164
1165
1166
1167
1168
1169
1170
1171
1172
1173
1174
1175
1176
1177
1178
1179
1180
1181
1182
1183
1184
1185
1186
1187
1188
1189
1190
1191
1192
1193
1194
1195
1196
1197
1198
1199
1200
- 1201
1202
1203
1204
1205
1206
1207
1208
1209
1210
1211
1212
1213
1214
1215
1216
1217
1218
1219
1220
1221
1222
1223
1224
1225
1226
1227
1228
1229
1230
1231
1232
1233
1234
1235
1236
1237
1238
1239
1240
1241
1242
1243
1244
1245
1246
1247
1248
1249
1250
1251
1252
1253
1254
1255
1256
1257
1258
1259
1260
1261
1262
1263
1264
1265
1266
1267
1268
1269
1270
1271
1272
1273
1274
1275
1276
1277
1278
1279
1280
1281
1282
1283
1284
1285
1286
1287
1288
1289
1290
1291
1292
1293
1294
1295
1296
1297
1298
1299
1300
- 1301
1302
1303
1304
1305
1306
1307
1308
1309
1310
1311
1312
1313
1314
1315
1316
1317
1318
1319
1320
1321
1322
1323
1324
1325
1326
1327
1328
1329
1330
1331
1332
1333
1334
1335
1336
1337
1338
1339
1340
1341
1342
1343
1344
1345
1346
1347
1348
1349
1350
1351
1352
1353
1354
1355
1356
1357
1358
1359
1360
1361
1362
1363
1364
1365
1366
1367
1368
1369
1370
1371
1372
1373
1374
1375
1376
1377
1378
1379
1380
1381
1382
1383
1384
1385
1386
1387
1388
1389
1390
1391
1392
1393
1394
1395
1396
1397
1398
1399
1400
- 1401
1402
1403
1404
1405
1406
1407
1408
1409
1410
1411
1412
1413
1414
1415
1416
1417
1418
1419
1420
1421
1422
1423
1424
1425
1426
1427
1428
1429
1430
1431
1432
1433
1434
1435
1436
1437
1438
1439
1440
1441
1442
1443
1444
1445
1446
1447
1448
1449
1450
1451
1452
1453
1454
1455
1456
1457
1458
1459
1460
1461
1462
1463
1464
1465
1466
1467
1468
1469
1470
1471
1472
1473
1474
1475
1476
1477
1478
1479
1480
1481
1482
1483
1484
1485
1486
1487
1488
1489
1490
1491
1492
1493
1494
1495
1496
1497
1498
1499
1500
- 1501
1502
1503
1504
1505
1506
1507
1508
1509
1510
1511
1512
1513
1514
1515
1516
1517
1518
1519
1520
1521
1522
1523
1524
1525
1526
1527
1528
1529
1530
1531
1532
1533
1534
1535
1536
1537
1538
1539
1540
1541
1542
1543
1544
1545
1546
1547
1548
1549
1550
1551
1552
1553
1554
1555
1556
1557
1558
1559
1560
1561
1562
1563
1564
1565
1566
1567
1568
1569
1570
1571
1572
1573
1574
1575
1576
1577
1578
1579
1580
1581
1582
1583
1584
1585
1586
1587
1588
1589
1590
1591
1592
1593
1594
1595
1596
1597
1598
1599
1600
- 1601
1602
1603
1604
1605
1606
1607
1608
1609
1610
1611
1612
1613
1614
1615
1616
1617
1618
1619
1620
1621
1622
1623
1624
1625
1626
1627
1628
1629
1630
1631
1632
1633
1634
1635
1636
1637
1638
1639
1640
1641
1642
1643
1644
1645
1646
1647
1648
1649
1650
1651
1652
1653
1654
1655
1656
1657
1658
1659
1660
1661
1662
1663
1664
1665
1666
1667
1668
1669
1670
1671
1672
1673
1674
1675
1676
1677
1678
1679
1680
1681
1682
1683
1684
1685
1686
1687
1688
1689
1690
1691
1692
1693
1694
1695
1696
1697
1698
1699
1700
- 1701
1702
1703
1704
1705
1706
1707
1708
1709
1710
1711
1712
1713
1714
1715
1716
1717
1718
1719
1720
1721
1722
1723
1724
1725
1726
1727
1728
1729
1730
1731
1732
1733
1734
1735
1736
1737
1738
1739
1740
1741
1742
1743
1744
1745
1746
1747
1748
1749
1750
1751
1752
1753
1754
1755
1756
1757
1758
1759
1760
1761
1762
1763
1764
1765
1766
1767
1768
1769
1770
1771
1772
1773
1774
1775
1776
1777
1778
1779
1780
1781
1782
1783
1784
1785
1786
1787
1788
1789
1790
1791
1792
1793
1794
1795
1796
1797
1798
1799
1800
- 1801
1802
1803
1804
1805
1806
1807
1808
1809
1810
1811
1812
1813
1814
1815
1816
1817
1818
1819
1820
1821
1822
1823
1824
1825
1826
1827
1828
1829
1830
1831
1832
1833
1834
1835
1836
1837
1838
1839
1840
1841
1842
1843
1844
1845
1846
1847
1848
1849
1850
1851
1852
1853
1854
1855
1856
1857
1858
1859
1860
1861
1862
1863
1864
1865
1866
1867
1868
1869
1870
1871
1872
1873
1874
1875
1876
1877
1878
1879
1880
1881
1882
1883
1884
1885
1886
1887
1888
1889
1890
1891
1892
1893
1894
1895
1896
1897
1898
1899
1900
- 1901
1902
1903
1904
1905
1906
1907
1908
1909
1910
1911
1912
1913
1914
1915
1916
1917
1918
1919
1920
1921
1922
1923
1924
1925
1926
1927
1928
1929
1930
1931
1932
1933
1934
1935
1936
1937
1938
1939
1940
1941
1942
1943
1944
1945
1946
1947
1948
1949
1950
1951
1952
1953
1954
1955
1956
1957
1958
1959
1960
1961
1962
1963
1964
1965
1966
1967
1968
1969
1970
1971
1972
1973
1974
1975
1976
1977
1978
1979
1980
1981
1982
1983
1984
1985
1986
1987
1988
1989
1990
1991
1992
1993
1994
1995
1996
1997
1998
1999
2000
- 2001
2002
2003
2004
2005
2006
2007
2008
2009
2010
2011
2012
2013
2014
2015
2016
2017
2018
2019
2020
2021
2022
2023
2024
2025
2026
2027
2028
2029
2030
2031
2032
2033
2034
2035
2036
2037
2038
2039
2040
2041
2042
2043
2044
2045
2046
2047
2048
2049
2050
2051
2052
2053
2054
2055
2056
2057
2058
2059
2060
2061
2062
2063
2064
2065
2066
2067
2068
2069
2070
2071
2072
2073
2074
2075
2076
2077
2078
2079
2080
2081
2082
2083
2084
2085
2086
2087
2088
2089
2090
2091
2092
2093
2094
2095
2096
2097
2098
2099
2100
- 2101
2102
2103
2104
2105
2106
2107
2108
2109
2110
2111
2112
2113
2114
2115
2116
2117
2118
2119
2120
2121
2122
2123
2124
2125
2126
2127
2128
2129
2130
2131
2132
2133
2134
2135
2136
2137
2138
2139
2140
2141
2142
2143
2144
2145
2146
2147
2148
2149
2150
2151
2152
2153
2154
2155
2156
2157
2158
2159
2160
2161
2162
2163
2164
2165
2166
2167
2168
2169
2170
2171
2172
2173
2174
2175
2176
2177
2178
2179
2180
2181
2182
2183
2184
2185
2186
2187
2188
2189
2190
2191
2192
2193
2194
2195
2196
2197
2198
2199
2200
- 2201
2202
2203
2204
2205
2206
2207
2208
2209
2210
2211
2212
2213
2214
2215
2216
2217
2218
2219
2220
2221
2222
2223
2224
2225
2226
2227
2228
2229
2230
2231
2232
2233
2234
2235
2236
2237
2238
2239
2240
2241
2242
2243
2244
2245
2246
2247
2248
2249
2250
2251
2252
2253
2254
2255
2256
2257
2258
2259
2260
2261
2262
2263
2264
2265
2266
2267
2268
2269
2270
2271
2272
2273
2274
2275
2276
2277
2278
2279
2280
2281
2282
2283
2284
2285
2286
2287
2288
2289
2290
2291
2292
2293
2294
2295
2296
2297
2298
2299
2300
- 2301
2302
2303
2304
2305
2306
2307
2308
2309
2310
2311
2312
2313
2314
2315
2316
2317
2318
2319
2320
2321
2322
2323
2324
2325
2326
2327
2328
2329
2330
2331
2332
2333
2334
2335
2336
2337
2338
2339
2340
2341
2342
2343
2344
2345
2346
2347
2348
2349
2350
2351
2352
2353
2354
2355
2356
2357
2358
2359
2360
2361
2362
2363
2364
2365
2366
2367
2368
2369
2370
2371
2372
2373
2374
2375
2376
2377
2378
2379
2380
2381
2382
2383
2384
2385
2386
2387
2388
2389
2390
2391
2392
2393
2394
2395
2396
2397
2398
2399
2400
- 2401
2402
2403
2404
2405
2406
2407
2408
2409
2410
2411
2412
2413
2414
2415
2416
2417
2418
2419
2420
2421
2422
2423
2424
2425
2426
2427
2428
2429
2430
2431
2432
2433
2434
2435
2436
2437
2438
2439
2440
2441
2442
2443
2444
2445
2446
2447
2448
2449
2450
2451
2452
2453
2454
2455
2456
2457
2458
2459
2460
2461
2462
2463
2464
2465
2466
2467
2468
2469
2470
2471
2472
2473
2474
2475
2476
2477
2478
2479
2480
2481
2482
2483
2484
2485
2486
2487
2488
2489
2490
2491
2492
2493
2494
2495
2496
2497
2498
2499
2500
- 2501
2502
2503
2504
2505
2506
2507
2508
2509
2510
2511
2512
2513
2514
2515
2516
2517
2518
2519
2520
2521
2522
2523
2524
2525
2526
2527
2528
2529
2530
2531
2532
2533
2534
2535
2536
2537
2538
2539
2540
2541
2542
2543
2544
2545
2546
2547
2548
2549
2550
2551
2552
2553
2554
2555
2556
2557
2558
2559
2560
2561
2562
2563
2564
2565
2566
2567
2568
2569
2570
2571
2572
2573
2574
2575
2576
2577
2578
2579
2580
2581
2582
2583
2584
2585
2586
2587
2588
2589
2590
2591
2592
2593
2594
2595
2596
2597
2598
2599
2600
- 2601
2602
2603
2604
2605
2606
2607
2608
2609
2610
2611
2612
2613
2614
2615
2616
2617
2618
2619
2620
2621
2622
2623
2624
2625
2626
2627
2628
2629
2630
2631
2632
2633
2634
2635
2636
2637
2638
2639
2640
2641
2642
2643
2644
2645
2646
2647
2648
2649
2650
2651
2652
2653
2654
2655
2656
2657
2658
2659
2660
2661
2662
2663
2664
2665
2666
2667
2668
2669
2670
2671
2672
2673
2674
2675
2676
2677
2678
2679
2680
2681
2682
2683
2684
2685
2686
2687
2688
2689
2690
2691
2692
2693
2694
2695
2696
2697
2698
2699
2700
- 2701
2702
2703
2704
2705
2706
2707
2708
2709
2710
2711
2712
2713
2714
2715
2716
2717
2718
2719
2720
2721
2722
2723
2724
2725
2726
2727
2728
2729
2730
2731
2732
2733
2734
2735
2736
2737
2738
2739
2740
2741
2742
2743
2744
2745
2746
2747
2748
2749
2750
2751
2752
2753
2754
2755
2756
2757
2758
2759
2760
2761
2762
2763
2764
2765
2766
2767
2768
2769
2770
2771
2772
2773
2774
2775
2776
2777
2778
2779
2780
2781
2782
2783
2784
2785
2786
2787
2788
2789
2790
2791
2792
2793
2794
2795
2796
2797
2798
2799
2800
- 2801
2802
2803
2804
2805
2806
2807
2808
2809
2810
2811
2812
2813
2814
2815
2816
2817
2818
2819
2820
2821
2822
2823
2824
2825
28

- 81 Merlet, C., and Bodinier, J.-L. (1990) Electron microprobe determination of minor and trace
817 transition elements in silicate minerals: A method and its application to mineral zoning in the
818 peridotite nodule PHN 1611. *Chemical Geology*, 83, 55–69.
- 81 Meth, C.E., and Carlson, W.D. (2005) Diffusion-Controlled Synkinematic Growth of Garnet from
820 a Heterogeneous Precursor at Passo Del Sole, Switzerland. *The Canadian Mineralogist*, 43,
821 157–182.
- 82 Mogi, K., Mochizuki, H., and Kurokawa, Y. (1989) Temperature changes in an artesian spring at
823 Usami in the Izu Peninsula (Japan) and their relation to earthquakes. *Tectonophysics*, 159,
824 95–108.
- 82 Muñoz, J.A. (1992) Evolution of a continental collision belt: ECORS-Pyrenees crustal balanced
826 cross-section. In K.R. McClay, Ed., *Thrust Tectonics* pp. 235–246. Springer Netherlands,
827 Dordrecht.
- 82 Muñoz, M., De Andrade, V., Vidal, O., Lewin, E., Pascarelli, S., and Susini, J. (2006) Redox and
829 speciation micromapping using dispersive X-ray absorption spectroscopy: Application to iron
830 chlorite mineral of a metamorphic rock thin section. *Geochemistry Geophysics Geosystems*,
831 7, Q11020.
- 83 Muñoz, M., Pascarelli, S., Aquilanti, G., Narygina, O., Kurnosov, A., and Dubrovinsky, L. (2008)
833 Hyperspectral μ -XANES mapping in the diamond-anvil cell: analytical procedure applied to
834 the decomposition of (Mg,Fe)-ringwoodite at the upper/lower mantle boundary. *High
835 Pressure Research*, 28, 665–673.
- 83 Muñoz, M., Vidal, O., Marcaillou, C., Pascarelli, S., Mathon, O., and Farges, F. (2013) Iron
837 oxidation state in phyllosilicate single crystals using Fe-K pre-edge and XANES
838 spectroscopy: Effects of the linear polarization of the synchrotron X-ray beam. *American
839 Mineralogist*, 98, 1187–1197.

- 840 Nicotra, E., and Viccaro, M. (2012) Unusual magma storage conditions at Mt. Etna (Southern
841 Italy) as evidenced by plagioclase megacryst-bearing lavas: implications for the plumbing
842 system geometry and summit caldera collapse. *Bulletin of Volcanology*, 74, 795–815.
- 843 Bearce, M.A., and Wheeler, J. (2010) Modelling grain-recycling zoning during metamorphism.
844 *Journal of Metamorphic Geology*, 28, 423–437.
- 845 Butirka, K.D., and Tepley, F.J. (2008) Minerals, inclusions and volcanic processes. Mineralogical
846 Society of America, Chantilly, VA.
- 847 Rahl, J.M., Haines, S.H., and van der Pluijm, B.A. (2011) Links between orogenic wedge
848 deformation and erosional exhumation: Evidence from illite age analysis of fault rock and
849 detrital thermochronology of syn-tectonic conglomerates in the Spanish Pyrenees. *Earth and
850 Planetary Science Letters*, 307, 180–190.
- 851 Ramsay, J.G. (1980) The crack–seal mechanism of rock deformation. *Nature*, 284, 135–139.
- 852 Robyr, M., Carlson, W.D., Passchier, C., and Vonlanthen, P. (2009) Microstructural, chemical and
853 textural records during growth of snowball garnet. *Journal of Metamorphic Geology*, 27, 423–
854 437.
- 855 Robyr, M., Darbellay, B., and Baumgartner, L. p. (2014) Matrix-dependent garnet growth in
856 polymetamorphic rocks of the Sesia zone, Italian Alps. *Journal of Metamorphic Geology*, 32,
857 3–24.
- 858 Roure, F., Choukroune, P., Berastegui, X., Munoz, J.A., Villien, A., Matheron, P., Bareyt, M.,
859 Seguret, M., Camara, P., and Deramond, J. (1989) Ecore deep seismic data and balanced cross
860 sections: Geometric constraints on the evolution of the Pyrenees. *Tectonics*, 8, 41–50.
- 861 Schumacher, R., Roetzler, K., and Maresch, W.V. (1999) Subtle oscillatory zoning in garnet from
862 regional metamorphic phyllites and mica schists, western Erzgebirge, Germany. *The
863 Canadian Mineralogist*, 37, 381–403.

- 863 Shata, S., and Hesse, R. (1998) A refined XRD method for the determination of chlorite
865 composition and application to the McGerrigle Mountains anchizone in the Quebec
866 Appalachians. *The Canadian Mineralogist*, 36, 1525–1546.
- 867 Shcherbakov, V.D., Plechov, P.Y., Izbekov, P.E., and Shipman, J.S. (2011) Plagioclase zoning as
868 an indicator of magma processes at Bezymianny Volcano, Kamchatka. *Contributions to*
869 *Mineralogy and Petrology*, 162, 83–99.
- 870 Shore, M., and Fowler, A.D. (1996) Oscillatory zoning in minerals; a common phenomenon. *The*
871 *Canadian Mineralogist*, 34, 1111–1126.
- 872 Sibson, R.H. (1990) Conditions for fault-valve behaviour. Geological Society, London, Special
873 Publications, 54, 15–28.
- 874 Souche, A., Medvedev, S., Andersen, T.B., and Dabrowski, M. (2013) Shear heating in extensional
875 detachments: Implications for the thermal history of the Devonian basins of W Norway.
876 *Tectonophysics*, 608, 1073–1085.
- 877 Tarantola, A., Mullis, J., Guillaume, D., Dubessy, J., de Capitani, C., and Abdelmoula, M. (2009)
878 Oxidation of CH₄ to CO₂ and H₂O by chloritization of detrital biotite at 270 +/- 5 degrees C
879 in the external part of the Central Alps, Switzerland. *Lithos*, 112, 497–510.
- 880 Teixell, A. (1996) The Anso transect of the southern Pyrenees: basement and cover thrust
881 geometries. *Journal of the Geological Society*, 153, 301–310.
- 882 ——— (1998) Crustal structure and orogenic material budget in the west central Pyrenees.
883 *Tectonics*, 17, PP. 395–406.
- 884 Toutain, J.P., Munoz, M., Poitrasson, F., and Lienard, A.C. (1997) Springwater chloride ion
885 anomaly prior to a ML= 5.2 Pyrenean earthquake. *Earth and planetary science letters*, 149,
886 113–119.

- 88Toutain, J.-P., Munoz, M., Pinaud, J.-L., Levet, S., Sylvander, M., Rigo, A., and Escalier, J. (2006)
888 Modelling the mixing function to constrain coseismic hydrochemical effects: An example
889 from the French Pyrénées. *pure and applied geophysics*, 163, 723–744.
- 89Trincal, V., Lacroix, B., Buatier, M.D., Charpentier, D., Labaume, P., and Lahfid, A. (2014a) Low
891 grade metamorphism fluid circulation in a sedimentary environment thrust fault zone:
892 properties and modeling Vol. 16, p. 12078. Presented at the EGU General Assembly
893 Conference Abstracts.
- 89Trincal, V., Charpentier, D., Buatier, M.D., Grobety, B., Lacroix, B., Labaume, P., and Sizun, J.-P.
895 (2014b) Quantification of mass transfers and mineralogical transformations in a thrust fault
896 (Monte Perdido thrust unit, southern Pyrenees, Spain). *Marine and Petroleum Geology*, 55,
897 160–175.
- 89Vidal, O., Parra, T., and Trotet, F. (2001) A thermodynamic model for Fe-Mg aluminous chlorite
899 using data from phase equilibrium experiments and natural pelitic assemblages in the 100
900 degrees to 600 degrees C, 1 to 25 kb range. *American Journal of Science*, 301, 557–592.
- 90Vidal, O., Parra, T., and Vieillard, P. (2005) Thermodynamic properties of the Tschermak solid
902 solution in Fe-chlorite: Application to natural examples and possible role of oxidation.
903 *American Mineralogist*, 90, 347–358.
- 90Vidal, O., De Andrade, V., Lewin, E., Muñoz, M., Parra, T., and Pascarelli, S. (2006) P-T-
905 deformation-Fe³⁺/Fe²⁺ mapping at the thin section scale and comparison with XANES
906 mapping: application to a garnet-bearing metapelite from the Sambagawa metamorphic belt
907 (Japan). *Journal of Metamorphic Geology*, 24, 669–683.
- 90Walker, J.R. (1993) Chlorite polytype geothermometry. *Clays and Clay Minerals*, 41, 260–260.
- 90Wang, C., and Manga, M. (2010) *Earthquakes and water* Vol. 114. Springer Science & Business
910 Media.

91 Wilke, M., Farges, F., Petit, P.-E., Brown, G.E., and Martin, F. (2001) Oxidation state and
912 coordination of Fe in minerals: An Fe K-XANES spectroscopic study. American
913 Mineralogist, 86, 714–730.

914 Wintsch, R.P., Christoffersen, R., and Kronenberg, A.K. (1995) Fluid-rock reaction weakening of
915 fault zones. Journal of Geophysical Research, 100, 13021–13,032.

916 Yardley, B.W.D., Rochelle, C.A., Barnicoat, A.C., and Lloyd, G.E. (1991) Oscillatory zoning in
917 metamorphic minerals: an indicator of infiltration metasomatism. Mineralogical Magazine,
918 55, 357–365.

919 Zane, A., Sassi, R., and Guidotti, C.V. (1998) New data on metamorphic chlorite as a petrogenetic
920 indicator mineral, with special regard to greenschist-facies rocks. The Canadian Mineralogist,
921 36, 713–726.

922 Zhai, D.-G., Liu, J.-J., Zhang, H.-Y., Wang, J.-P., Su, L., Yang, X.-A., and Wu, S.-H. (2014)
923 Origin of oscillatory zoned garnets from the Xieertala Fe–Zn skarn deposit, northern China:
924 In situ LA–ICP–MS evidence. Lithos, 190–191, 279–291.

925

926

Figure captions

927 **Figure 1.** (a) Structural map of the Pyrenees with the location of study area (modified from
928 Teixell 2000). Geological map (b) and (c) cross section AB of the Gavarnie thrust sheet
929 showing the location of the study area (Pic de Port Vieux) modified from Grant (1992) and
930 Jolivet et al. (2007). MPT: Monte Perdido thrust; PT: Pineta thrust.

931

932 **Figure 2.** (a) View of the Pic de Port Vieux massif. (b) Pic de Port Vieux thrust culmination
933 showing the main study area, modified from Grant (1989). (c) Schematic stratigraphic log
934 through the Pic de Port Vieux culmination, modified from Grant (1990). GT: Gavarnie
935 Thrust; PPVT: Pic de Port Vieux Thrust.

936

937 **Figure 3.** (a) Pic de Port Vieux outcrop showing hanging-wall Triassic pelites and footwall
938 Cretaceous dolomitic limestone separated by the PPV thrust. (b) Outcrop view of shear and
939 extension veins filled by quartz and chlorite in hanging wall Triassic pelite. (c) Detailed
940 sketch of synthetic faults (faults A and B); others faults and veins are indicated in grey
941 (modified from Grant 1989). Stars: samples with oscillatory zoned chlorite, from Grant
942 (1989) (NF) and from this study (PPV). Red and green colors correspond to red pelite and
943 altered green pelite, respectively.

944

945 **Figure 4.** (a) Schematic diagram of the structural organization of the studied fault zone
946 outcrop. (b) SEM image of pelite showing quartz, muscovite, chlorite, hematite, rutile and
947 apatite minerals; PPV12-06B sample. (c) SEM image of green pelite with almost the same
948 mineralogy as B except for hematite; PPV12-05 sample. (d) Optical microscopic image from
949 dolomitic limestone showing euhedral dolomite in micritic calcite matrix; PPV11-01 sample.
950 (e) SEM image of euhedral dolomite and iron oxides in micritic calcite. (f) Zoom from (e) on
951 a dolomite crystal partially dissolved in calcite matrix. Newly formed calcite precipitated
952 inside dolomitic cracks and dissolution ghosts (in black). (g) SEM image of a fractured and
953 microveined dolomitic limestone sampled closed to thrust in the footwall.

954

955 **Figure 5.** Microscopic observation of thin sections from the studied fault zone. (a-b) quartz +
956 chlorite \pm calcite extension crack-seal syntaxial vein showing chlorite nucleation in contact
957 with host-pelite preferentially to silt; in PPL and XPL respectively from sample PPV11-11B.
958 (c-d) shear vein showing blocky quartz \pm calcite crystal textures and rosette shaped zoned
959 chlorite; in PPL and XPL respectively from sample PPV11-25B. (e) Representative sketch of

960 veins cogenetic to synthetic fault. In extension veins, quartz crack-seal appears parallel to the
961 vein wall. Key: S: schistosity plane; PPL: plane polarized light; XPL: cross polarized light.

962

963 **Figure 6.** (a) vSEM images of oscillatory zoning pattern chlorite crystals from sample PPV11-
964 XX. The rosette like morphology of the chlorite aggregates is imaged (b) in 3D on PPV11-16
965 sample and (c) in thin section on sample PPV11-19. (d) Contrasted layers can have different
966 thickness from one rosette to another and zonation can be complex as imaged in sample
967 PPV11-25B. (e) At a higher magnification, the contrast distribution seems to follow the
968 growth development of the chlorite crystals but with preferential growth directions as
969 highlighted in sample PPV11-25B.

970

971 **Figure 7.** Microprobe X-Ray (WDS) images from sample PPV11-XX. Values of each box are
972 reported table 1. (a) SEM-BSE image of the analyzed area (b) Zone 1 to 5 defined from (a)
973 based on electronic contrast. (c) FeO in wt%. (d) MgO in wt%. (e) SiO₂ in wt%. (f) Al₂O₃ in
974 wt%.

975

976 **Figure 8.** (a) Scheme of the mapped area showing growth bands in clinocllore concentric
977 crystal (sample PPV11-XX MapA), and the locations of μ -XANES measurements; (b)
978 corresponding normalized XANES spectra; (c) baseline-subtracted pre-edge peaks (white
979 circles), best fits (solid lines) and peaks used for deconvolution (dashed lines); (d) integrated
980 area versus centroid position variogram showing the positions of standards together with the
981 data from clinocllore crystal. Values are reported Table 1 and converted in XFe³⁺ based on
982 the calibration curve of Wilke et al. (2001).

983

984 **Figure 9.** Plot of the chlorite compositions from boxes samples in (a) chemical elements of
985 the octahedron; (b) Amesite-(clinochlore + daphnite)-sudaite end-member ternary diagram
986 including iron state oxidation data. FM = Fe-Mg substitution; TK = Tschermak substitution;
987 DT = Ditriooctahedral substitution.

988

989 **Figure 10.** Microprobe X-Ray images from sample PPV11-XX with $\text{Fe}^{3+}/\text{Fe}_{\text{Tot}}$ specific for
990 each chlorite band. Representative values of each zone are reported table 1. (a) Fe^{2+} in a.p.f.u..
991 (b) Fe^{3+} in a.p.f.u.. (c) $X_{\text{MG}} = \text{Mg}^{2+}/(\text{Mg}^{2+}+\text{Fe}^{2+})$ ratio. (d) Temperature map from Lanari et al.
992 (2014a) model calculation.

993

994 **Figure 11.** Relationships between the $(\text{Fe}^{3+}/\sum\text{Fe})_{\text{chl}}$ value in chlorite and the temperatures
995 estimate from the Lanari et al. (2014a) geo-thermometer. Two main trends were reported from
996 Lanari et al. (2014a) corresponding on two redox conditions of fluid, which are less oxidized
997 (continuous line) and more oxidized (dashed line). Each sample number refers to its zone in
998 MapA (in blue) or in MapB (in red); for example the red star corresponds to the zone 5 in
999 MapB.

1000

1001

1002

1003

Tables

Spot	Integrated area	Centroid energy (eV)	X Fe^{3+}
Xan1	0.1021	7113.55 ± 0.05	42 (7)
Xan2	0.0969	7113.33 ± 0.05	27 (5)
Xan3	0.1029	7113.45 ± 0.05	34 (5)
Xan4	0.0940	7113.27 ± 0.05	23 (5)

Xan5	0.1281	7113.59 ± 0.05	44 (5)
------	--------	----------------	--------

1004 **Table 1.** Results from XANES and pre-edge spot analyses, showing the integrated area and
 1005 centroid position of pre-edge peaks and XFe³⁺ values obtained from XANES normalization.

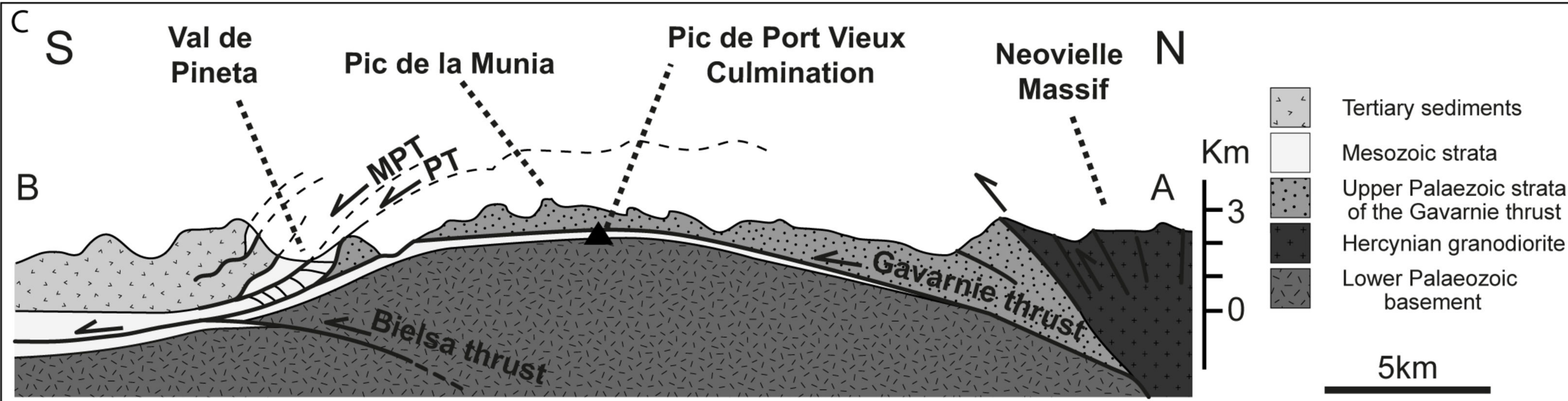
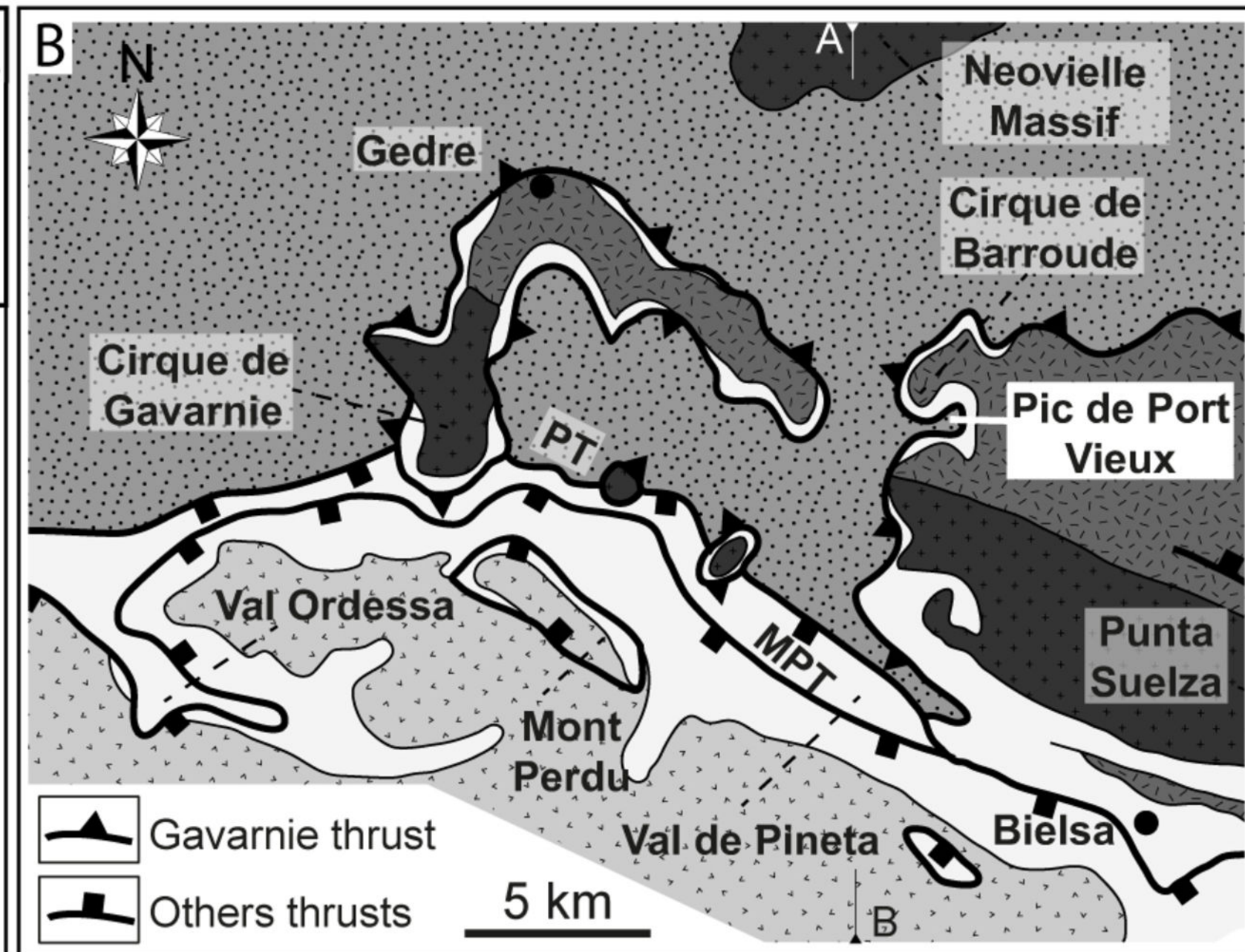
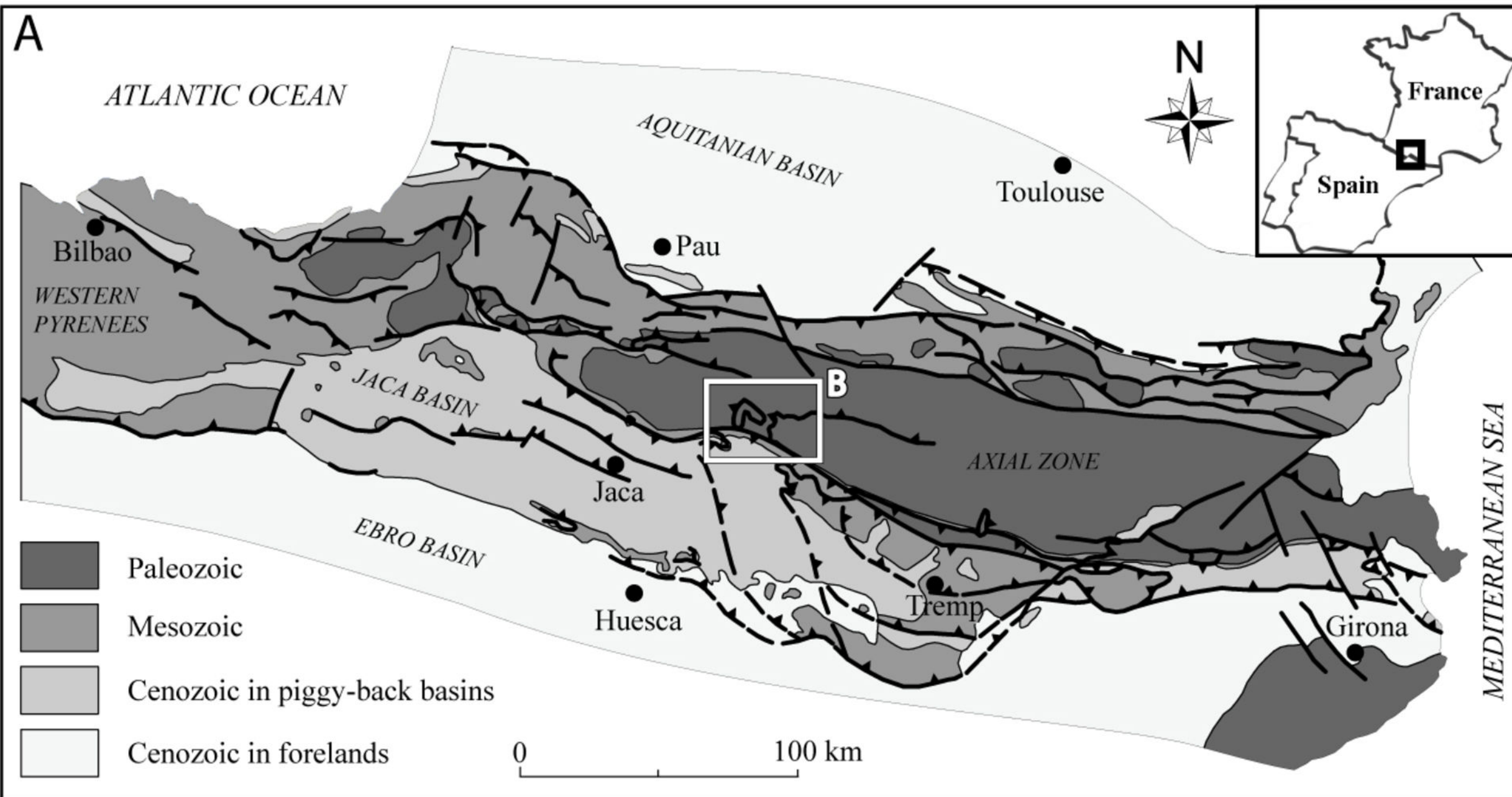
1006

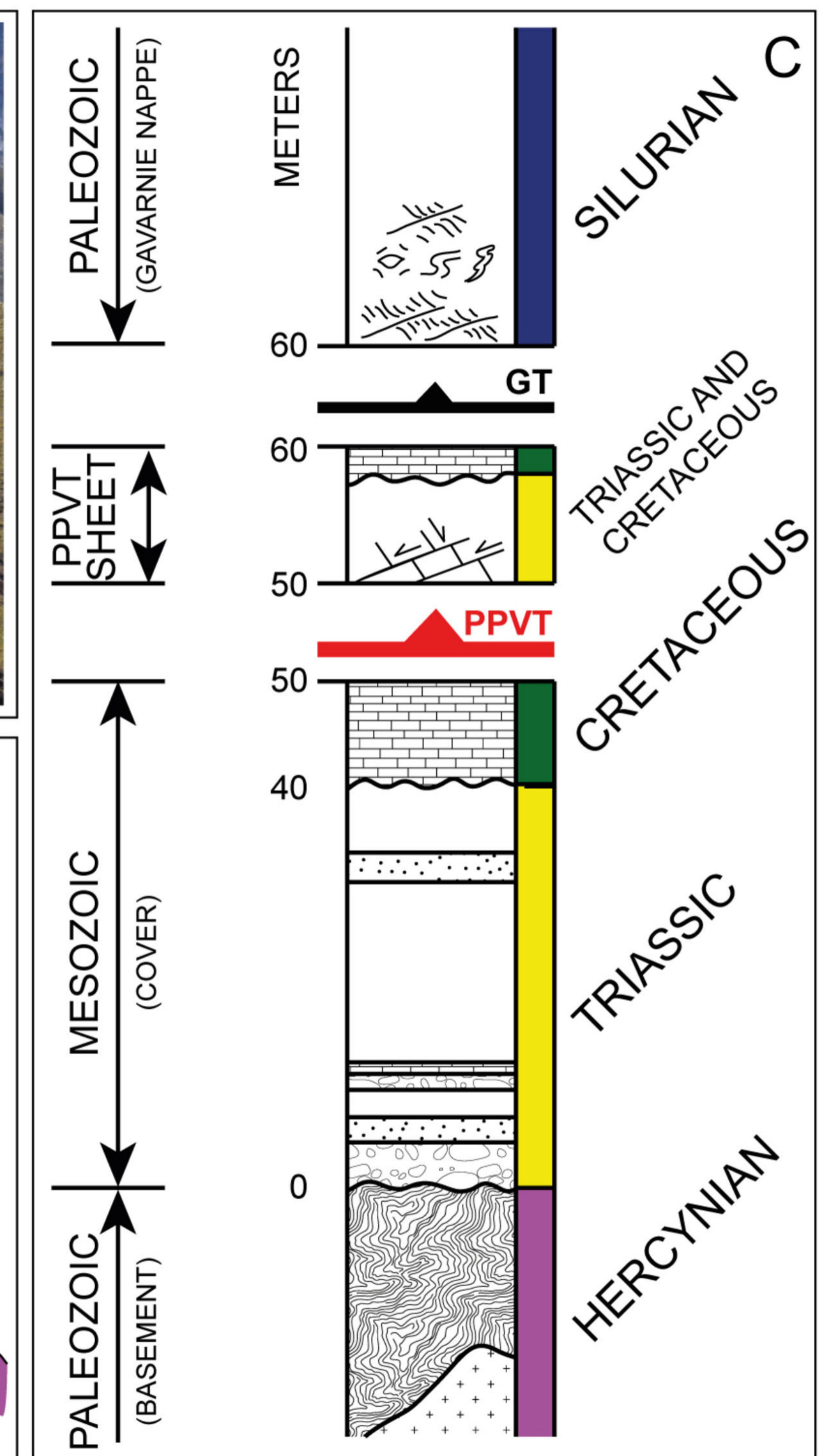
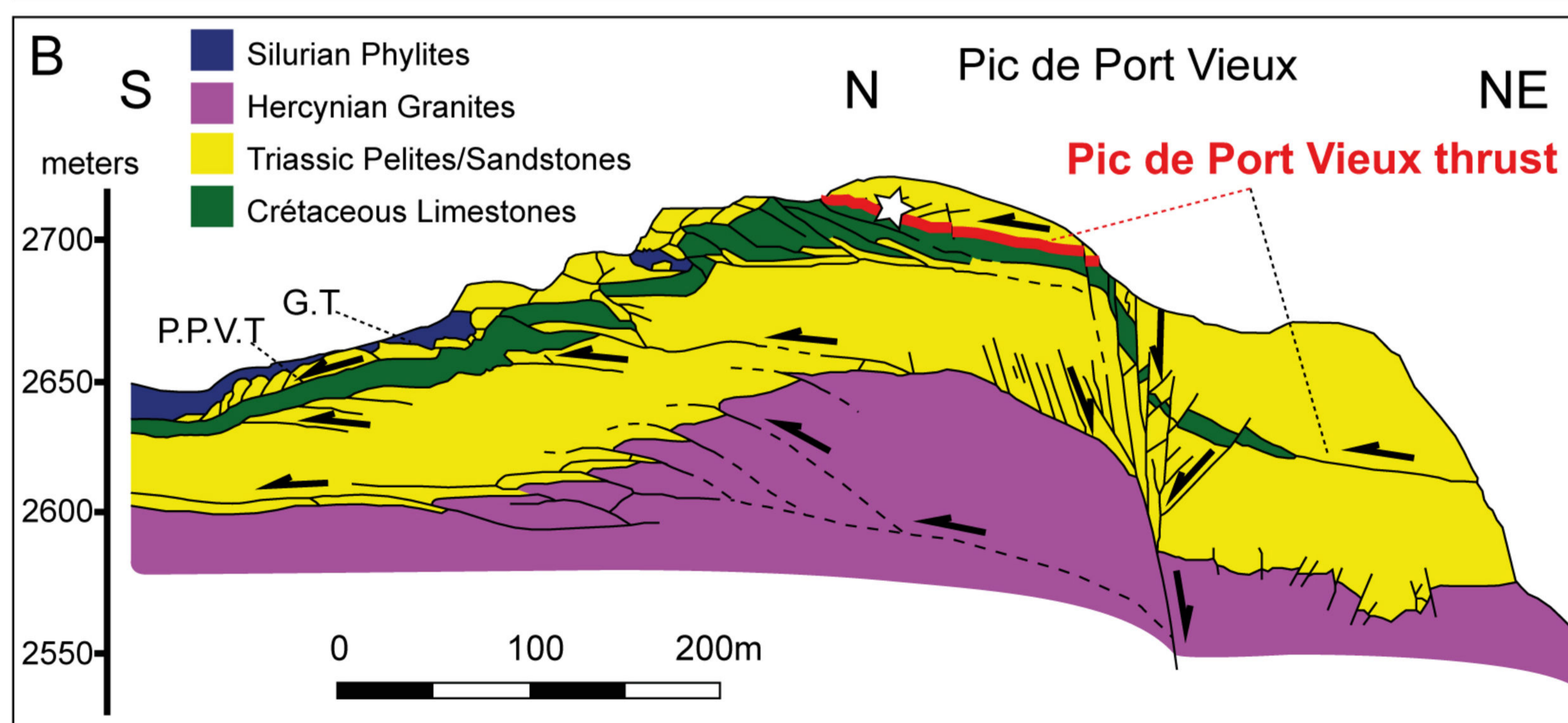
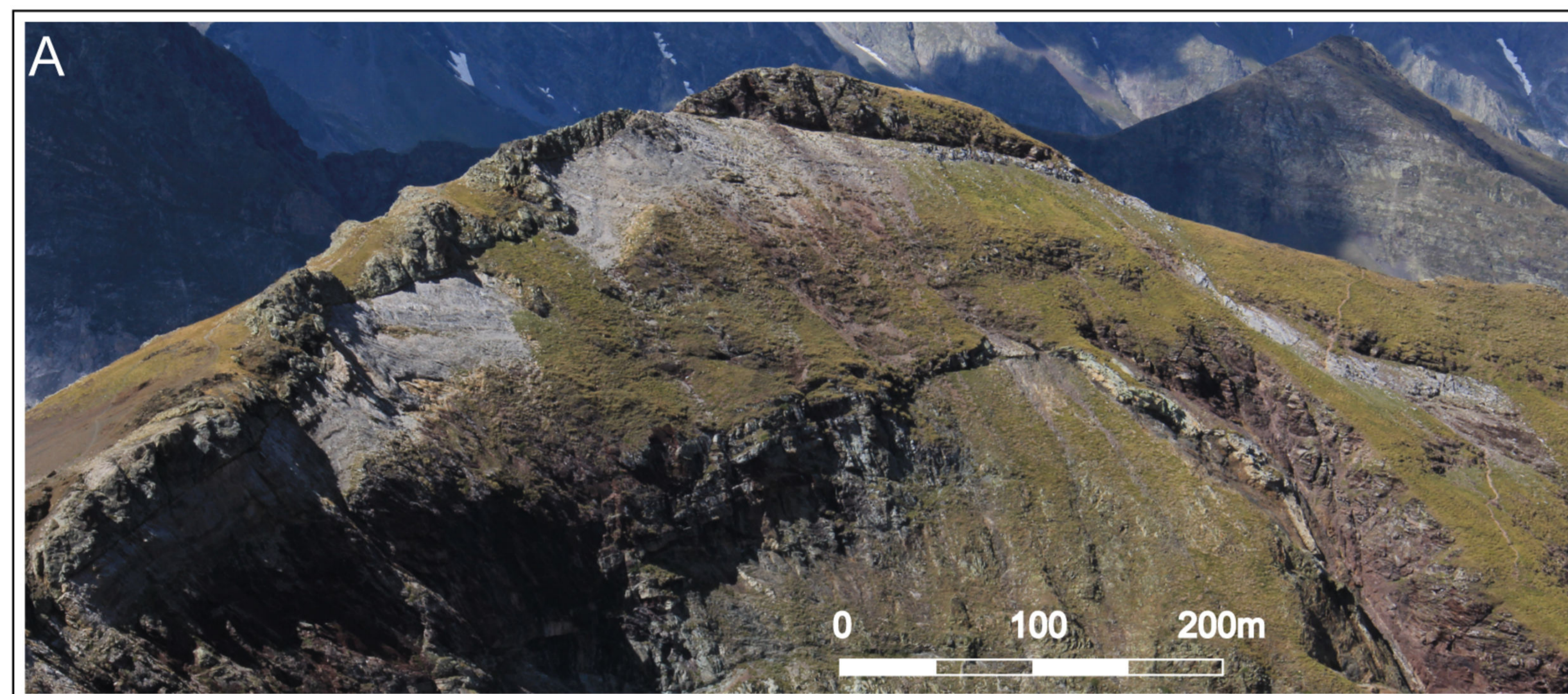
Zones	MapA					MapB					Unzoned
	1A	2A	3A	4A	5A	1B	2B	3B	4B	5B	
SiO ₂	25.1 7 (49)	26.1 1 (36)	25.7 4 (33)	25.98 (43)	25.53 (44)	25.76 (33)	26.39 (37)	25.75 (34)	25.85 (39)	25.55 (33)	26.57 (71)
TiO ₂	0.01 (0)	0.01 (0)	0.01 (0)	0.01 (0)	0.01 (0)	0.02 (0)	0.01 (0)	0.02 (0)	0.01 (1)	0.02 (0)	0.03 (8)
Al ₂ O ₃	22.7 6 (52)	22.9 3 (29)	23.2 5 (32)	23.65 (56)	23.16 (46)	22.91 (42)	23.00 (41)	23.17 (39)	23.55 (43)	23.05 (41)	22.91 (66)
FeO	20.9 8 (88)	18.4 3 (76)	20.4 3 (62)	18.39 (91)	21.94 (81)	21.92 (42)	17.59 (48)	20.47 (45)	18.70 (77)	21.48 (42)	24.27 (176)
MgO	17.2 7 (76)	19.6 4 (63)	17.8 6 (54)	19.09 (75)	16.41 (65)	16.36 (43)	19.83 (54)	17.44 (45)	18.83 (70)	16.58 (42)	14.54 (136)
MnO	0.09 (3)	0.09 (3)	0.09 (3)	0.09 (3)	0.08 (3)	0.10 (2)	0.11 (2)	0.11 (2)	0.11 (2)	0.11 (2)	0.05 (5)
CaO	0.02 (1)	0.01 (0)	0.01 (0)	0.01 (0)	0.01 (0)	0.01 (0)	0.01 (0)	0.01 (0)	0.01 (0)	0.01 (0)	0.03 (4)
Na ₂ O	0.02 (0)	0.02 (0)	0.02 (0)	0.02 (0)	0.02 (0)	0.03 (1)	0.03 (1)	0.03 (1)	0.03 (1)	0.03 (1)	0.00 (2)
Cr ₂ O ₃	0.05 (2)	0.05 (2)	0.05 (2)	0.05 (2)	0.04 (2)	0.05 (1)	0.05 (1)	0.05 (1)	0.05 (1)	0.05 (1)	
K ₂ O	0.01 (0)	0.01 (0)	0.01 (0)	0.01 (0)	0.01 (0)	0.01 (0)	0.01 (0)	0.01 (0)	0.01 (0)	0.01 (0)	0.03 (14)
Σ	86.3 7 (116)	87.2 9 (54)	87.4 7 (53)	87.30 (131)	87.23 (96)	87.17 (76)	87.02 (74)	87.04 (73)	87.15 (72)	86.87 (70)	88.20 (112)
Si	2.58 (3)	2.63 (2)	2.60 (3)	2.62 (3)	2.59 (3)	2.62 (3)	2.65 (3)	2.62 (3)	2.61 (3)	2.60 (3)	
Al ^{IV}	1.42 (3)	1.37 (2)	1.40 (3)	1.38 (4)	1.41 (3)	1.38 (3)	1.35 (3)	1.38 (3)	1.39 (3)	1.40 (3)	
Al ^{VI}	1.33 (4)	1.35 (3)	1.37 (3)	1.42 (5)	1.37 (4)	1.37 (3)	1.38 (4)	1.39 (3)	1.42 (4)	1.37 (3)	
Fe ²⁺	1.04 (5)	1.13 (5)	1.14 (4)	1.19 (6)	1.04 (4)	1.08 (2)	1.08 (3)	1.15 (3)	1.22 (5)	1.02 (2)	
Fe ³⁺	0.68 (3)	0.38 (2)	0.53 (2)	0.32 (2)	0.74 (3)	0.70 (1)	0.36 (1)	0.53 (1)	0.33 (1)	0.72 (2)	
Mg	2.64 (10)	2.95 (8)	2.69 (8)	2.87 (10)	2.48 (10)	2.48 (6)	2.97 (7)	2.64 (6)	2.84 (9)	2.52 (6)	
Fe ³⁺ /Fe _{Tot}	0.42	0.27	0.34	0.23	0.44	0.42	0.27	0.34	0.23	0.44	

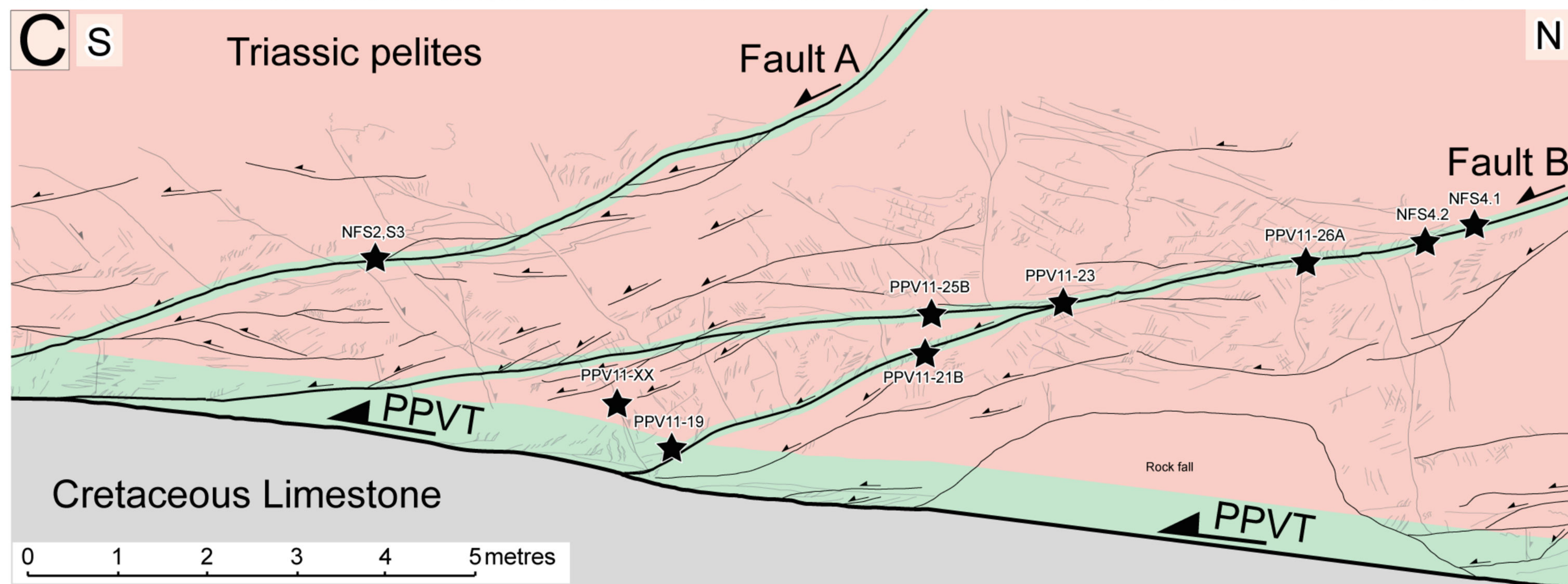
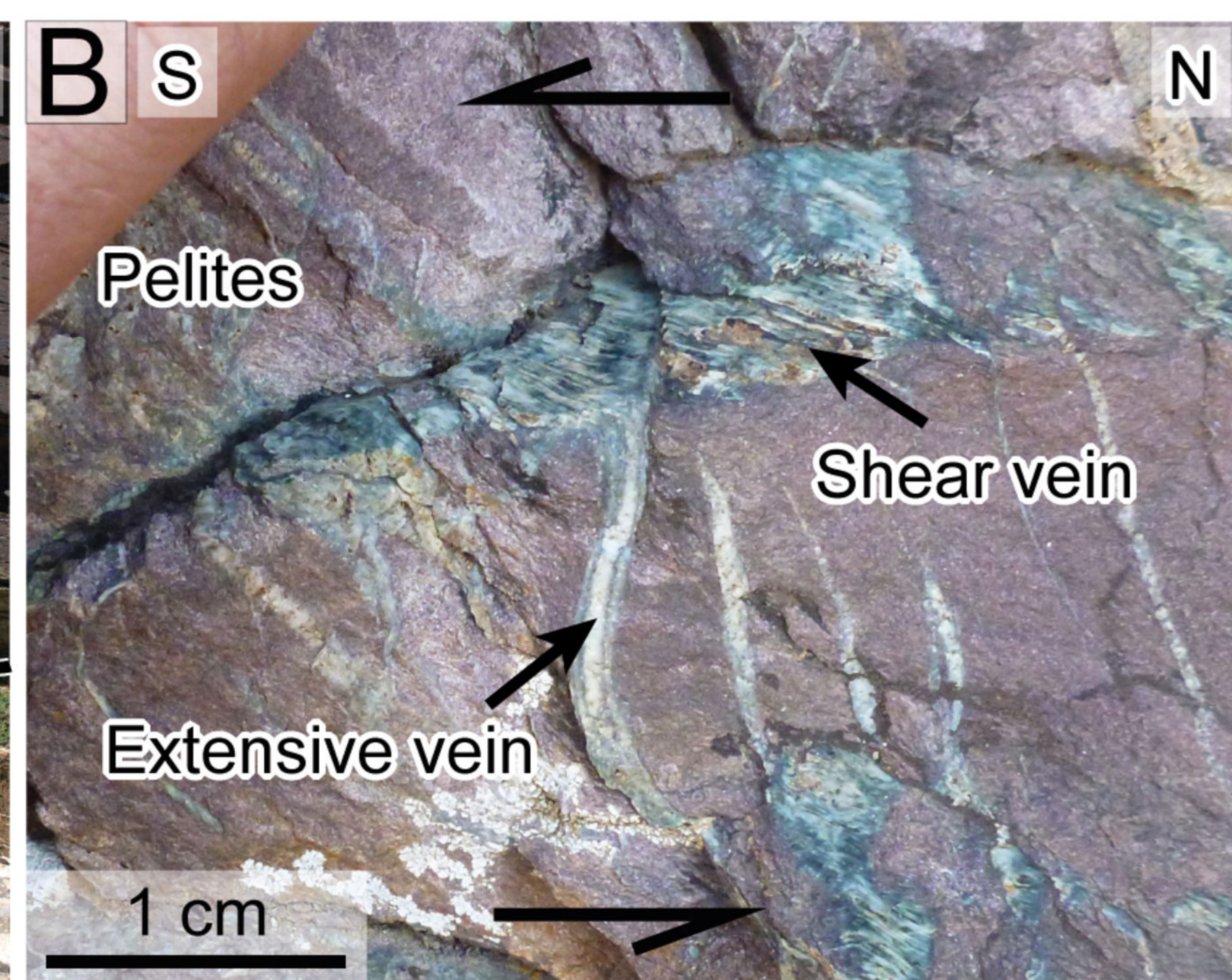
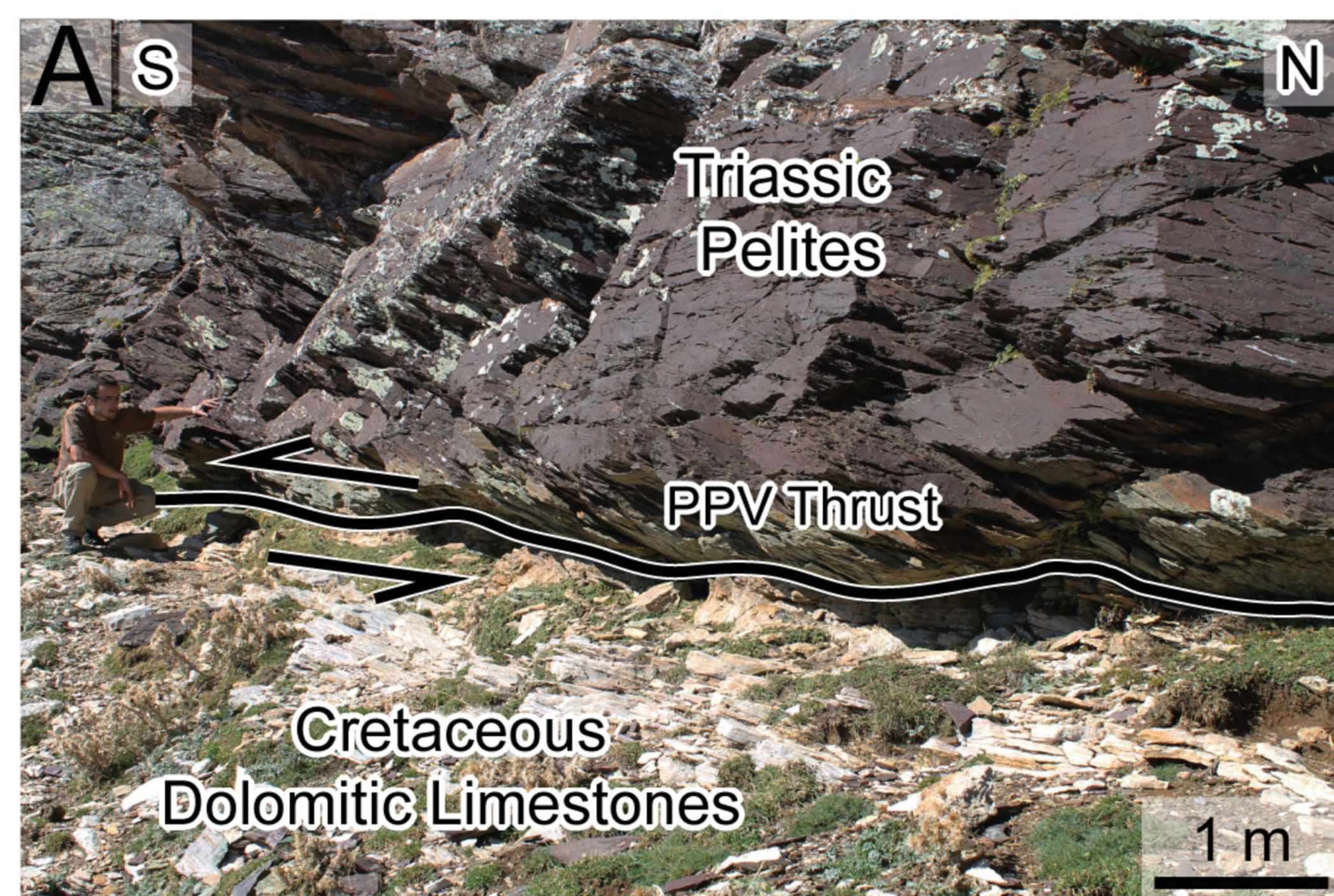
Al M1 = Xame	0.43 (3)	0.38 (2)	0.40 (3)	0.39 (3)	0.41 (3)	0.39 (3)	0.35 (3)	0.39 (3)	0.39 (3)	0.40 (3)	
Mg M1 = Xclin	0.20 (2)	0.32 (2)	0.24 (2)	0.31 (2)	0.17 (2)	0.19 (1)	0.33 (2)	0.24 (2)	0.30 (2)	0.18 (1)	
Fe M1 = Xdap	0.08 (1)	0.12 (0)	0.10 (0)	0.13 (1)	0.07 (1)	0.08 (1)	0.12 (1)	0.10 (1)	0.13 (1)	0.07 (1)	
Vac = Xsud	0.29 (3)	0.18 (2)	0.25 (2)	0.18 (3)	0.35 (3)	0.34 (2)	0.19 (3)	0.27 (2)	0.18 (3)	0.34 (2)	
X _{Mg}	0.72 (2)	0.72 (1)	0.70 (1)	0.71 (2)	0.70 (2)	0.70 (1)	0.73 (1)	0.70 (1)	0.70 (2)	0.71 (1)	
T (°C)	341 (26)	396 (29)	351 (22)	405 (56)	312 (21)	302 (18)	370 (36)	336 (24)	406 (41)	310 (19)	

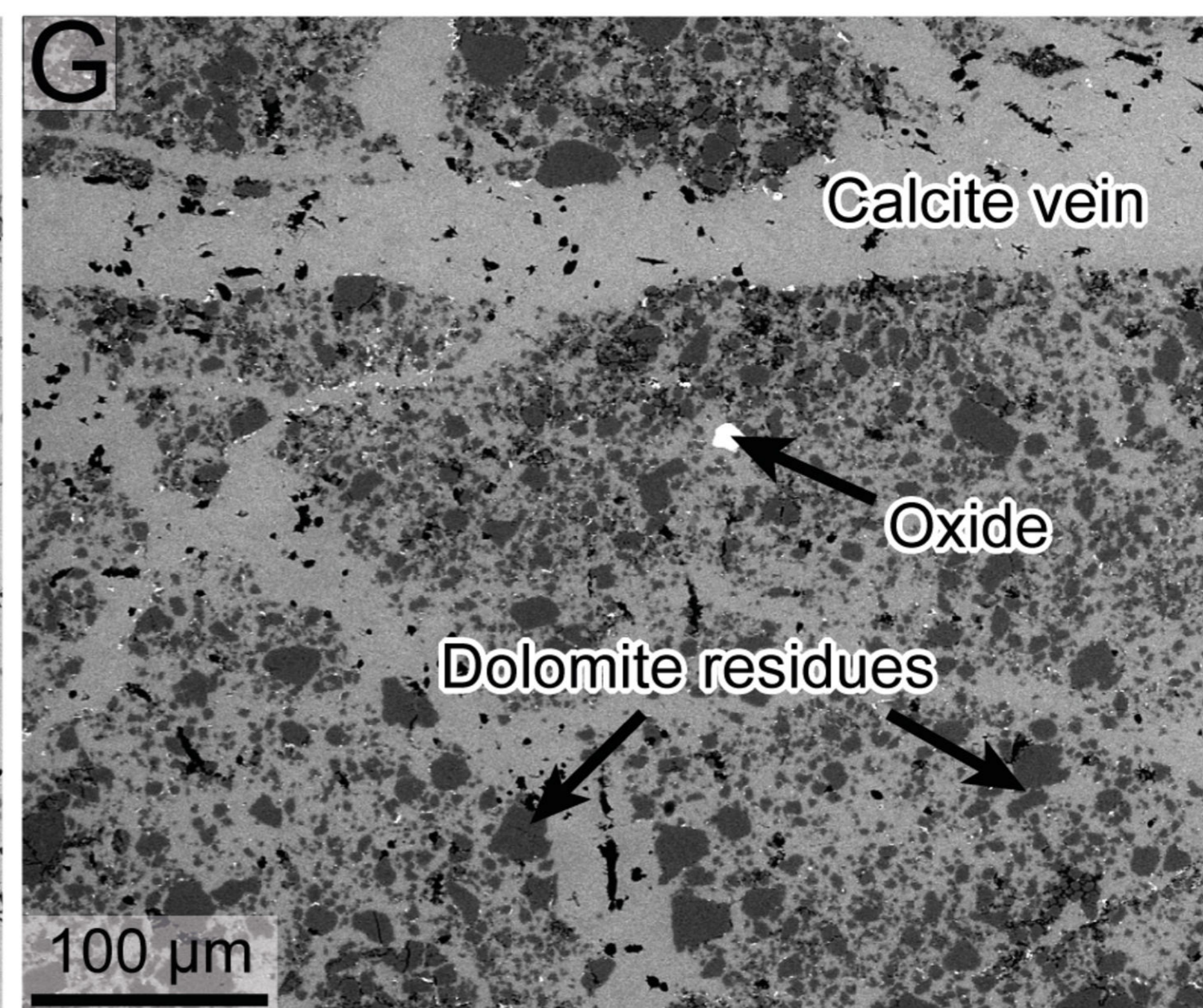
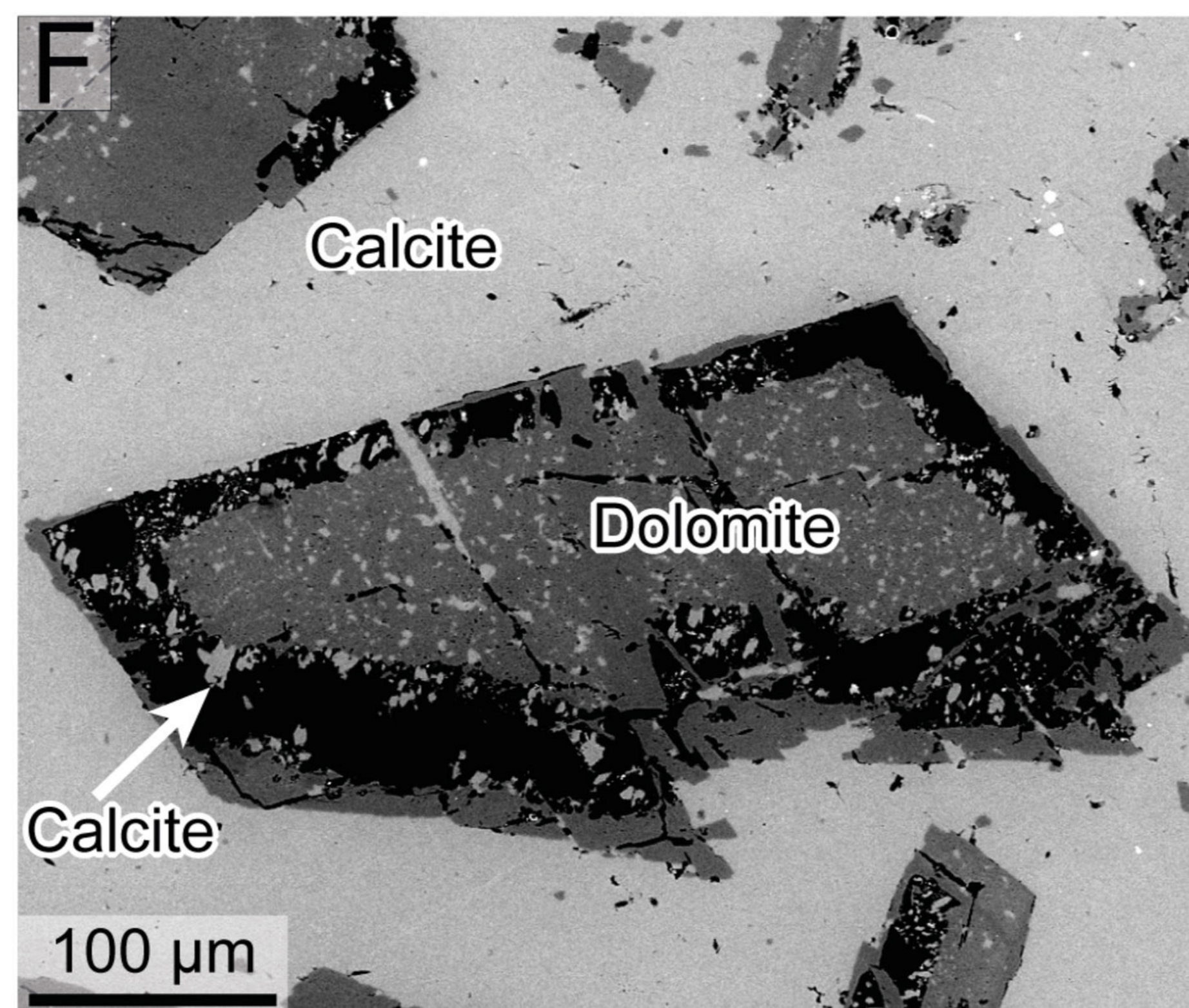
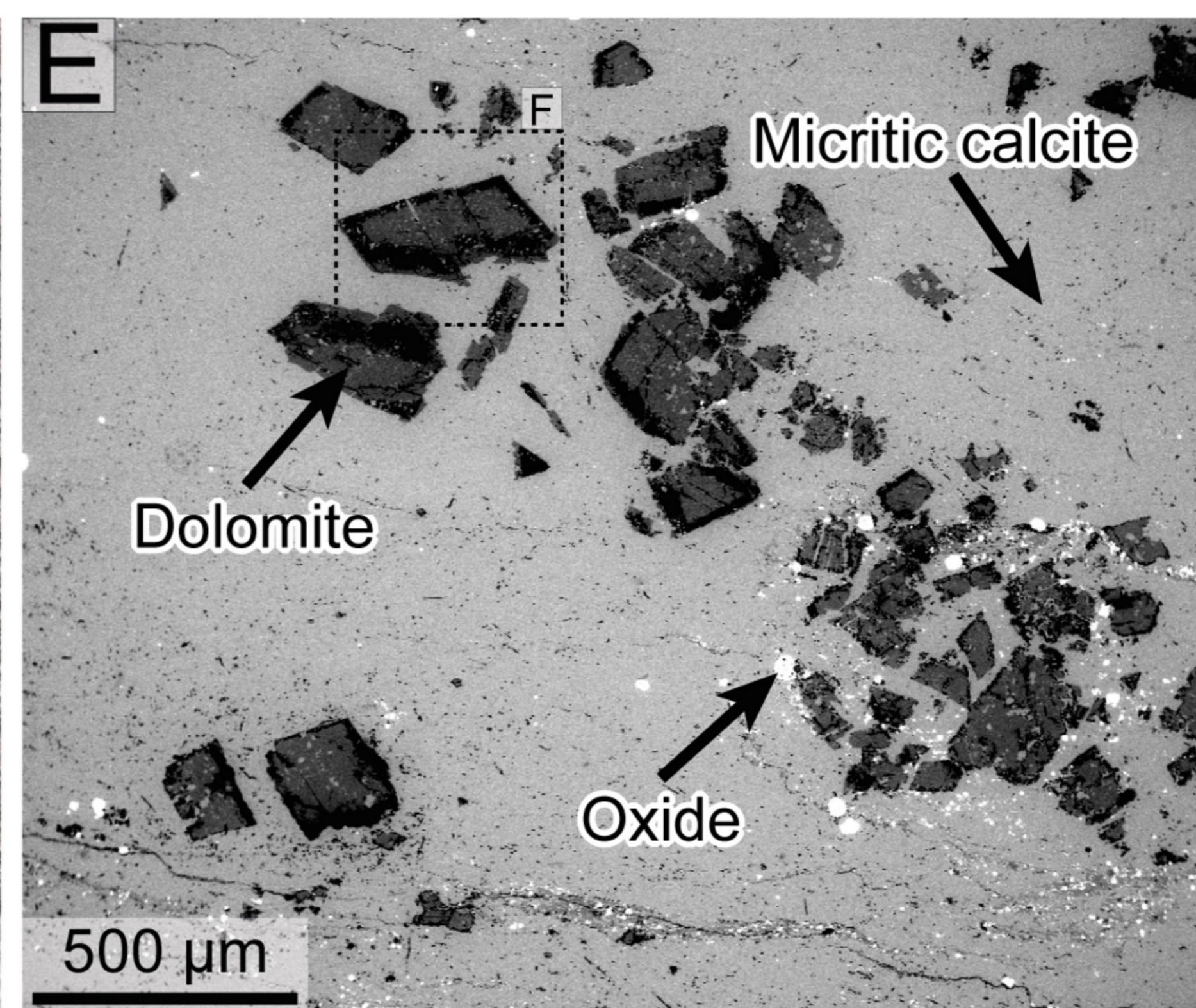
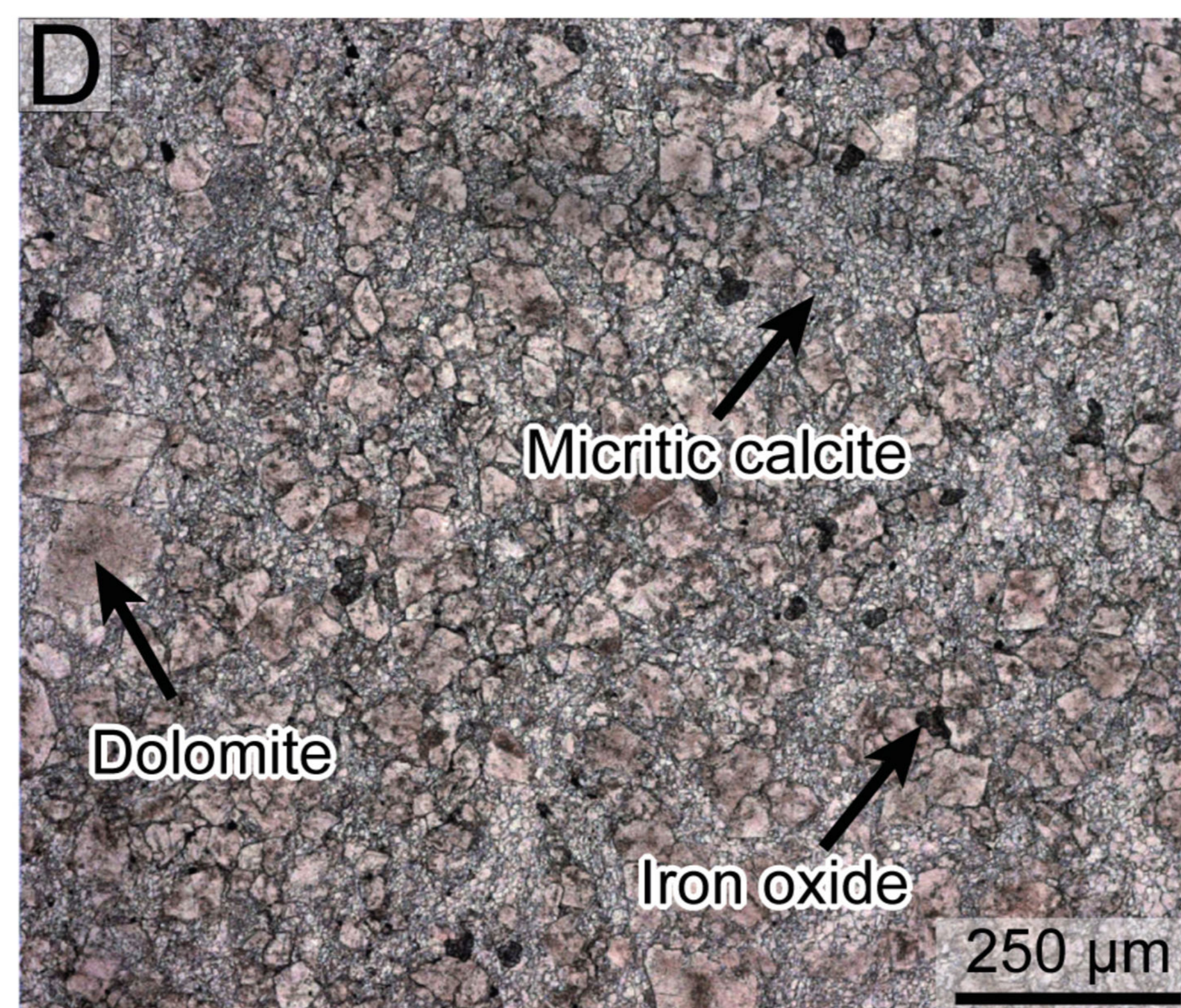
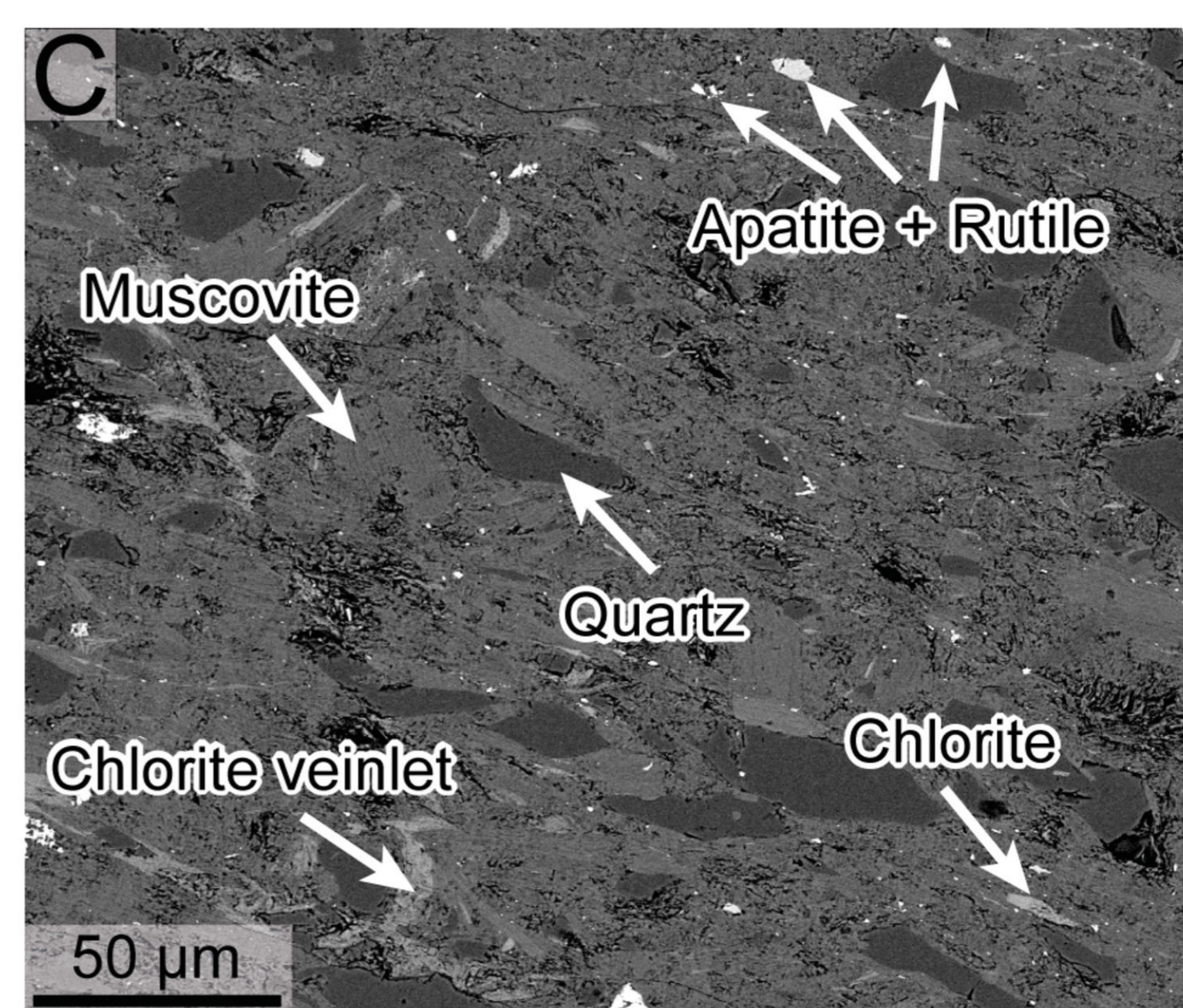
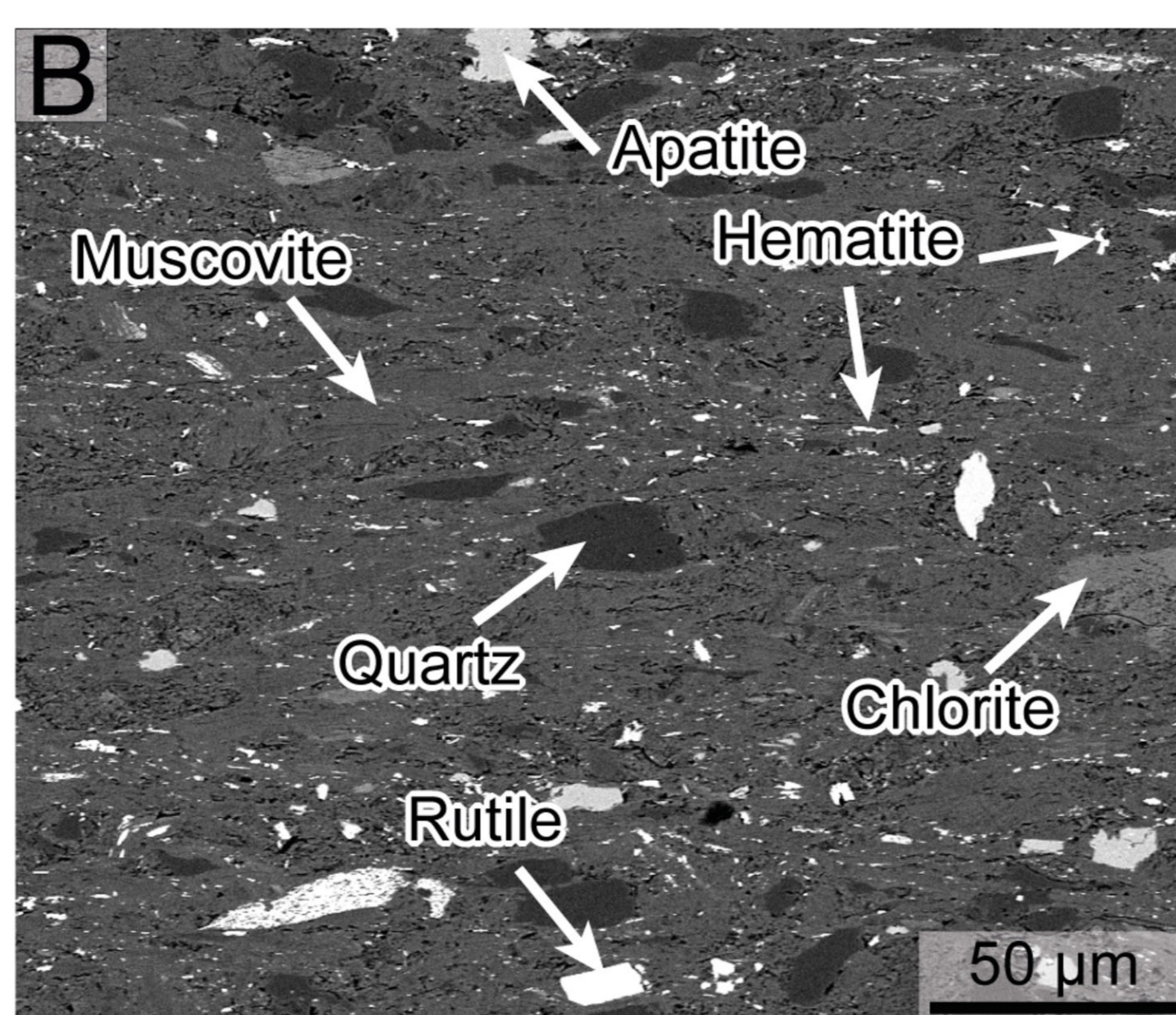
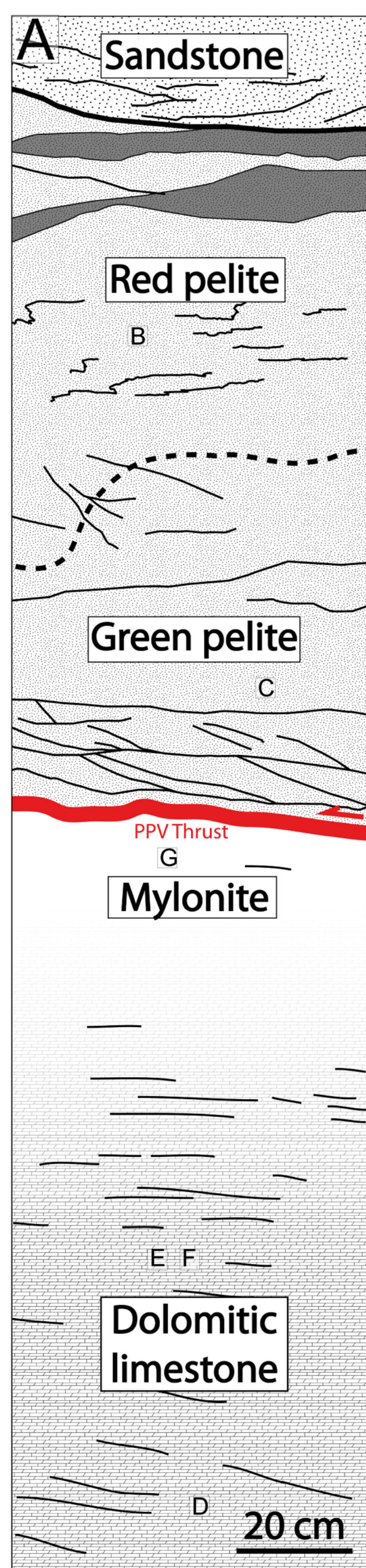
1007 **Table 2.** Chlorite structural formulas from sample PPV11-XX maps A and B. Unzoned
 1008 medians and standard deviation oxides %wt were added for comparison. $X_{MG} =$
 1009 $Mg^{2+}/(Fe^{2+}+Mg^{2+})$. Oxides in wt%, atoms in a.p.f.u.. Each data represent the average and
 1010 standard deviation of 400 points corresponding to 20*20 μm^2 in the map. $X_{Fe^{3+}}$ standard
 1011 deviation induce small variations in the structural formulas; they have not been reported in
 1012 this table. Points are reported on Figure 10.

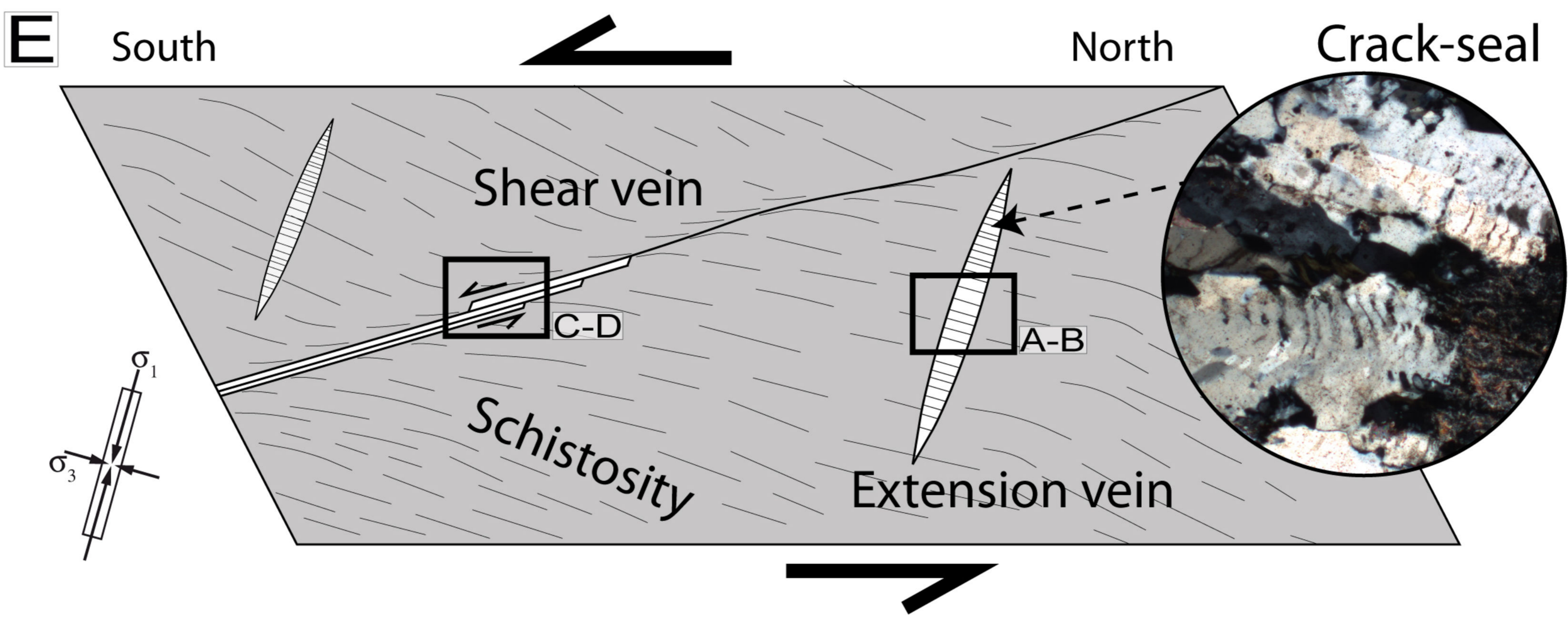
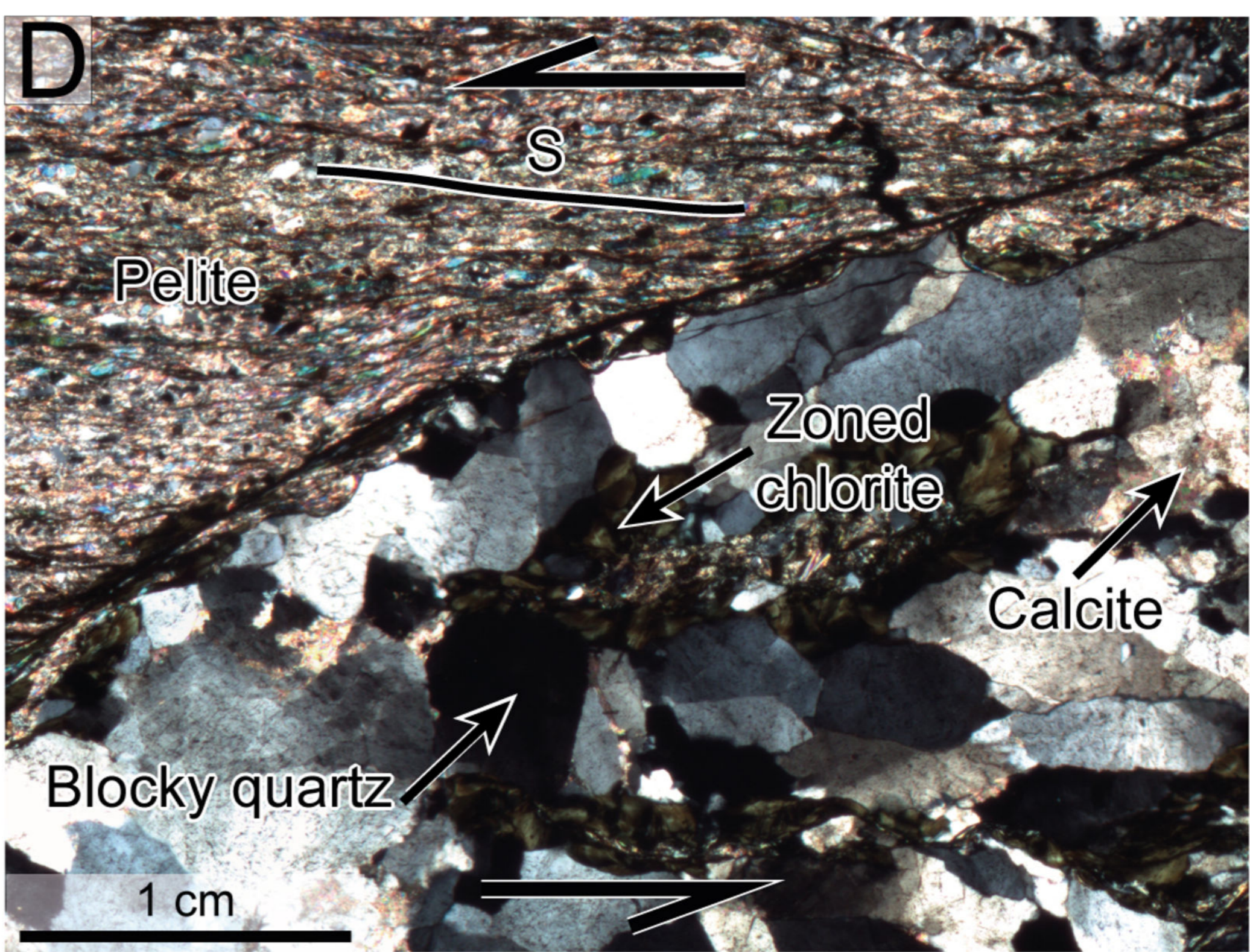
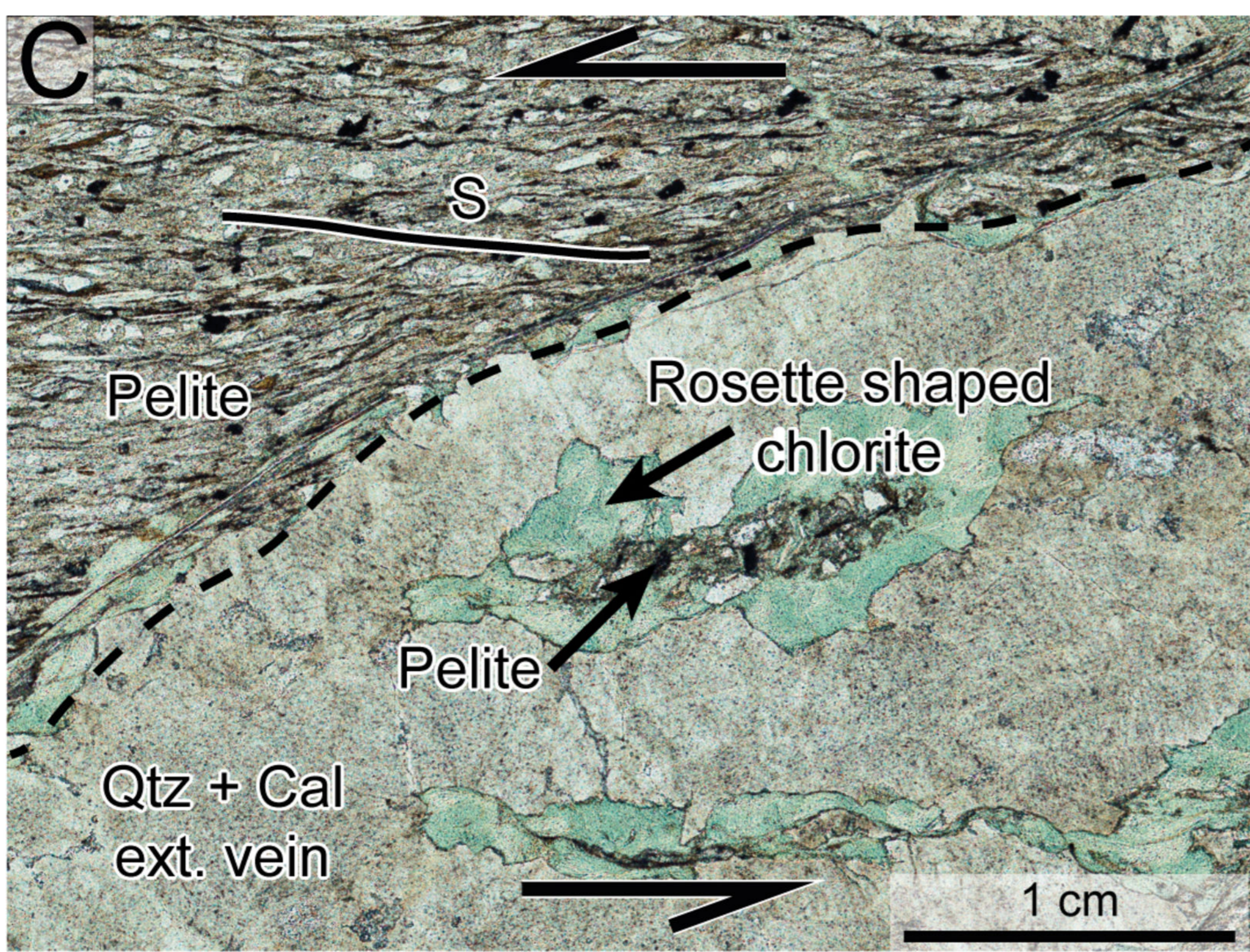
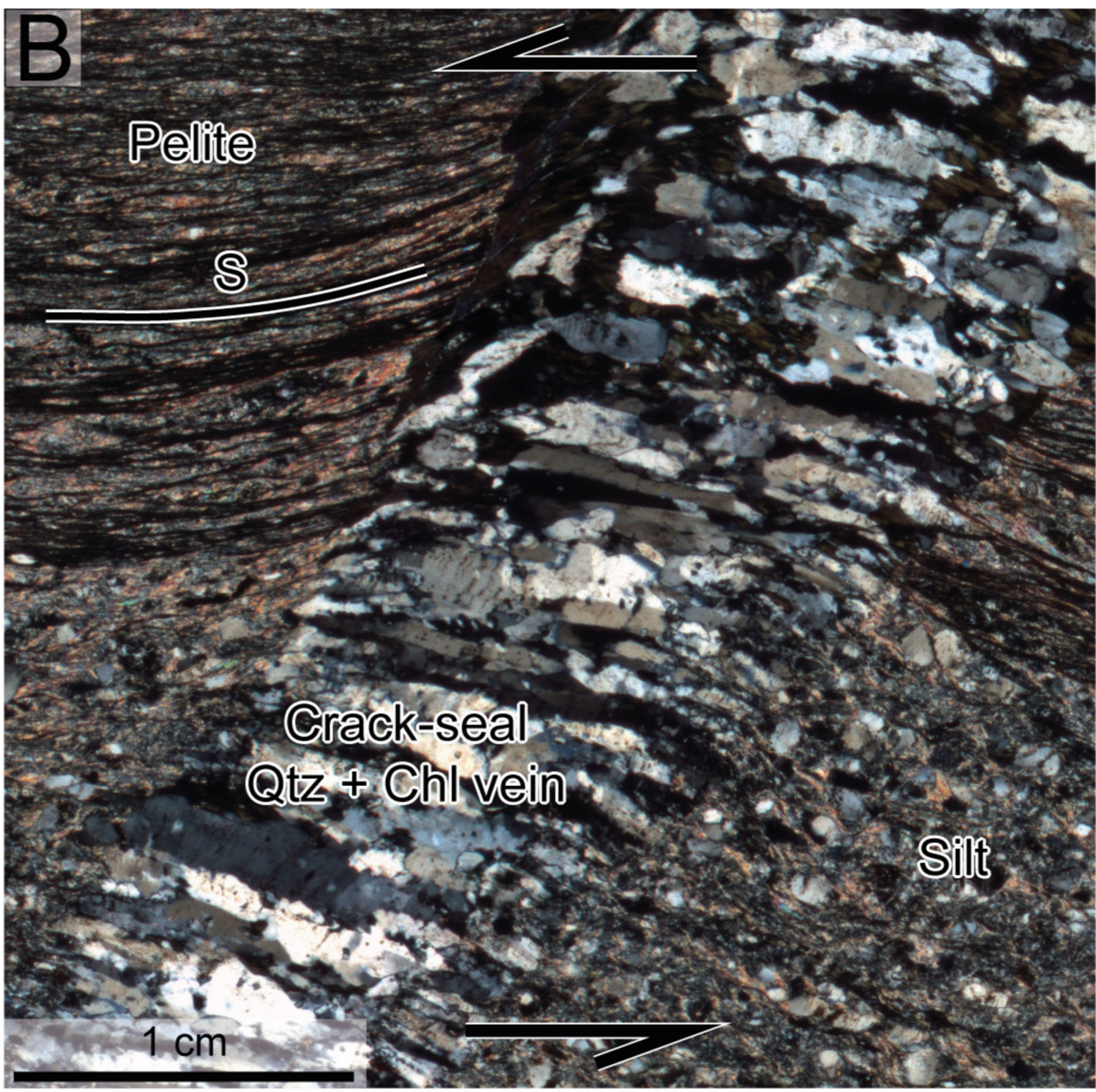
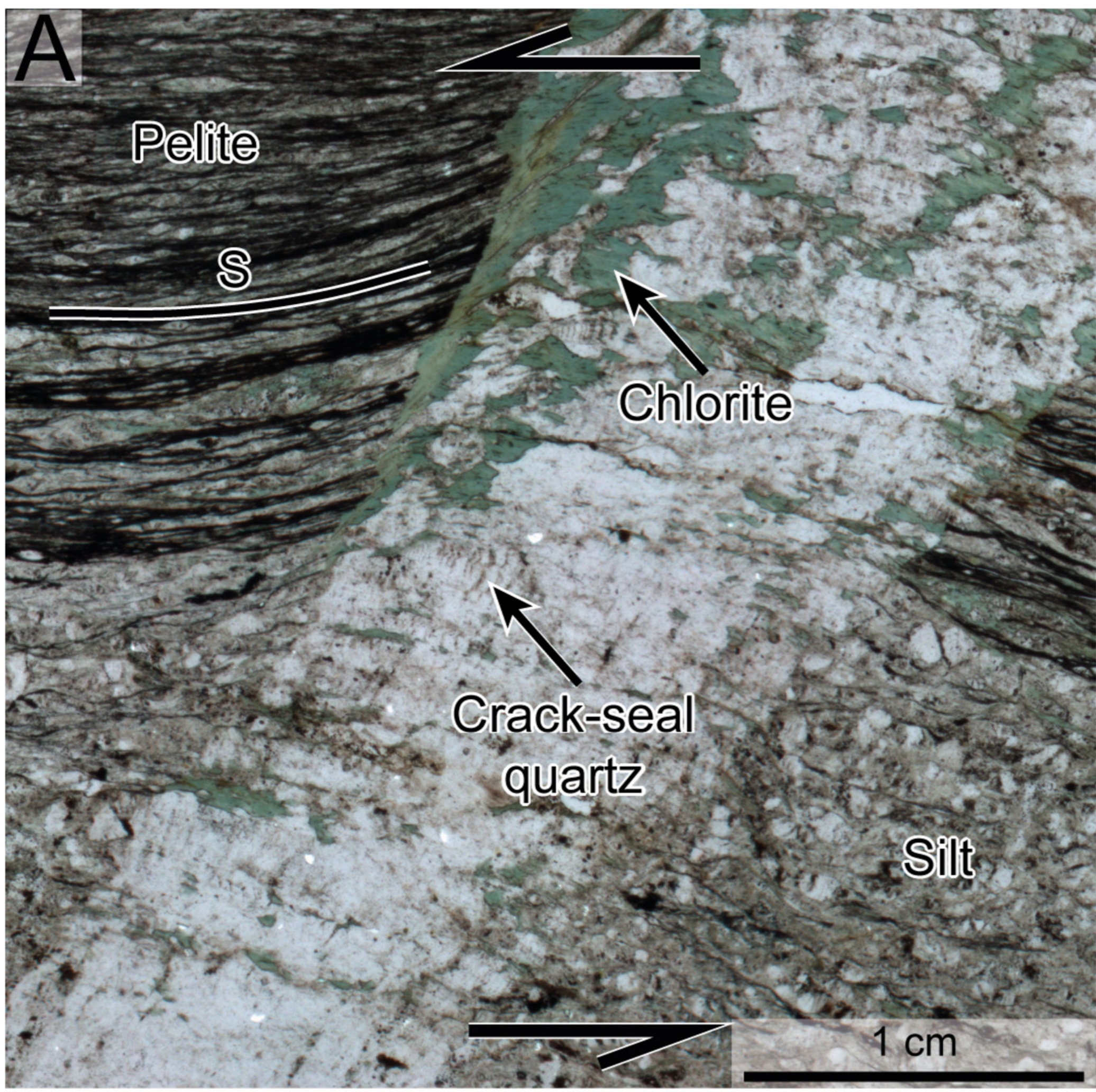
1013

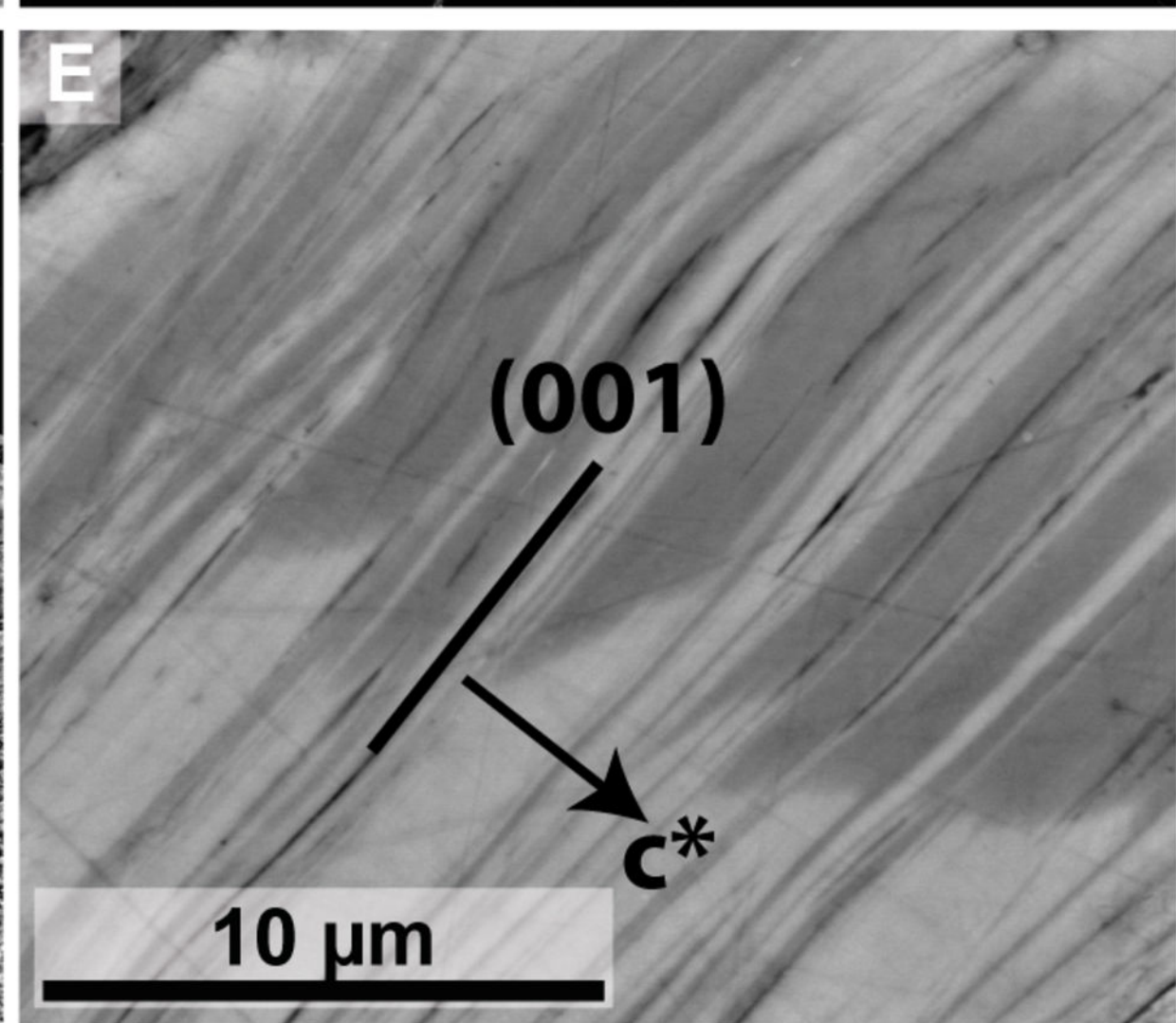
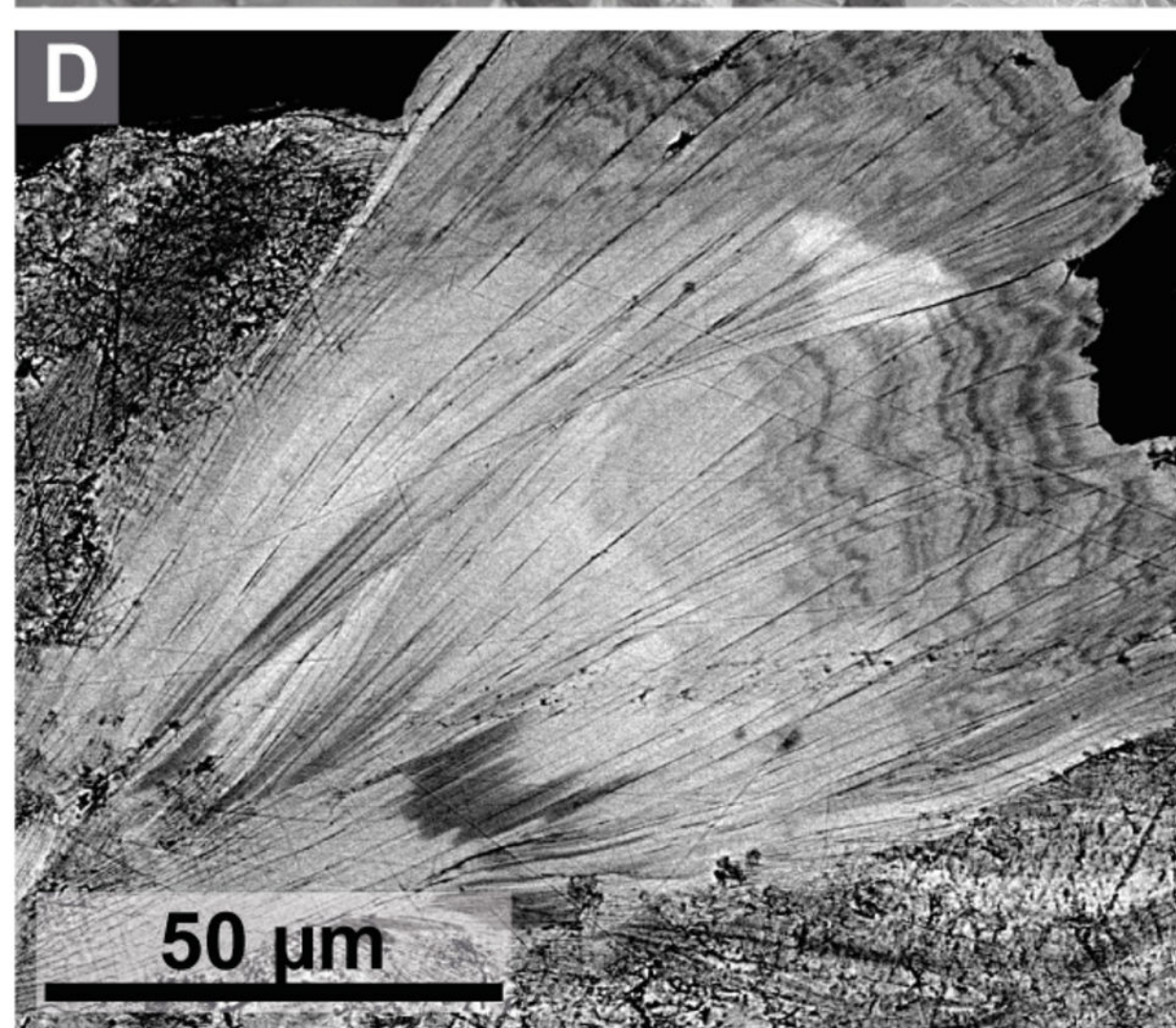
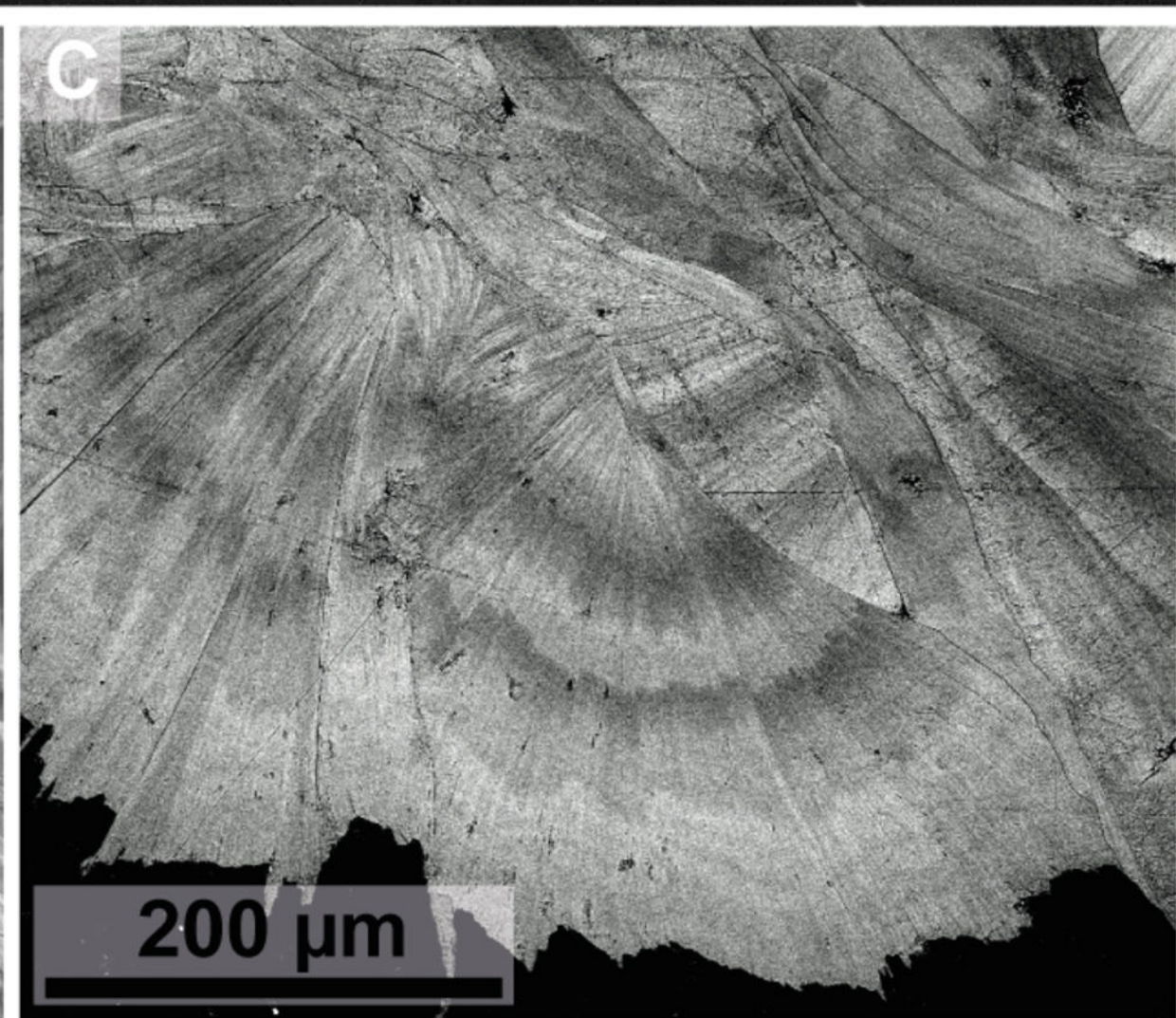
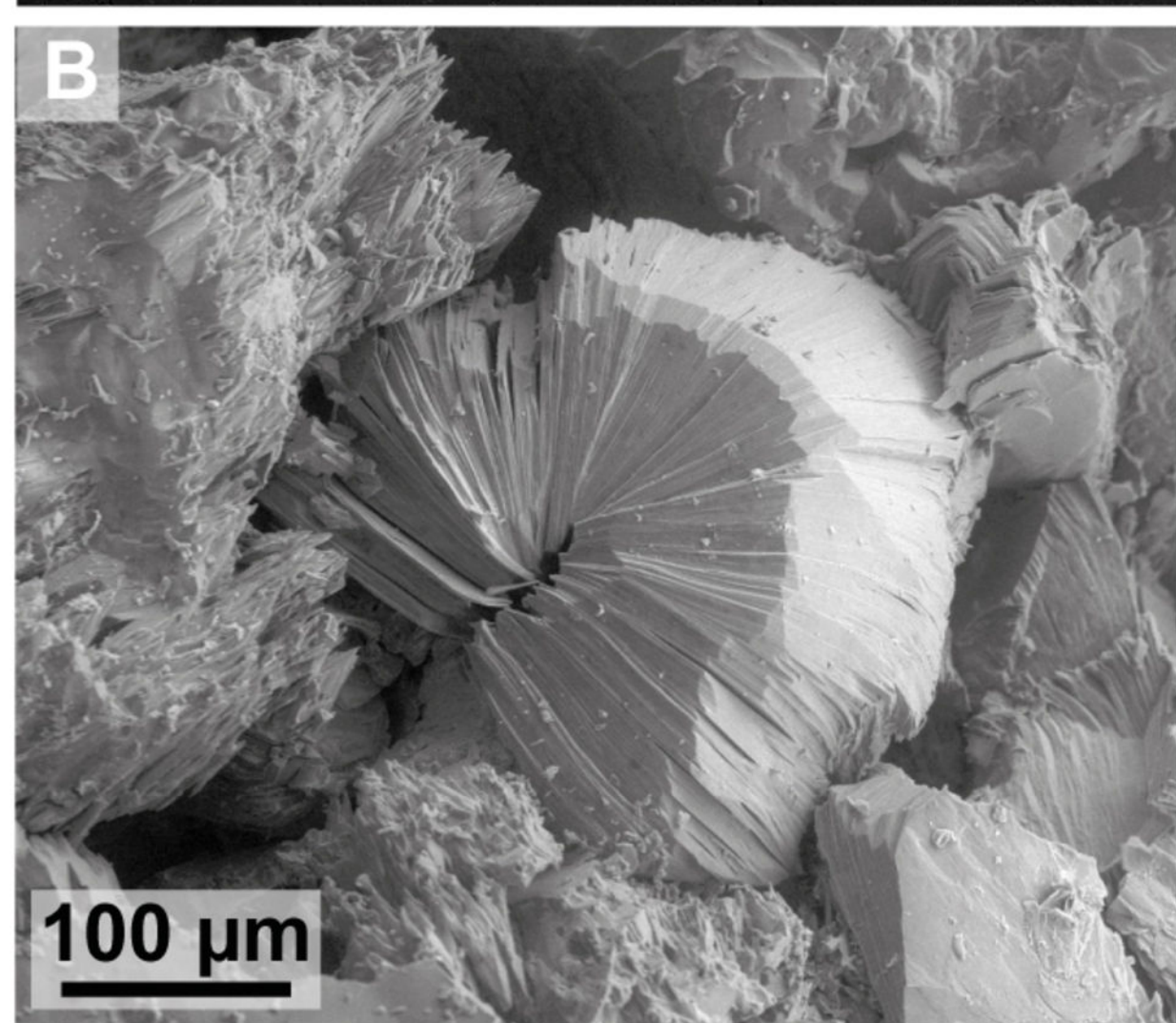
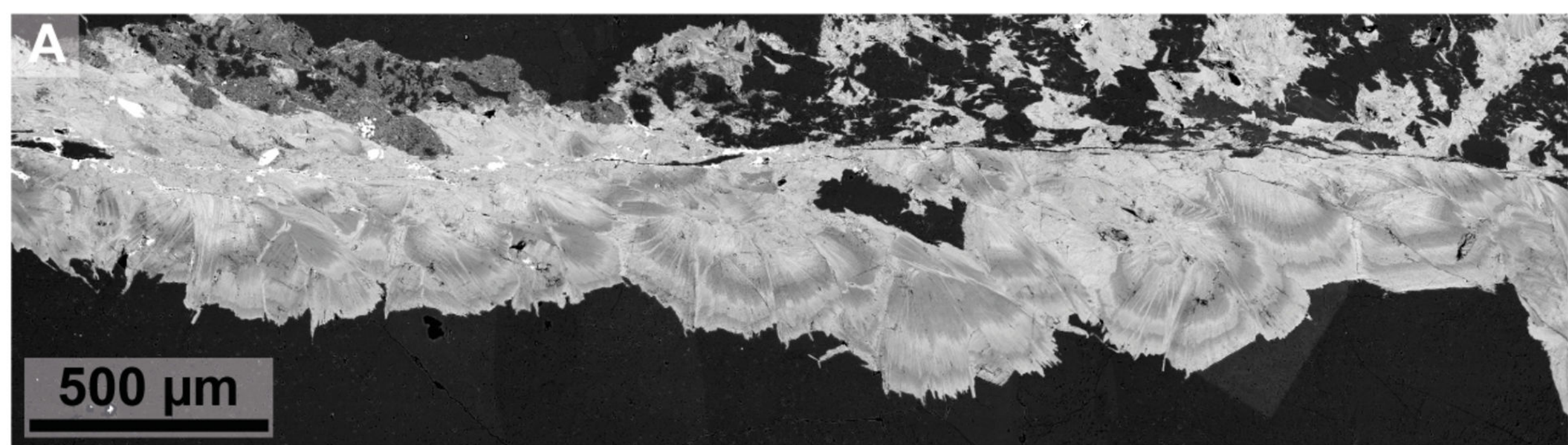


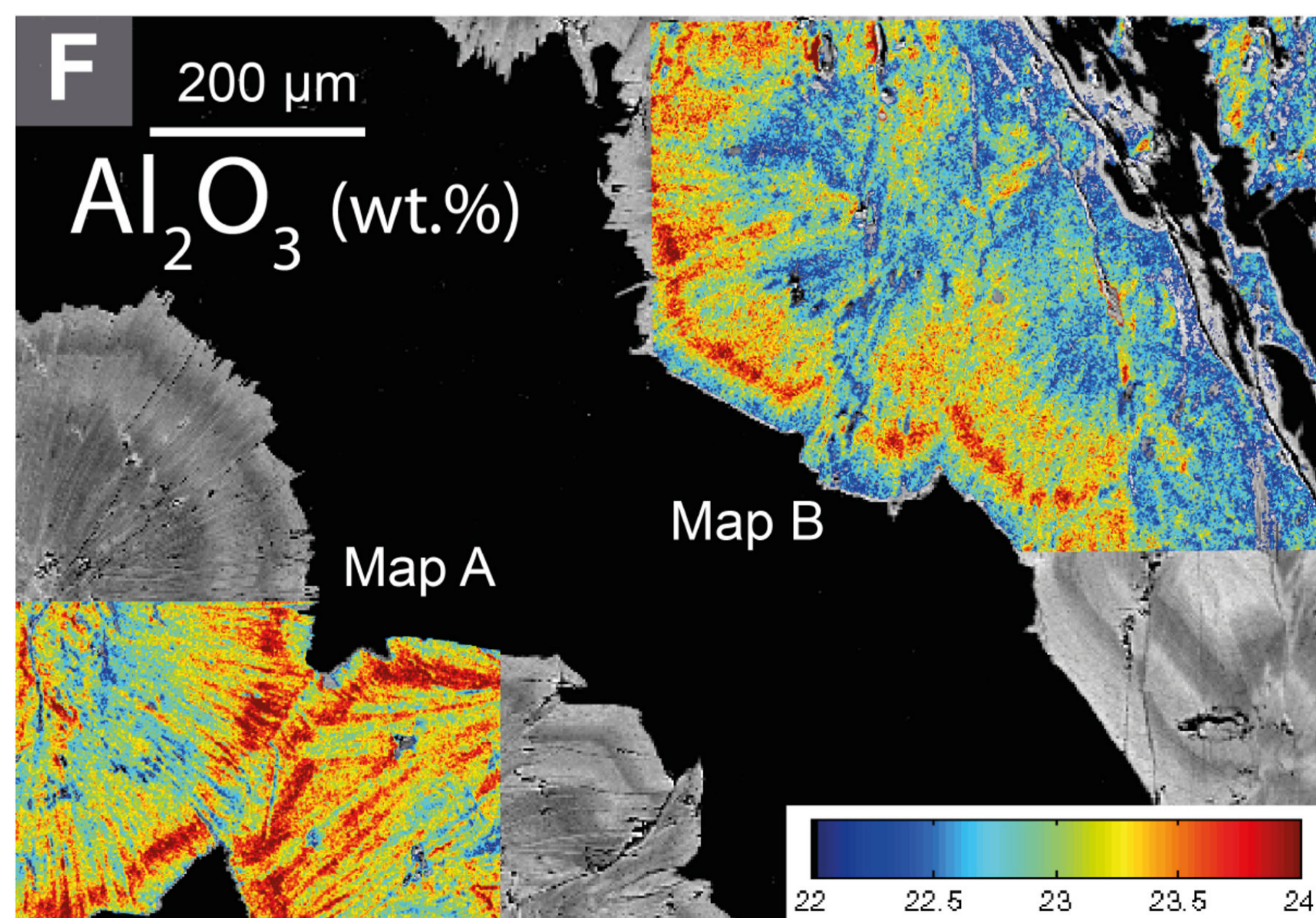
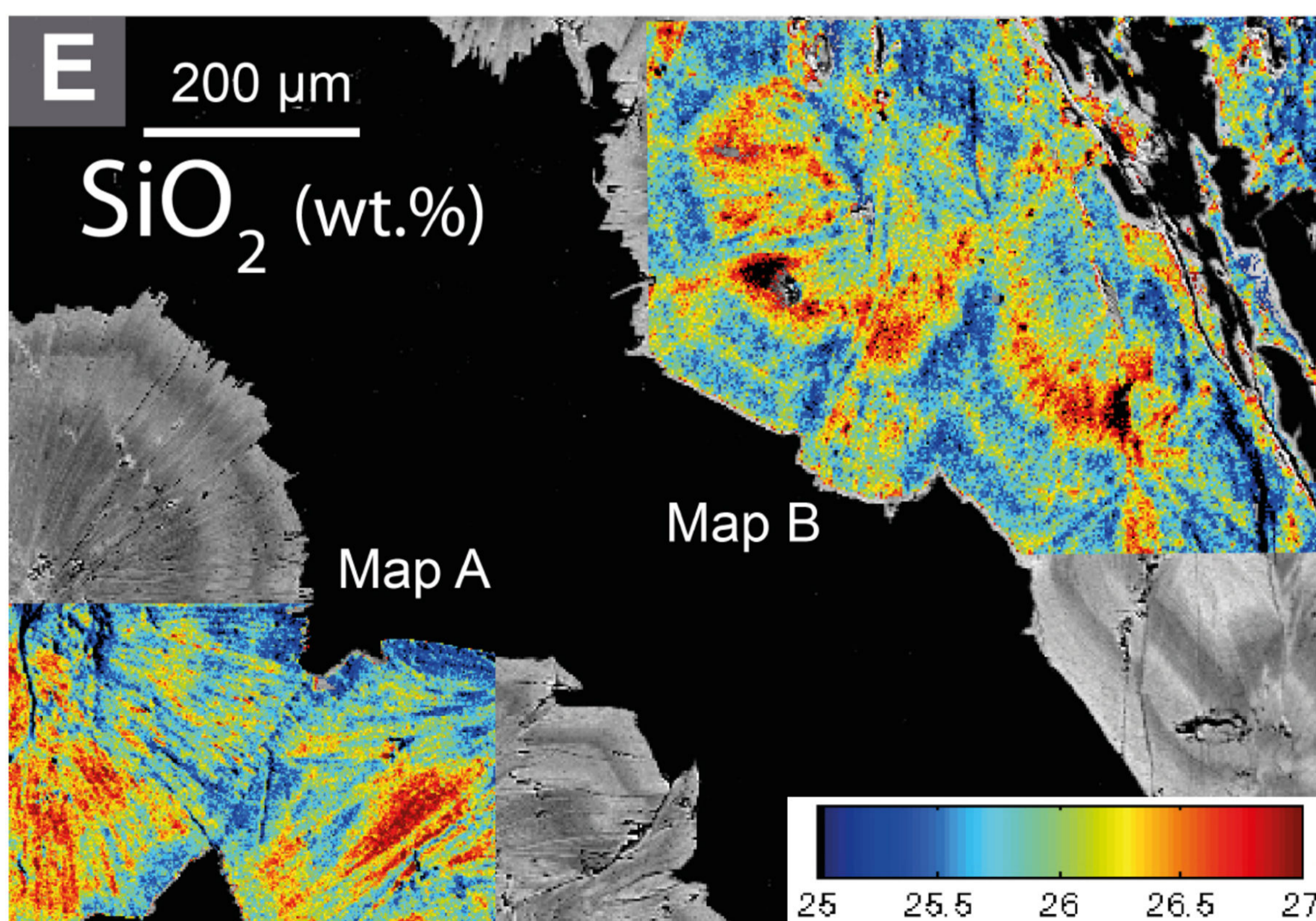
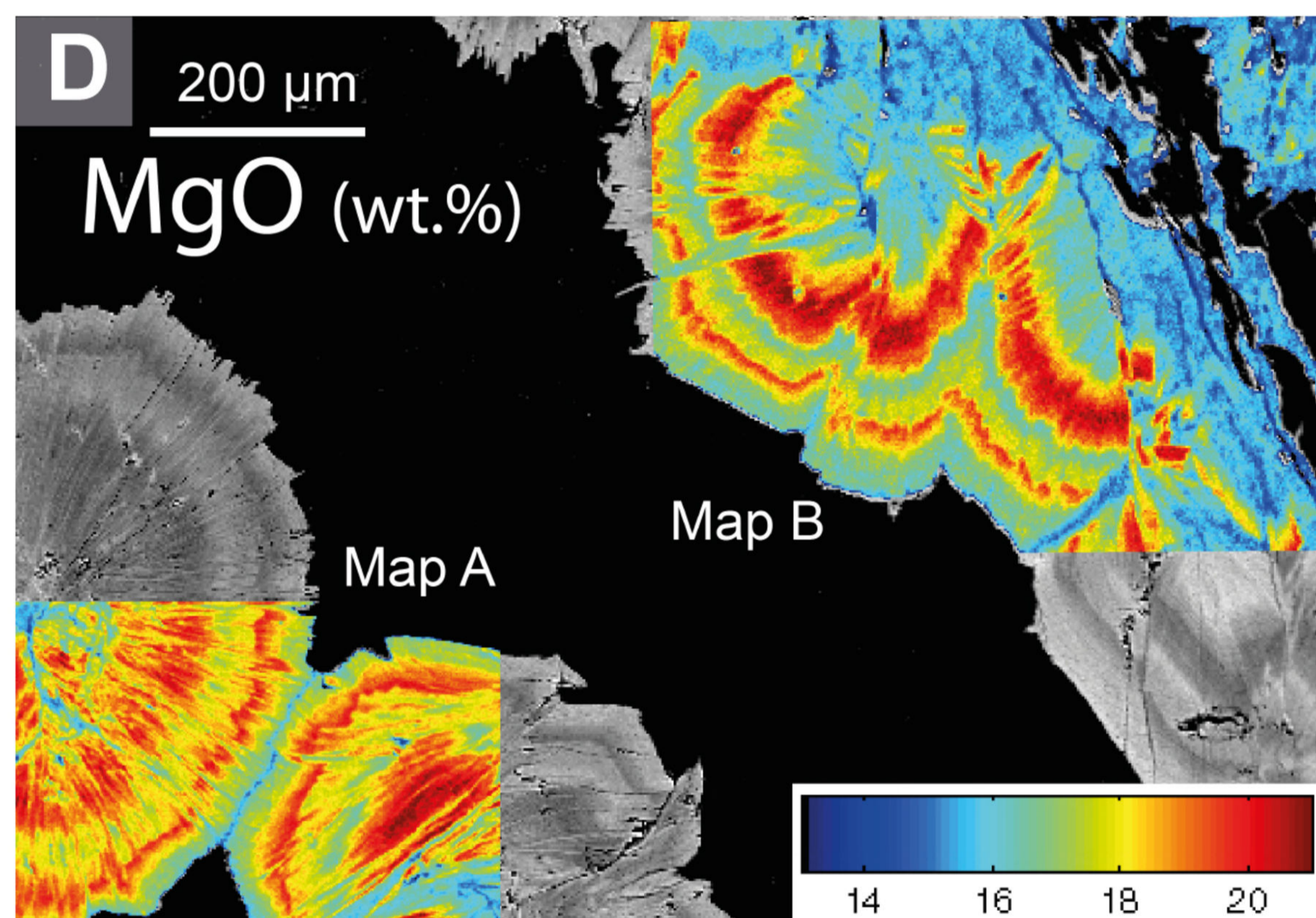
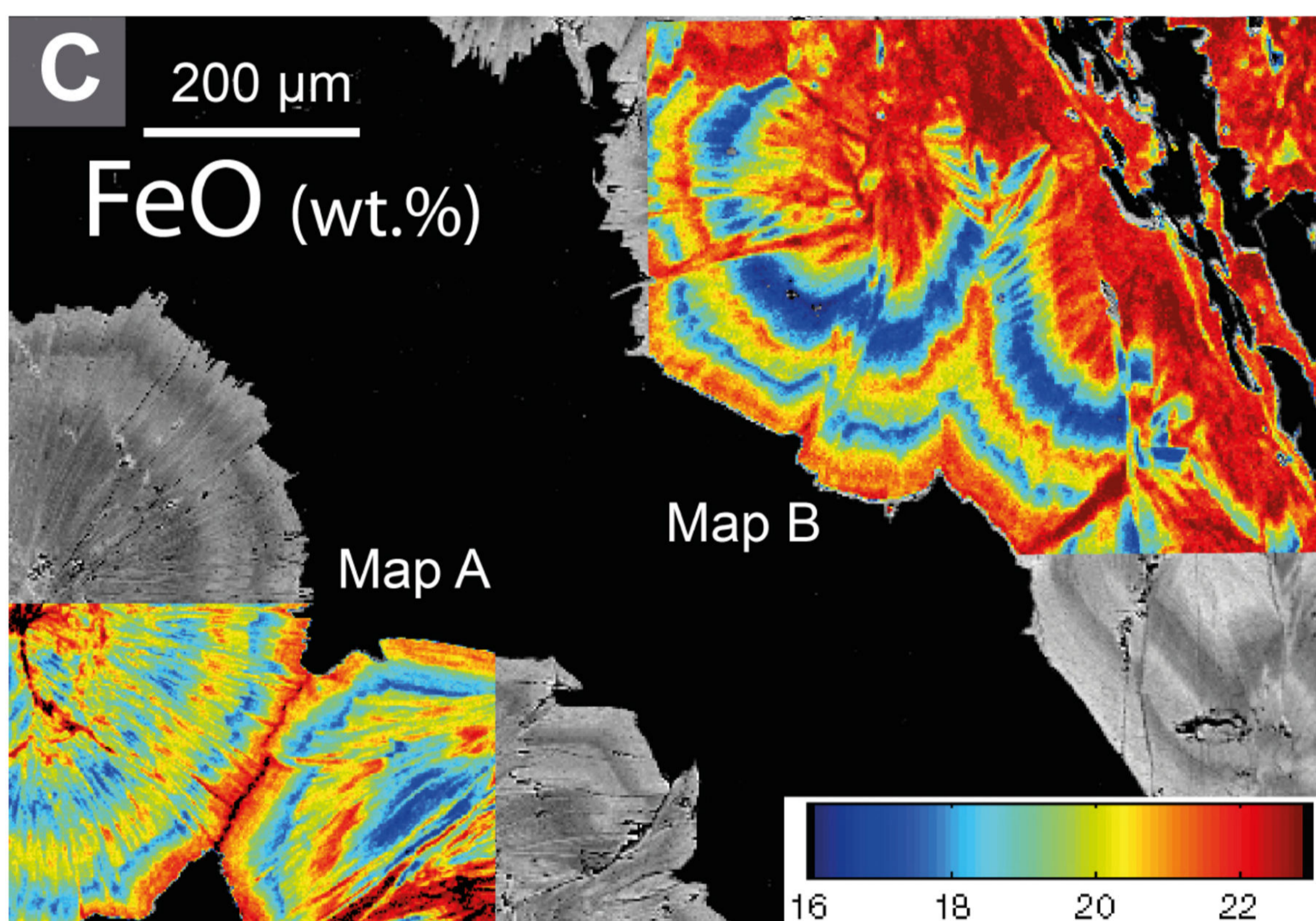
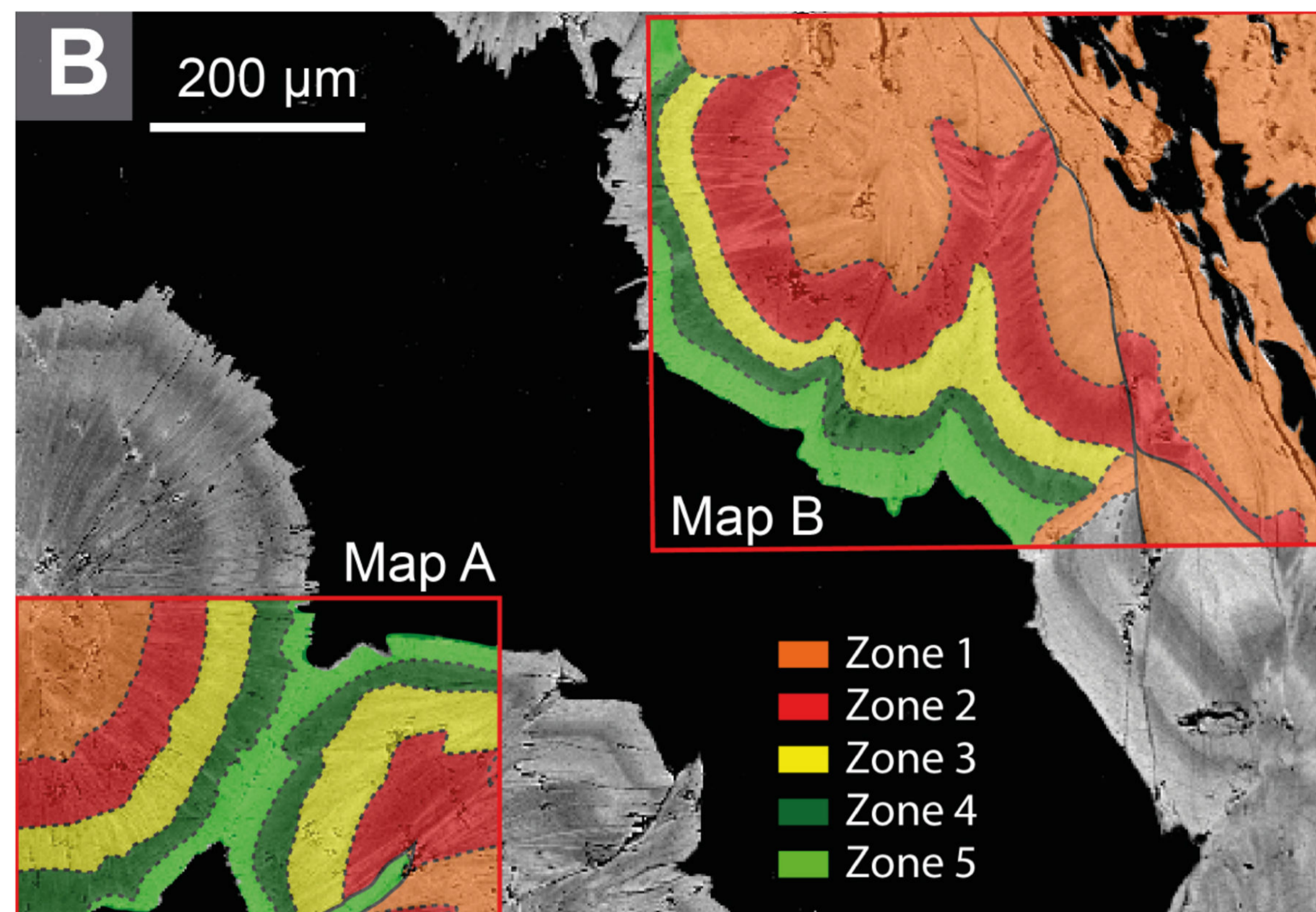
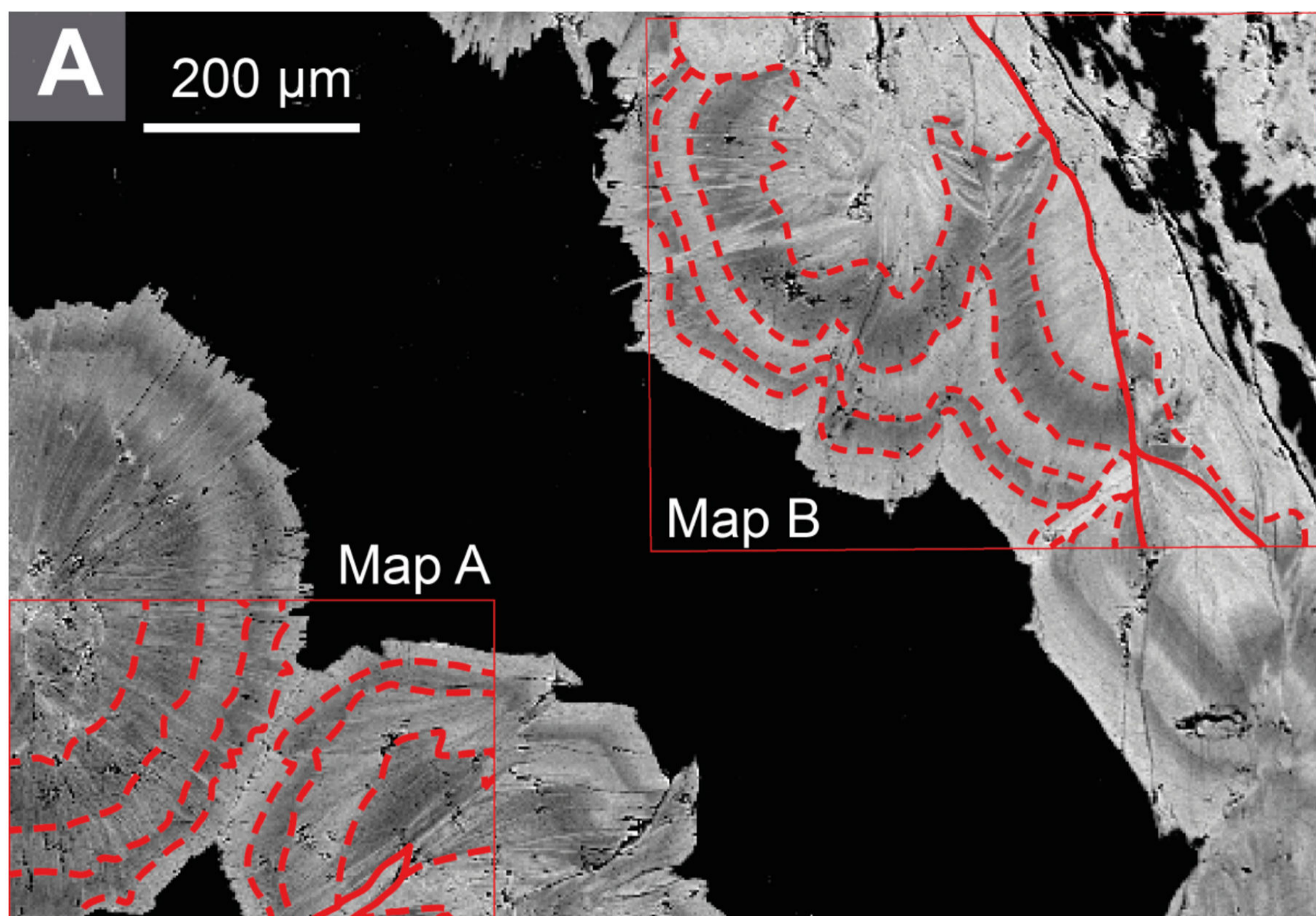


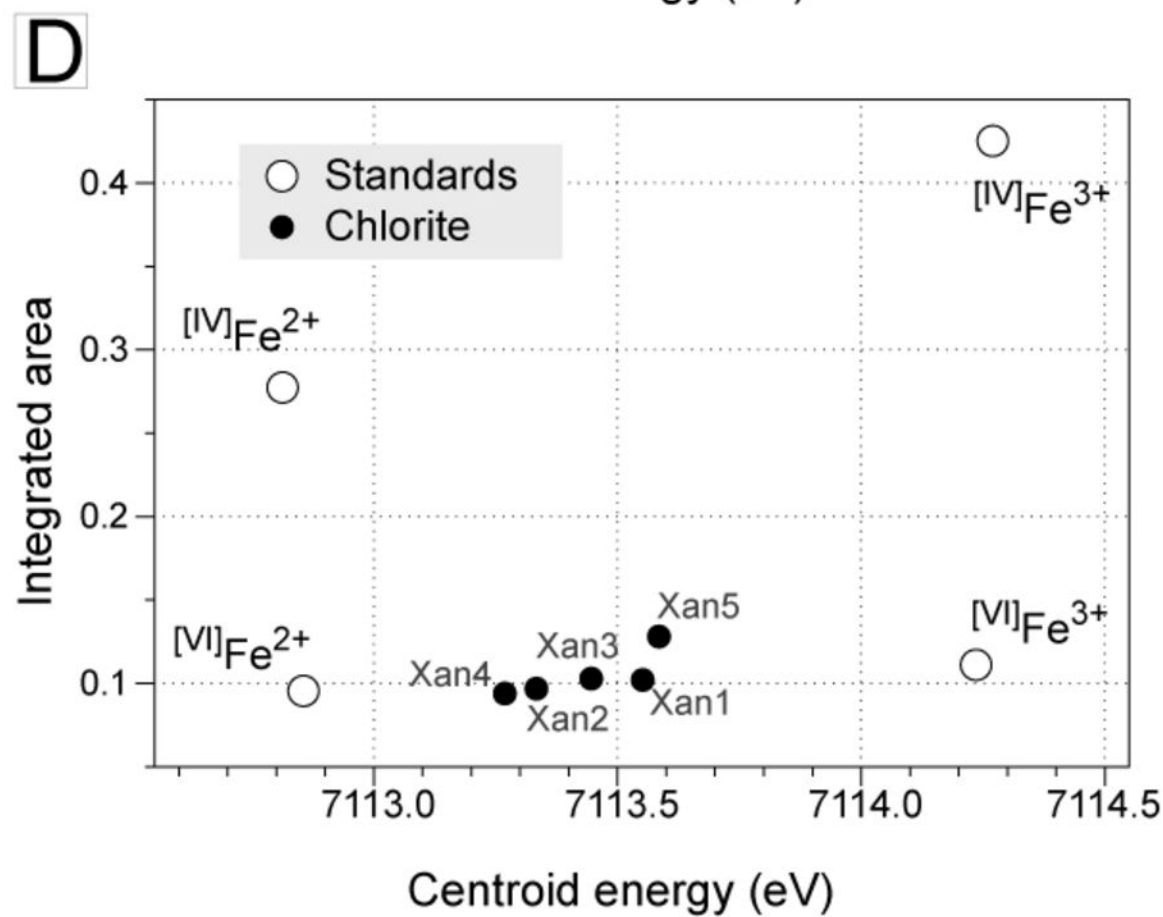
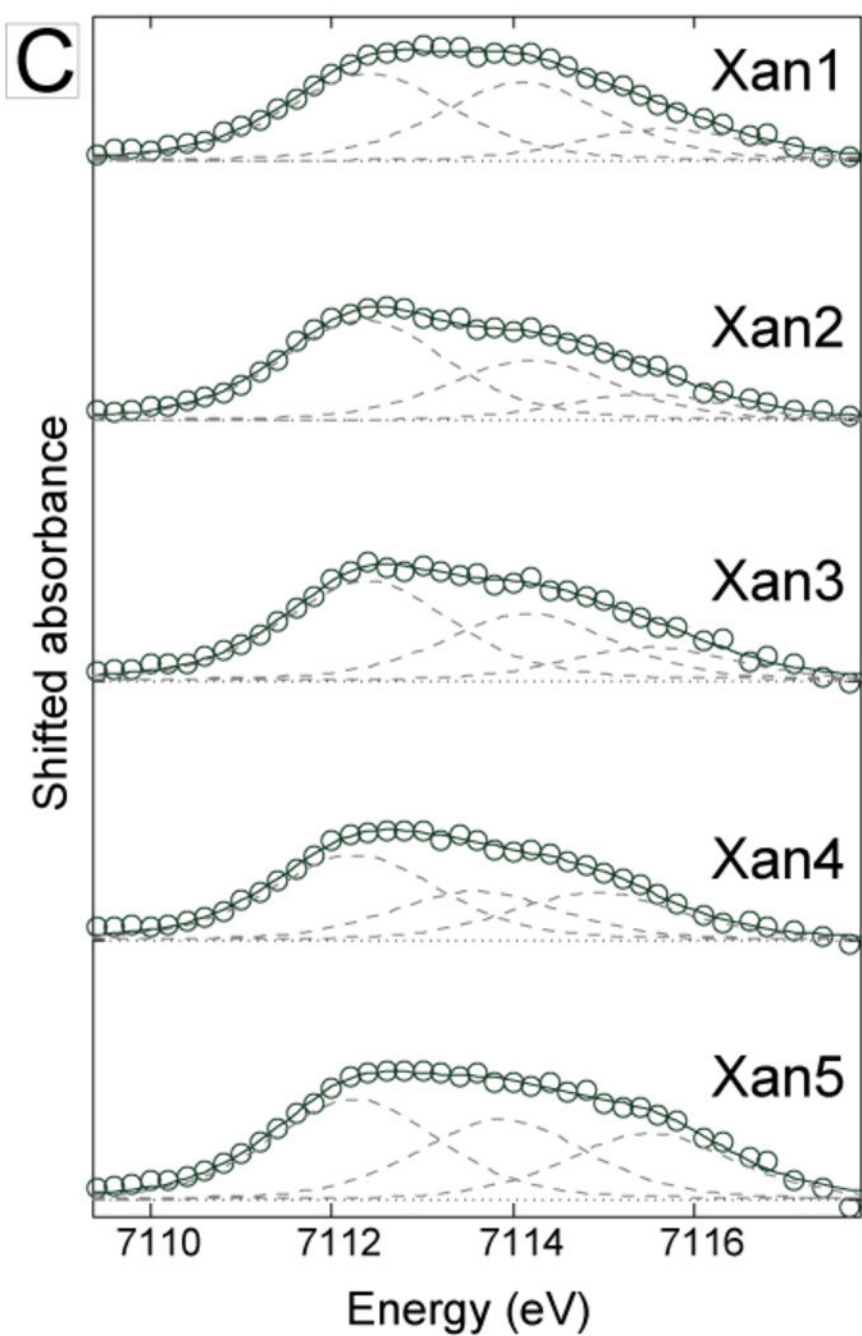
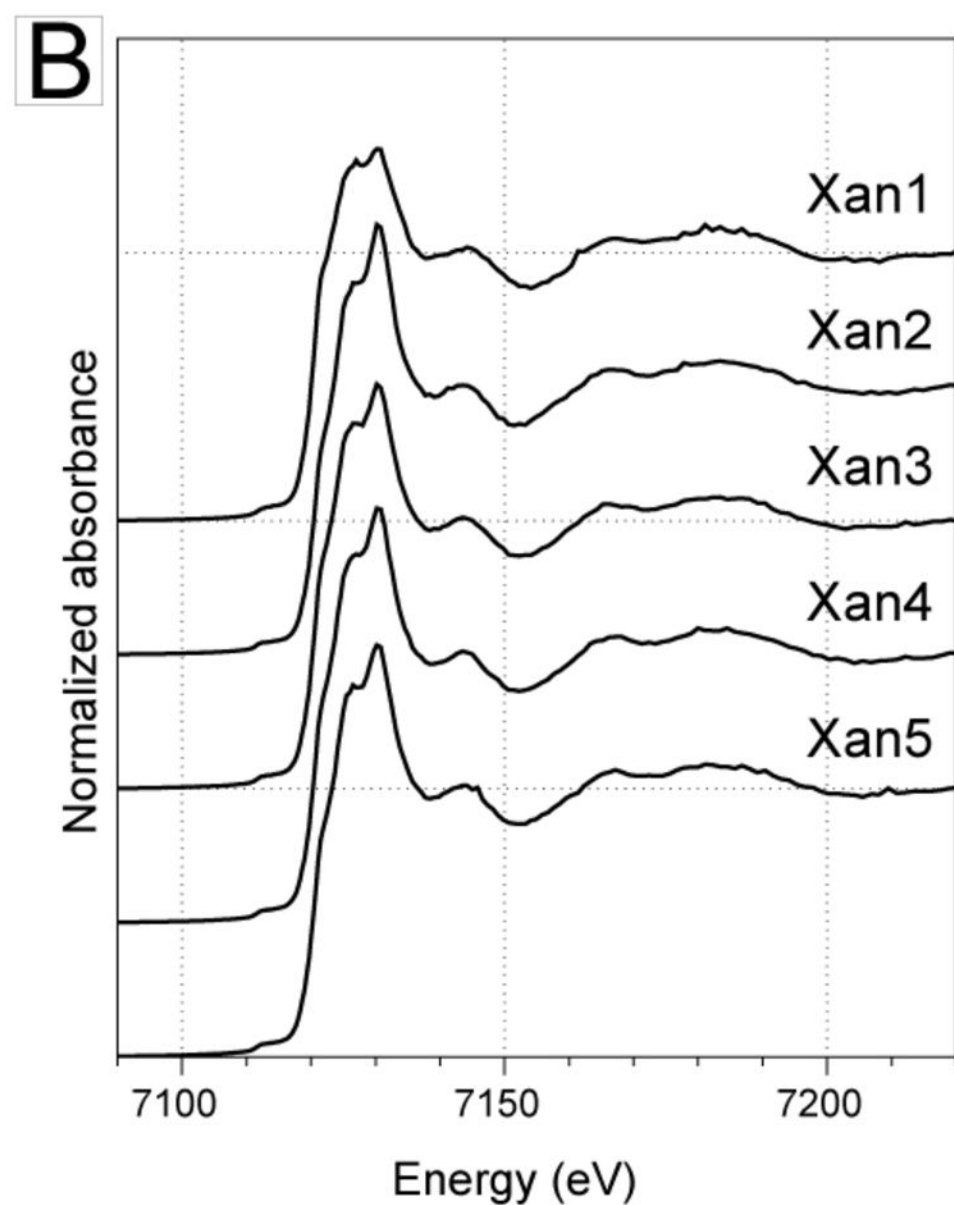
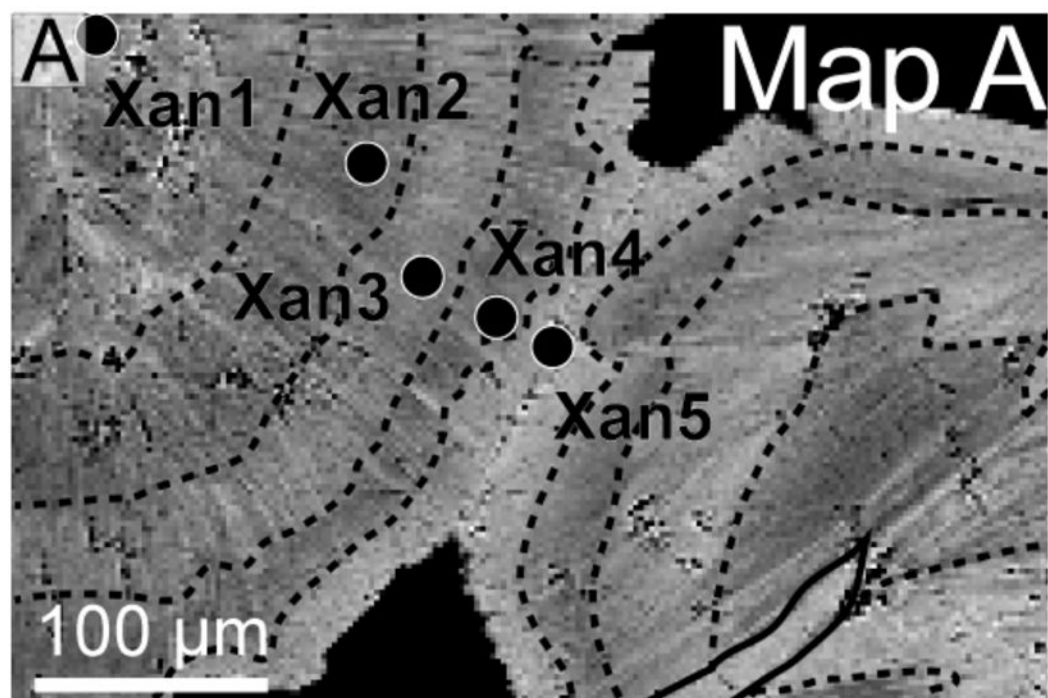






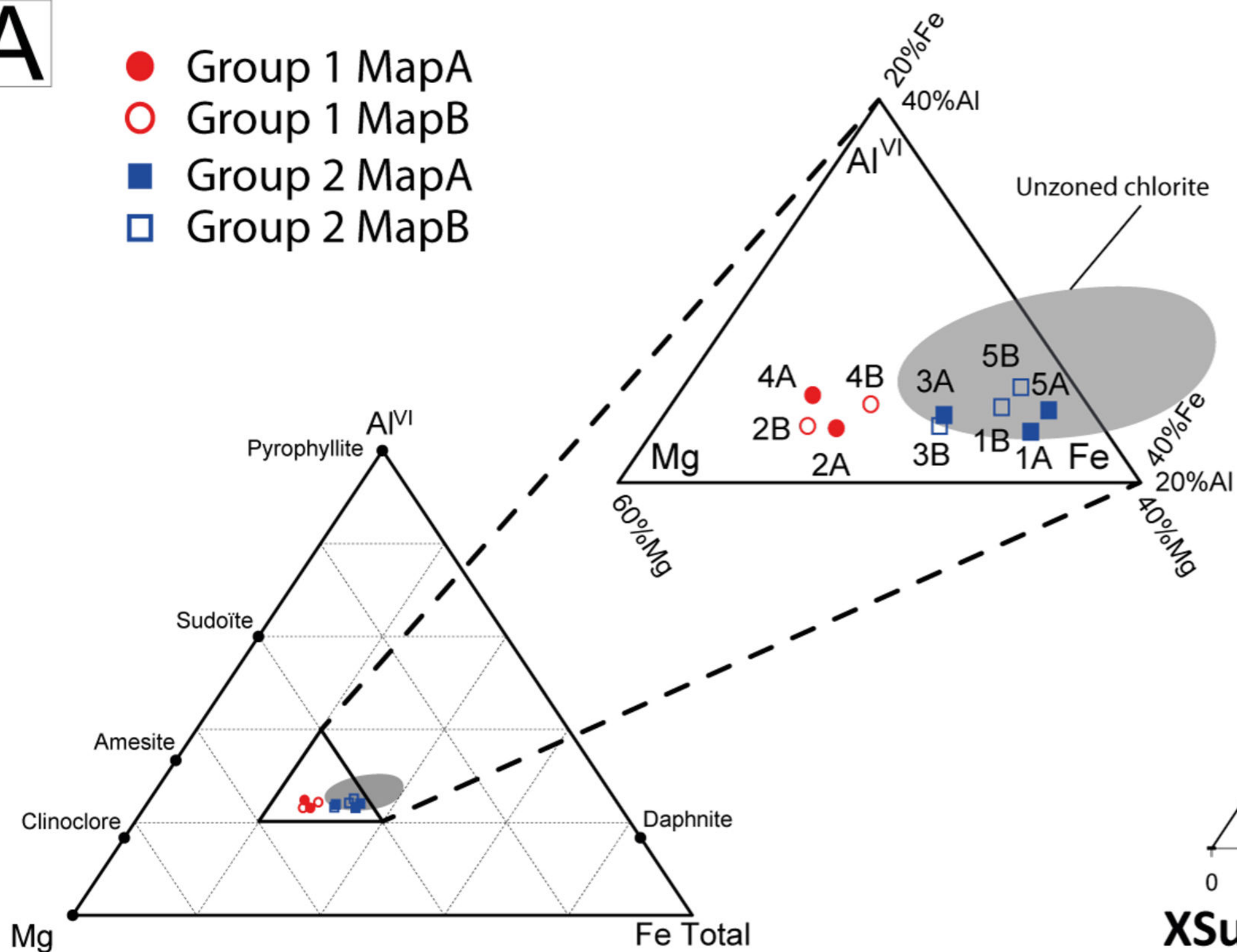






A

- Group 1 MapA
- Group 1 MapB
- Group 2 MapA
- Group 2 MapB

**B**